

AD/

FILE COPY
EOD ACCESSION LISTDRI Call No. 85423Copy No. 1 of 2 cys.

Semiannual Technical Summary

Seismic Discrimination

30 June 1976

Prepared for the Defense Advanced Research Projects Agency
under Electronic Systems Division Contract F19628-76-C-0002 by

Lincoln Laboratory

MASSACHUSETTS INSTITUTE OF TECHNOLOGY

LEXINGTON, MASSACHUSETTS



Approved for public release; distribution unlimited.

ADA032754

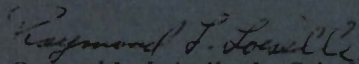
The work reported in this document was performed at Lincoln Laboratory, a center for research operated by Massachusetts Institute of Technology. This research is a part of Project Vela Uniform, which is sponsored by the Defense Advanced Research Projects Agency under Air Force Contract F19628-76-C-0002 (ARPA Order 512).

This report may be reproduced to satisfy needs of U.S. Government agencies.

The views and conclusions contained in this document are those of the contractor and should not be interpreted as necessarily representing the official policies, either expressed or implied, of the Defense Advanced Research Projects Agency of the United States Government.

This technical report has been reviewed and is approved for publication.

FOR THE COMMANDER


Raymond L. Loiselle, Lt. Col., USAF
Chief, ESD Lincoln Laboratory Project Office

Non-Lincoln Recipients

PLEASE DO NOT RETURN

Permission is given to destroy this document
when it is no longer needed.

MASSACHUSETTS INSTITUTE OF TECHNOLOGY
LINCOLN LABORATORY

SEISMIC DISCRIMINATION

SEMIANNUAL TECHNICAL SUMMARY REPORT
TO THE
DEFENSE ADVANCED RESEARCH PROJECTS AGENCY

1 JANUARY - 30 JUNE 1976

ISSUED 21 SEPTEMBER 1976

Approved for public release; distribution unlimited.

LEXINGTON

MASSACHUSETTS

ABSTRACT

This report describes 25 investigations in the field of seismic discrimination. These are grouped as follows: estimation of body wave magnitude m_b by single stations and networks (9 contributions), surface wave studies (2 contributions), examination of methods for the separation of the signals from a sequence of closely spaced explosions (2 contributions), studies concerned with lateral heterogeneity within the earth (5 contributions), miscellaneous studies (3 contributions), and recent developments in our data and computer systems (4 contributions).

CONTENTS

Abstract	iii
Summary	vii
I. BODY WAVE MAGNITUDE m_b	1
A. Global Variations in Station Magnitude Bias	1
B. Source Region Variations in Bias	4
C. Temporal Variations in the Shape of the Magnitude-Frequency Curve	5
D. Comparison of Recent Estimates of Magnitude Bias	7
E. Seismic Magnitude Simulation Studies	9
1. True Magnitude Distributions	9
2. Bias and Scatter Parameters	10
3. Station Detection Characteristics	10
F. Magnitude Differences Between Station Pairs	14
G. Estimation of Seismic Source at 1 Hz from $\log(A/T)$	15
H. Evidence for ω -Cube Scaling from Short-Period Amplitudes and Periods of the Rat Island Sequence (1965)	17
I. Contribution of WWSSN Stations to the PDE Bulletin	19
II. SURFACE WAVE STUDIES	39
A. The Effects of Lateral Heterogeneity in the Oceanic Lithosphere Upon Surface Wave Propagation	39
B. Synthetic Rayleigh Wave Seismograms for the Fallon Earthquake	40
III. EVASION	49
A. Detecting Multiple Events in Narrowband Seismograms	49
B. Comparison of Different Prediction Error Filters on a Synthetic Composite Event	50
IV. EARTH HETEROGENEITY	55
A. Analysis of Scattering from Novaya Zemlya Explosions	55
B. Mislocation Patterns for Seismic Networks	56
C. Large-Scale Heterogeneities in the Lower Mantle; Correlation with the Gravity Field	57
D. Internal Discontinuities in the Earth's Structure and Perturbation Theory	61
E. Transmission Holography with Impulsive Sources	65

V. MISCELLANEOUS STUDIES	79
A. Model Order Criteria Applied to Autoregressive and Non-Autoregressive Processes	79
B. Application of the Energy-Moment Tensor Relation to Finite Duration Sources	81
C. Contribution of Large Earthquakes to Excitation of Polar Motion for Years 1901 to 1970	83
VI. DATA SYSTEMS	95
A. Seismic Data and Information System	95
B. Multi-Azimuth Large Array Long-Period Data Base	98
C. SRO Data Tape Processing Facility	98
D. PDP-11 Software	99
Glossary	103

SUMMARY

This is the twenty-fifth Semiannual Technical Summary report describing the activities of Lincoln Laboratory, M.I.T., in the field of seismic discrimination. These activities involve research into the fundamental seismological problems associated with the detection, location, and identification of earthquakes and nuclear explosions, and with the estimation of explosion yields. In order to investigate these problems, we are continuously improving our ability to manipulate and process seismic data from a global network of high-quality digital stations and arrays.

We are engaged in a series of related projects, all aimed at improving our understanding of body wave magnitude m_b , a quantity of considerable importance for teleseismic yield estimation. In particular, we have focused our attention on the various kinds of bias that can affect single-station and network measurements of m_b for an event. One study has reduced the large volume of magnitude data contained in the ISC Bulletin, in order to obtain values of station bias for a set of 72 stations. The resulting biases show good correlation with tectonic region, particularly in the U.S. At the same time, the results of this study indicate disturbing nonuniformity in operator performance at a number of stations.

Earlier work on attempting to remove m_b bias due to detection characteristics is continuing. We have begun a series of numerical simulations which will allow us to examine the contributions of the various different parameters, including seismicity models and instrument saturation. At the same time, we are developing various methods for the estimation of these parameters. The use of magnitudes measured with respect to a reference station appears particularly promising. Related studies are concerned with removing the bias that can arise from a combination of the shape of the source spectrum, attenuation in the earth, and instrument response. The traditional method of dividing the observed amplitude by the dominant period of the signal is only a naive approach to a complex problem. Indications are given that it will be possible to make a much more sophisticated approach to the removal of these effects.

Improvements to previous Lincoln Laboratory work on the use of ray tracing techniques to study the propagation of surface waves from sources in Eurasia have been made. Lateral heterogeneity within the oceanic lithosphere has been included by utilizing the known variation of phase velocity with age. Other surface wave studies have included an application of the seismic moment tensor formalism to the analysis of earthquake source mechanism. As an example, the case of the surface waves observed at LRSM sites from the Fallon earthquake is described.

We are concentrating our efforts in the area of evasion techniques on the problem of the separation of the signals from a closely spaced sequence of shots. The utilization of maximum entropy cepstral analysis appears, on the basis of a simulated example, to be promising. In another case, adaptive deconvolution methods are quite successful.

A variety of studies has continued our efforts to characterize lateral heterogeneity within the earth. Complexities in the P codas from some Novaya Zemlya explosions are shown to originate in a broad region which may not be associated with source or receiver region. Earlier results from a global analysis of travel-time variations have been extended. It is shown that it is possible to make a convincing correlation between the inferred velocity anomalies and the gravitational field of the earth. And another study examines the determination of levels of velocity discontinuity within the earth using free oscillation data.

Among other studies reported here are included some comparisons between various criteria that have been proposed for the determination of the optimum prediction error filter length for maximum entropy spectral analysis. Also, an extension of previous work on the energy-moment tensor relation is described. In another investigation, the observed time series for the excitation of the Chandler motion of the earth is compared with the calculated contribution due to large earthquakes. A good correlation is observed.

We have continued to develop our data and computer systems in order to be able to handle the SRO data currently on hand, and the much larger quantity of digital data soon to be available. We have designed an expansion of our CONSOLE program that permits interactive display and processing of SRO data on our PDP-7 computers. Our PDP-11 based system is already operating as an ARPANET connection, and will become a general-purpose time-sharing facility in the very near future.

M. A. Chinnery

SEISMIC DISCRIMINATION

I. BODY WAVE MAGNITUDE m_b

A. GLOBAL VARIATIONS IN STATION MAGNITUDE BIAS

In the last SATS,¹ the results of a study of body wave magnitudes reported in the USCGS earthquake data reports (EDR) lists for the first 6 months of 1971 were given. This has been extended to the entire set of station m_b observations given in the ISC Bulletins for 1964-1973, comprising over 400,000 m_b reports for nearly 40,000 events. Mean station magnitude biases have been computed for the best (in terms of events reported) 72 stations with respect to the mean magnitude of observations reported by this set of stations, in the manner previously reported. The only difference is that we have required that an event be reported by more than 15 of these 72 stations before a bias is calculated. In all cases, the distribution of biases is remarkably close to normal and is, thus, well characterized by its mean and standard deviation. In Table I-1, the size, mean, and standard deviation of the bias distribution for each of these 72 stations are given. The mean biases range from +0.37 (EDM, Canada) to -0.32 m_b units (TFO, Arizona) and the standard deviations of the distributions from 0.24 to 0.50. The means themselves are very well determined because of the large sample sizes, and the standard deviation of the mean in no case exceeds 0.02 m_b units. There is, thus, no doubt that the large variations in mean bias are statistically significant.

Biases also have been calculated for each individual year of data as well as the entire time period 1964-1973. In general, the biases show little temporal variation, but there are some stations for which the variation with time is alarming. EUR (Eureka, Nevada) shows an almost linear decrease in mean bias from +0.3 to -0.2 m_b units over 1964-1973; nearby stations in Utah show no such variation. Substantial changes in mean bias with time also were found for arrays in Montana (LASA) and Sweden (Hagsfors); the years of largest change also are those of largest variance in the distribution of biases and it appears that the magnitude reporting of these arrays was grossly degraded in certain years. In most cases, the temporal variations in bias are incapable of rational explanation.

Biases also have been calculated for a further 30 stations which reported fairly frequently. The sample sizes here are smaller and they must necessarily be considered less accurate; in particular, we cannot determine whether they vary with time or with source region. The size, mean, and standard deviation of bias for these 30 stations are given in Table I-2.

Figure I-1 shows the mean biases measured for the total of 102 stations as a function of geographical position. Negative biases imply low Q , and positive biases high Q , beneath the station. It can be seen that the biases are in accordance with other measurements of Q from, e.g., S_n propagation,² long-period teleseismic P- and S-wave amplitudes,³ and surface wave attenuation.⁴ Q is lowest in the region of mid-ocean ridges and "rift" structures such as the western U.S. and East Africa, and highest in stable regions such as shields, aseismic platforms, and deep ocean basins.

Figure I-2 shows the biases for stations in the continental U.S. on a larger scale. The difference in attenuation between the western and eastern U.S. is immediately apparent. The dashed lines separate regions of negative and positive bias. Notable exceptions to this rule are the Vela stations WMO and CPO; this may be partly due to the response characteristics of the

TABLE I-1
MEAN BIASES FOR 72 STATIONS

Station	Number of Events†		Mean Bias	Standord Deviation‡	Station	Number of Events†		Mean Bios	Stondord Deviation‡
	N ₃	N ₁₅				N ₃	N ₁₅		
ALE	1390	1160	-0.04	0.29	KRR	3159	1047	-0.24	0.30
ALQ	5205	1917	-0.20	0.33	KTG	2221	1798	+0.02	0.30
ASP	1813	466	-0.05	0.35	LAO	10202	1705	-0.10	0.47
BHA	2829	980	-0.28	0.32	LJU	2501	1739	+0.29	0.30
BKS	1476	877	+0.18	0.38	LON	2093	1333	-0.30	0.37
BMO	26192	3777	-0.29	0.35	LOR	1879	1147	+0.06	0.42
BNG	3944	1029	-0.07	0.50	LPS	1448	679	+0.04	0.34
BNS	1975	1695	+0.20	0.29	MBC	2327	1256	+0.14	0.34
BOZ	2748	978	-0.06	0.31	MOX	4645	2762	+0.02	0.27
BUL	4793	1368	-0.07	0.29	MUN	1738	397	+0.15	0.37
CAN	2462	507	-0.02	0.40	NAO	3399	755	-0.09	0.29
CAR	1289	674	+0.13	0.38	NDI	1653	906	+0.33	0.37
CIR	2623	938	-0.27	0.30	NEW	2116	1221	+0.05	0.30
CLL	2726	1715	+0.20	0.32	NIE	1566	1096	-0.02	0.33
CLK	2451	902	-0.27	0.28	NOR	3693	1986	-0.14	0.33
COL	11418	2579	+0.01	0.33	NP-	3934	1035	-0.00	0.38
COP	1457	1290	+0.36	0.26	NUR	7256	3149	+0.19	0.30
CPO	11569	2510	-0.07	0.35	PMG	4435	1146	+0.10	0.38
DUG	6117	1753	-0.15	0.35	PMR	6016	2075	-0.08	0.37
EDM	1709	1181	+0.37	0.28	PNT	1178	663	+0.13	0.30
EKA	3094	1395	+0.00	0.33	POO	2841	1288	+0.17	0.36
EUR	14997	2913	-0.24	0.40	PRE	1947	802	-0.07	0.39
FUR	2498	1816	+0.10	0.38	PRU	2779	2210	+0.04	0.24
GDH	1439	1257	+0.00	0.34	RES	1435	1064	+0.13	0.37
GIL	6138	1842	-0.04	0.35	RIV	1730	507	+0.31	0.33
GOL	4058	1770	-0.28	0.39	SHL	2753	769	+0.11	0.33
GRF	1450	1104	+0.24	0.28	SJG	1547	718	+0.24	0.38
HFS	2917	895	+0.05	0.45	STU	1752	1434	+0.29	0.31
HYB	2106	1166	+0.19	0.37	TFO	18546	2395	-0.32	0.35
KEV	3678	2218	+0.02	0.27	TRN	1337	704	+0.07	0.35
KHC	4092	2720	+0.10	0.26	TSK	2762	1047	-0.07	0.45
KJF	2137	1036	+0.09	0.28	TUC	3033	1263	-0.14	0.25
KJN	6940	2400	+0.14	0.30	TUL	2820	1152	+0.21	0.32
KOD	2294	1210	+0.06	0.31	UBO	23157	2828	-0.11	0.38
KON	1442	1093	+0.07	0.30	WIN	1259	643	-0.09	0.43
KRA	1743	1251	+0.22	0.29	WMO	13101	1658	-0.17	0.31

†N₃: number of events reported by 3 or more stations.
N₁₅: number of events reported by 15 or more stotions.

‡Standord deviation of distribution of magnitude bioses.

TABLE I-2
MEAN BIASES FOR 30 SUPPLEMENTARY STATIONS

Station	Number of Events [†]	Mean Bias	Standard Deviation [‡]
ABU	702	+0.29	0.53
ATL	213	+0.35	0.51
BRG	749	-0.11	0.26
BUH	414	-0.04	0.38
DAG	394	-0.02	0.27
ESK	650	+0.19	0.37
FFC	568	+0.08	0.29
FLO	495	+0.26	0.31
GBA	350	+0.04	0.37
ILG	314	+0.04	0.42
INK	904	+0.15	0.29
KBL	578	+0.09	0.31
KLG	639	-0.02	0.45
LHN	476	-0.15	0.36
LPB	455	+0.07	0.31
MAW	190	+0.11	0.35
MTD	432	-0.22	0.30
OIS	392	-0.08	0.41
PAE	248	-0.03	0.29
PMO	277	+0.08	0.35
PNS	370	-0.08	0.45
PPN	233	-0.19	0.32
PPT	237	+0.06	0.29
RAB	766	+0.12	0.43
RCD	264	+0.24	0.31
ROL	392	+0.19	0.31
RUV	227	+0.09	0.37
TPT	299	+0.06	0.34
TVO	235	+0.08	0.28
VAH	283	+0.02	0.32

[†] Number of events reported by 15 or more stations.

[‡] Standard deviation of distribution of magnitude biases.

instruments, which are capable of recording much shorter period signals than conventional (e.g., WWSSN) equipment. Division of reported amplitude A by dominant period T does not entirely compensate for the much higher attenuation at these shorter periods.

An obvious application of these biases is their use as station magnitude corrections to reduce scatter in magnitude observations for a single event. We define the "scatter" of station m_b observations relative to the average m_b by

$$\sqrt{\frac{\sum_i^{N_e} \sum_j^{N_i} (m_{ij} - \bar{m}_i)^2}{N_r - N_e}}$$

for events in a particular magnitude range $m_b \rightarrow m_b + \Delta m_b$, where N_e is the total number of events in the magnitude range with a total of N_r associated station observations, there being N_i (≥ 3) observations m_{ij} for each event of average magnitude \bar{m}_i . Figure I-3 shows the scatter as defined above, with $\Delta m_b = 0.1 m_b$ units, for the 38,316 events of $N_i \geq 3$ during 1964-1973, prior to and after application of the mean station biases as magnitude corrections. The biases have been obtained from the 4668 events with $N_i \geq 15$, nearly all $5.0 < m_b \leq 6.5$. Application of the corrections has decreased the scatter by at least 15 percent not only in this magnitude range but also down to $m_b = 4.3$. Below $m_b = 4.0$, the scatter has been increased; this is presumably because, through the efforts of detection characteristics, our biases are not valid at these low magnitudes. Clearly, the scatter could be further reduced by applying different bias corrections for each seismic region (and year!). Unfortunately, we could find little rational explanation for the yearly variation in station bias, and no consistency in regional biases across small receiver areas; these problems should be resolved before more sophisticated station corrections are applied.

R. G. North

B. SOURCE REGION VARIATIONS IN BIAS

We may consider the mean station bias \bar{b} as defined in Sec. A, above, to consist of the following factors

$$\bar{b} = b^s + b^{cs} + b^{us} + b^M + b^{ur} + b^{cr}$$

where b^{cs} and b^{cr} are introduced by crustal structure at the source and receiver, respectively, b^{us} and b^{ur} by upper mantle structure in the same regions, b^M in the lower mantle part of the ray path, and b^s by the source radiation pattern. All these factors clearly may depend upon the source-receiver configuration through source take-off angle and receiver arrival angle. The Gutenberg-Richter distance-depth correction may be considered to approximate the effects ($b^{cs} + b^{us} + b^M + b^{ur} + b^{cr}$) globally; the biases measured then really measure deviations from this average behavior. The term b^s accounts for deviations from the average amplitude in a small region surrounding the source due to radiation pattern effects. Station site effects, e.g., seismometer-ground coupling variations due to the medium (hard rock, alluvium) upon which the station is situated, are included in b^{cr} .

Seismic sources, by their very nature, have a tendency to be located in regions of high lateral inhomogeneity and, thus, it may be expected that features such as the anomalously high attenuation on the concave side of island arcs² can seriously affect m_b determinations. Studies

leading to the development of plate tectonic theory have indicated consistency of fault plane solutions and, thus, presumably radiation patterns and b^S over large source regions.

The sources used in Sec. A have been separated into 11 major source regions, shown in Fig. I-4, and biases computed in the same manner as before for events from each of these source areas reported at a given station. A value of mean bias is not calculated unless there are at least 100 events in any particular source region data sample.

For 16 of the 72 stations of Sec. A, the mean bias for any one particular source region differs by more than $0.2 m_b$ units from the mean bias for all source regions given in Table 1-1. For three stations in highly heterogeneous seismic regions (PMG, New Guinea; PMR, Alaska; and TSK, Japan), it differs from the mean bias for all source regions by more than $0.3 m_b$ units. It must be noted here that for some stations there are an insufficient number of events for individual source region biases to be calculated and, thus, comparison of biases from different regions is severely limited to the better stations. For some of the best stations, e.g., TFO, UBO, WMO which have reported many events from various source regions, the variation of bias with source region is, however, less than $0.2 m_b$ units.

Many of the stations considered here happen to be concentrated in regions which are small in extent compared to source-receiver distances and we may therefore expect to see consistencies in the variations of mean bias with source region. Three particularly small receiver regions are those containing stations in Germany, East Africa, and the western U.S. Table 1-3 gives the variations of bias with source region for each of these areas.

It can be seen that, even over these small receiver regions, there is remarkably little consistency in variations of mean bias with source region, the only possible exception being that for events in region 4 (Japan) to the western U.S. Similar tables for other receiver areas such as Scandinavia and India also fail to reveal any correlation of bias with source region. Had we selected smaller source regions, it is likely both that regional variations in bias and their consistency across receiver areas would have been more pronounced, particularly in the case of ray paths traveling down descending lithospheric slabs. Unfortunately, the data base is insufficient to test this.

This lack of correlation may be taken to indicate that the terms $(b^{CS} + b^{US} + b^M)$, however large they may be for individual ray paths, tend to average out in such a manner that they cannot be resolved in the present study. It also indicates that the Gutenberg-Richter distance-depth correlation is not grossly in error. In particular, much of the observed station bias may be due to the term b^{ur} , and its variation with source region to b^{cr} . This does not of course imply that b^{CS} and b^{US} are not as large as b^{cr} and b^{ur} ; in fact, the greater lateral heterogeneity in source regions probably means that they will be larger, but they cannot be resolved by the present means.

R. G. North

C. TEMPORAL VARIATIONS IN THE SHAPE OF THE MAGNITUDE-FREQUENCY CURVE

Variations in the shape of the magnitude-frequency curve and, in particular, the slope b of the (dubiously) linear portion of the curve, where b is given by $\log N = a - bm$, N being the number of events of magnitude $\geq m$ (a and b constants), have been interpreted⁵ as indicative of changes in the state of stress in the earth's crust with source region and/or time. In a previous SATS,⁶ it has been shown that these variations in b are of dubious statistical significance.

TABLE I-3 VARIATIONS OF STATION BIAS WITH SOURCE REGION (With Respect to the Bias Values Listed in Table I-1)											
Station	Source Region (See Fig. I-4)										
	1	2	3	4	5	6	7	8	9	10	11
Germany											
BNS				-0.09	+0.01	+0.02				-0.08	
CLL			-0.04	-0.01	+0.18	-0.04				-0.21	
FUR			+0.21	+0.04	-0.09	-0.15				+0.07	+0.01
GRF				+0.09	0.0					0.0	
MOX			+0.05	-0.04	+0.09	-0.03	+0.25			-0.07	
STU				+0.12	+0.03	-0.13					
East Africa											
BHA			+0.05	+0.10						+0.01	-0.16
CIR			+0.04						+0.15	-0.03	-0.02
CLK			-0.15						+0.07	-0.21	+0.23
KRR			-0.06						+0.10	+0.05	+0.08
Western U. S.											
DUG	-0.10			-0.08	-0.07	-0.07	+0.07	-0.10	+0.18		
EUR				-0.08	+0.05	-0.07			-0.01		
TFO				-0.09	-0.13	-0.06	0.0		+0.15		
TUC					-0.25	+0.02			+0.08		
UBO				-0.13	-0.03	+0.03	+0.05	-0.01	0.0		-0.09

We consider here the effects of temporal changes in the set of stations reporting m_b values in the ISC Bulletins for 1964-1973 upon the shape of magnitude-frequency curves. Such changes may be expected if the proportion of stations reporting which have large negative or positive magnitude biases (see Sec. A, above) changes with time. An inspection of the set of stations reporting m_b values for each year of 1964-1973 reveals that this indeed may be the case. For the first six years of this period, a very large proportion of all m_b reports was from stations in the western U.S.; this proportion declined considerably over 1970-1973. Since low upper mantle Q beneath the western U.S. causes substantial negative magnitude biases for stations in this region (see previous section), this implies that average m_b values for the earlier time period will be lower than later ones, relative to "true" m_b . Figure I-5 shows the total number of station m_b reports per year for (a) all stations, and (b) stations in the western U.S. as a function of year. It can be seen that the proportion of station m_b reports from western U.S. stations has declined from over 60 percent in 1964-1965 to 30 percent in 1970-1973. The largest change occurs during 1969-1970.

The seismicity studied has been separated into that for 1964-1969 and 1970-1973, and the annual number of events, in m_b increments of 0.1, for these intervals compared with that for 1964-1973. Figure I-6(a) shows ratios of annual seismicity for each of the time periods 1964-1969 and 1970-1973 to that for 1964-1973. It is clear that during the earlier time period there were many more events reported of lower magnitudes, and slightly less at higher magnitudes, than in the later time period. Application of the station biases determined in the previous section as corrections to station magnitudes before calculation of average m_b [Fig. I-6(b)] reduces the difference in numbers of events of $m_b \geq 4.6$ between the two time periods by a factor of 2. There are still many more events at lower magnitudes for the earlier time period; this is due to the remarkable detection performance of the 5 Vela short-period arrays (BMO, CPO, TFO, UBO, and WMO). These stations closed down (TFO, WMO), or reported a smaller proportion of later events during 1969-1970. Obviously, the detection capability of the global network of stations, as measured in terms of m_b , has been seriously degraded by the removal of these Vela stations. It is surprising that although there are more stations reporting in later years, they do not do as well at lower magnitudes as the fewer stations of 1964-1969.

It can be concluded that temporal changes in station distribution can cause variations in the distribution of event magnitudes reported by a global network. Similar regional changes also can be expected as the location of stations relative to world seismicity varies.

R. G. North

D. COMPARISON OF RECENT ESTIMATES OF MAGNITUDE BIAS

In Sec. A, we have presented a set of station biases determined directly from station amplitude readings. It is interesting to compare these results with two recent studies of magnitude bias by Marshall⁷ and Evernden.⁸ Table I-4 lists the biases from all three studies for a set of stations common to at least two studies. Results from Marshall and Evernden have each been subjected to a base line correction so that station COL (College, Alaska) has the value +0.01 in each case.

The results of Marshall⁷ (kindly supplied to us in advance of publication) were obtained using estimates of the mean attenuation coefficient Q of the crust and upper mantle beneath the receiver obtained from observations of P_n velocity. The general agreement with the Lincoln

TABLE I-4
COMPARISON OF ESTIMATES OF STATION MAGNITUDE BIAS

Station	Magnitude Biases			Station	Magnitude Biases		
	Table I-1	Marshall ⁷	Evernden ⁸		Table I-1	Marshall ⁷	Evernden ⁸
TFO	-0.32	-0.21	-0.25	COL†	+0.01	+0.01	+0.01
BMO	-0.29	-0.21	-0.25	KEV	+0.02	+0.06	+0.37
GOL	-0.28	-0.23		LPS	+0.04		+0.04
ALQ	-0.20	-0.23	-0.17	HFS	+0.05	+0.03	
WMO	-0.17		-0.18	KOD	+0.06		-0.12
DUG	-0.15	-0.28	-0.31	TRN	+0.07	+0.15	
NOR	-0.14	-0.12	+0.20	KON	+0.07	-0.05	+0.16
UBO	-0.11	-0.21	+0.03	KHC	+0.10	+0.10	
LAO	-0.10	+0.01		PMG	+0.10		+0.21
WIN	-0.09		+0.12	SHL	+0.11		-0.02
NAO	-0.09	-0.05		KJN	+0.14	+0.06	
BUL	-0.07		-0.01	POO	+0.17	+0.15	+0.22
PRE	-0.07		+0.23	HYB	+0.19	+0.15	
CPO	-0.07	+0.10	+0.06	SJG	+0.24		+0.24
BOZ	-0.06		-0.21	STU	+0.29	+0.01	+0.27
ALE	-0.04	-0.12		NDI	+0.33	+0.15	+0.18
EKA	0	+0.01		EDM	+0.37	+0.10	

† Reference station.

Laboratory results is excellent (differences in estimated bias seldom exceed $0.1 m_b$ units). It is interesting to note, however, that the total range of biases given by Marshall is approximately $0.4 m_b$ units, compared with a range of nearly $0.7 m_b$ units in the present study.

Marshall's results raise the possibility that there may be some correlation between station magnitude bias and local P_n velocity. To test this, Fig. I-7 shows a plot of bias against P_n velocity for 40 stations. The P_n values are those obtained by Marshall (private communication). A definite trend is seen, which may be approximated by the expression

$$\text{bias} = (P_n \text{ velocity}) - 8.05 \quad .$$

Because of the scatter in the data points, we do not suggest that this relation has a useful predictive capability. It is interesting, however, and gives some support to the arguments of Marshall.⁷

In a second recent study, Evernden⁸ has estimated station biases using a relationship between bias and background noise level presented in an earlier paper.⁹ The agreement of these results with the first two studies is reasonably good, in most cases.

In addition to P_n velocity and background noise level, a third parameter which might be expected to correlate with station magnitude bias is the station travel time correction. Figure I-8 shows a plot of magnitude bias against the station corrections listed by Herrin and Taggart.¹⁰ Quite clearly, there is no correlation between these parameters.

M. A. Chinnery
R. G. North

E. SEISMIC MAGNITUDE SIMULATION STUDIES

A statistical model for the seismic magnitudes measured at a network of stations was formulated in our last SATS.¹ Some implications of the model were developed as were algorithms for the estimation of model parameters and magnitude. The basic model continues to be used to interpret magnitude data, and it was felt that computer simulations should be done to allow various controlled experiments in which all model parameters and event magnitudes were known. Such a simulation may indicate how the model might be reformulated to better represent actual data, and we plan to apply proposed estimation algorithms to simulated data to evaluate their performance.

A simulation program has been written which is in terms of individual station magnitudes and does not take account of geographical distribution of either stations or events. The simulation generates a sequence of true magnitude values and for each of these randomly generates the magnitudes seen at a network of stations. The user specifies the number of stations which must detect to declare an event detected by the network. The program outputs the simulated magnitude data as well as the true magnitude for each event detected. All this is driven by a pseudo-random number generator subroutine. The main input options are as follows.

1. True Magnitude Distributions

- (a) The user can select to generate true magnitude values by sampling from a probability density function which is of the form $Ce^{-\beta m}$ on an interval from $m = m_0$ to $m = 7.0$. C is automatically selected to properly normalize the distribution. The user can choose the minimum magnitude m_0 and the slope β of the seismicity curve. This choice for the

generation of true magnitude corresponds to the common assumption of a linear relation between average number of events and magnitude. The nominal assumption of a factor of 10 change in the number of events for each magnitude unit is equivalent to using $\beta = \ln 10 \approx 2.3$.

- (b) A second alternative is that all events have the same true magnitude. In this case, the user selects the value.
- (c) The third alternative is for the user to supply a special subroutine which allows him to specify any probability density function at all for the true magnitudes.

2. Bias and Scatter Parameters

Given true magnitude m the predetection magnitude at station i is given by:

$$m_i = m + B_i + \epsilon_i \quad (\text{I-1})$$

where B_i is a constant bias and ϵ_i is a zero-mean Gaussian random variable with standard deviation σ_i . The user must specify the B_i and σ_i values.

3. Station Detection Characteristics

- (a) The basic option for the detection characteristics of a station is that the probability of detection is:

$$\text{Pr} [\text{detection} / m_i] = \Phi \left(\frac{m_i - G_i^*}{\gamma_i^*} \right) \quad (\text{I-2})$$

where Φ is the error function, G_i^* is the 50-percent detection threshold, and γ_i^* determines the rate at which the probability goes from zero to one. The user supplies the G_i^* and γ_i^* . For a given m_i , the simulation randomly (using the proper probability) decides if a detection has occurred. It then reports either m_i or the "not seen" value.

- (b) In recognition that the error function may not be a satisfactory detection curve in all cases, the program allows the user to supply a subroutine which can modify the basic detection curve. The problem of saturation of stations for large events can be conveniently accommodated using this option.

One imminent application of the magnitude simulation program is to check for the possible influence of station detection characteristics upon the station bias estimates obtained by North (see Sec. A). Given North's station bias estimates plus estimates of other model parameters, we can generate simulated magnitudes for a network. The algorithms used by North to estimate biases can then be applied to these data to see if the now known biases built into the model will be regenerated by the estimation algorithms.

The model parameters required to complete such an experiment are the seismicity parameter β , the scattering parameter σ_i , and the detection parameters G_i^* and γ_i^* . An effort has

been made to obtain estimates of the G_i^* and γ_i^* which could be used for the experiment. These estimates are probably not optimal but should be adequate for the application at hand.

A log-likelihood function for the estimation of seismicity and detection parameters of a single station in terms of the reported amplitudes and periods at a station was given in our last SATS.¹ In terms of station magnitudes, this becomes

$$\ln L_i = \sum_{j=1}^{N_i} \left[\ln \beta + \beta(G_i^* - \frac{1}{2} \beta \gamma_i^{*2}) + \ln \Phi\left(\frac{m_{ij} - G_i^*}{\gamma_i^*}\right) \right] \quad (I-3)$$

where i indicates the station, N_i is the number of events detected at station i , and j is the index on the events. We have written and used a program to search the β , G_i^* , γ_i^* space for the maximum value of

$$C = \sum \ln L_i$$

and to thus estimate β , G_i^* , and γ_i^* . For the results given below, the grids for this search were:

$$\begin{aligned} \beta &= 1.5 \text{ to } 2.4 \text{ in steps of } 0.1 \\ G_i^* &= 3.4 \text{ to } 5.8 \text{ in steps of } 0.1 \\ \gamma_i^* &= 0.1 \text{ to } 0.55 \text{ in steps of } 0.05 \end{aligned}$$

A preliminary simulation for 15 stations and 7500 detected events was run with seismicity parameter $\beta = 2.3$, $\sigma_i = 0.3$ for all stations, and other parameters as given in Table I-5. Parameters were selected arbitrarily. The object was to check the estimation algorithms with simulated data using known parameter values. Given the quantizations used for estimation and the small number of events, performance was quite satisfactory. The seismicity parameter was underestimated as 2.1 rather than the correct 2.3 value. Estimates of \hat{G}_i^* and $\hat{\gamma}^*$ are also good with some tendency to underestimate. The bias at some stations caused no problem. The quality of estimates generally decreased with the number of magnitude reports available. In anticipation of results with real data, we note that when we assigned $\beta = 1.6$ for estimation purposes (although the true value was 2.3), the resulting detection parameter estimates did not change very much. As might be expected, the estimated 50-percent detection thresholds decreased when β was fixed at the lower value.

Table I-6 shows the results obtained using real data. Based upon numbers of reports to the ISC, North selected a set of 72 stations to study in detail. We used the data from those stations from 1964 through 1973. No data from 1969 were used due to a technical problem. The number of available reports per station ranged from 1106 for WIN to 27,915 for BMO. The search over β as well as detection parameters gave the unexpected low value of $\hat{\beta} = 1.6$. The estimated 50-percent detection magnitudes ranged from 3.8 to 5.4 and the scatter parameters cluster near 0.3. The estimates of 50-percent threshold increased by 0.0 to 0.2 magnitude unit when β was fixed at the value 2.3.

Some additional work is required but we believe that we now have estimates of most parameters needed so that, given North's bias estimates, we can undertake a meaningful simulation. Our next step will be to verify within the context and assumptions of our model that the station bias estimates obtained by North have not been excessively influenced by station detection characteristics.

R. T. Lacoss
M. A. Chinnery

TABLE I-5
ESTIMATE OF DETECTION CHARACTERISTICS
AND SEISMICITY FROM SIMULATED DATA FOR 15 STATION†

Station	Number of Reports	Model Parameters			Estimated Parameters			
					$\hat{\beta} = 2.1$		$\beta = 1.6$	
		Bios	G_i^*	γ_i^*	\hat{G}_i^*	$\hat{\gamma}_i^*$	\hat{G}_i^*	$\hat{\gamma}_i^*$
1	5451	-0.3	3.8	0.2	3.8	0.15	3.7	0.15
2	4350	-0.3	3.9	0.2	3.9	0.20	3.8	0.15
3	3510	-0.3	4.0	0.2	4.0	0.20	3.9	0.15
4	3582	-0.2	4.1	0.2	4.1	0.20	4.0	0.15
5	2886	-0.2	4.2	0.2	4.2	0.20	4.1	0.15
6	2293	-0.2	4.3	0.2	4.3	0.20	4.2	0.15
7	2221	-0.1	4.4	0.2	4.4	0.15	4.3	0.10
8	1891	-0.1	4.5	0.2	4.5	0.20	4.4	0.15
9	1512	-0.1	4.6	0.2	4.5	0.15	4.5	0.15
10	1513	0.0	4.7	0.2	4.7	0.20	4.6	0.15
11	1228	0.0	4.8	0.2	4.8	0.15	4.7	0.15
12	995	0.0	4.9	0.2	4.9	0.15	4.8	0.15
13	743	0.0	5.0	0.2	4.9	0.10	4.9	0.15
14	646	0.0	5.1	0.2	5.0	0.10	5.0	0.10
15	621	0.1	5.2	0.2	5.1	0.10	5.1	0.10

† Model parameters were $\sigma_i = 0.3$, $\beta = 2.3$ and Bios, G_i^* , γ_i^* as shown in the table. Estimated detection parameters \hat{G}_i^* , $\hat{\gamma}_i^*$ shown for estimated seismicity parameter $\hat{\beta} = 2.1$ and for β improperly constrained to $\beta = 1.6$ for estimation purposes.

TABLE I-6
ESTIMATES OF DETECTION CHARACTERISTICS FOR 72 STATION†

Station	$\hat{\beta} = 1.6$		$\beta = 2.3$		Station	$\hat{\beta} = 1.6$		$\beta = 2.3$	
	\hat{G}_i^*	$\hat{\gamma}_i^*$	\hat{G}_i^*	$\hat{\gamma}_i^*$		\hat{G}_i^*	$\hat{\gamma}_i^*$	\hat{G}_i^*	$\hat{\gamma}_i^*$
CPO	4.2	0.30	4.3	0.35	KJF	4.8	0.25	4.9	0.30
TUL	4.7	0.35	4.8	0.35	KJN	4.7	0.25	4.8	0.30
WMO	4.1	0.25	4.1	0.25	KON	5.0	0.30	5.0	0.25
ALQ	4.4	0.35	4.5	0.35	NAO	3.9	0.35	4.0	0.35
BKS	5.4	0.50	5.6	0.55	NUR	4.8	0.30	4.9	0.30
BMO	3.9	0.25	4.0	0.25	EKA	4.6	0.30	4.7	0.30
BOZ	4.5	0.30	4.6	0.30	KHC	4.8	0.25	4.9	0.25
DUG	4.1	0.30	4.2	0.30	KRA	5.1	0.25	5.2	0.25
EUR	4.2	0.30	4.3	0.30	LJU	5.2	0.30	5.4	0.35
GOL	4.3	0.30	4.4	0.30	LOR	4.8	0.50	4.8	0.50
LAO	4.0	0.30	4.1	0.30	NIE	4.7	0.20	4.8	0.20
LON	4.6	0.30	4.7	0.30	PRU	5.0	0.30	5.0	0.30
NEW	4.8	0.35	4.9	0.35	BNS	5.2	0.30	5.3	0.30
TFO	3.8	0.25	3.9	0.30	CLL	4.9	0.25	5.0	0.25
TUC	4.6	0.30	4.7	0.30	FUR	5.0	0.35	5.1	0.35
UBO	3.9	0.35	4.1	0.30	GRF	5.1	0.25	5.2	0.25
BHA	4.4	0.25	4.5	0.25	MOX	4.8	0.30	4.9	0.30
BNG	4.2	0.25	4.3	0.25	STU	5.2	0.30	5.3	0.30
BUL	4.5	0.20	4.6	0.25	COL	4.5	0.35	4.6	0.30
CIR	4.4	0.25	4.6	0.30	GIL	4.5	0.35	4.6	0.35
CLK	4.4	0.25	4.5	0.25	PMR	4.6	0.30	4.7	0.35
KRR	4.4	0.20	4.5	0.20	GDH	5.0	0.35	5.1	0.35
PRE	4.6	0.25	4.8	0.30	KTG	4.9	0.35	5.0	0.35
WIN	4.6	0.25	4.7	0.25	NOR	4.6	0.25	4.7	0.25
HYB	5.1	0.35	5.2	0.30	ALE	4.9	0.30	5.0	0.30
KOD	4.9	0.30	5.1	0.35	MBC	4.8	0.40	4.9	0.40
NDI	5.2	0.35	5.3	0.30	NP-	4.3	0.30	4.4	0.30
POO	5.0	0.50	5.2	0.55	RES	5.0	0.40	5.1	0.35
SHL	4.7	0.30	4.8	0.30	EDM	5.3	0.35	5.3	0.35
ASP	4.6	0.30	4.7	0.30	PNT	4.9	0.25	5.0	0.25
CAN	4.7	0.30	4.8	0.30	TSK	4.7	0.40	4.9	0.45
MUN	5.0	0.30	5.1	0.30	TRN	4.9	0.25	5.0	0.30
RIV	5.3	0.30	5.4	0.30	LPS	4.8	0.30	4.9	0.30
COP	5.4	0.25	5.5	0.25	SJG	4.9	0.35	5.0	0.30
HFS	4.2	0.35	4.3	0.35	CAR	4.9	0.25	5.0	0.25
KEV	4.9	0.25	5.0	0.25	PMG	4.8	0.25	4.9	0.25

† Computed using station magnitude reports from 1964 through 1973 except for 1969. Estimates of 50-percent threshold \hat{G}_i^* and spread factors $\hat{\gamma}_i^*$ shown for seismicity parameter $\hat{\beta} = 1.6$ which resulted from searching over β and for β constrained to 2.3 for estimation purposes.

F. MAGNITUDE DIFFERENCES BETWEEN STATION PAIRS

In the previous work,¹ an expression was given for the expected value of the magnitude m_2 observed at station 2, given the magnitude m_1 observed at station 1. This may be conveniently rewritten in terms of the magnitude difference $m_2 - m_1$, as follows:

$$E[(m_2 - m_1)/m_1] = B_2 - B_1 - \beta\sigma_1^2 + \frac{\sigma_1^2 + \sigma_2^2}{\sqrt{\sigma_1^2 + \sigma_2^2 + \gamma_2^{*2}}} \times Z \left\{ \frac{m_1 + B_2 - B_1 - \beta\sigma_1^2 - G_2^*}{\sqrt{\sigma_1^2 + \sigma_2^2 + \gamma_2^{*2}}} \right\}. \quad (I-4)$$

This formula is derived assuming a linear frequency magnitude relation of the form

$$\ln N = \alpha - \beta m \quad . \quad (I-5)$$

The parameters involved¹ are as follows:

B_i = bias of station i

σ_i^2 = variance of magnitude readings at station i

G_i^* = detection threshold of station i

γ_i^2 = variance of detection probability curve for station i .

The function $z(x)$ is defined as previously.¹

Equation (I-4) is interesting for several reasons. It shows that the magnitude difference $(m_2 - m_1)$, averaged at each value of m_1 , has an expected value independent of the detection characteristics of m_1 . Furthermore, the appearance of the quantity β in the expression suggests that information about the seismicity distribution, Eq. (I-5), can be obtained even though the data used in the evaluation of $E[(m_2 - m_1)/m_1]$ are not complete.

As a test of the usefulness of Eq. (I-4), we report here the results of plotting the average value of $(m_2 - m_1)$ against m_1 for several station pairs. The data used were those of the Bulletin of the International Seismological Center (ISC), for the years 1966-1970, which are available on tape. For a given station pair, events were selected that had a recorded magnitude at each station, and which lay in the distance range 30° to 90° from each station (to minimize possible errors in the distance correction).

An example of the resulting data is shown in Fig. I-9, for the station pair TFO - UBO, using reference station UBO. The points show the average value of the magnitude difference $m_{TFO} - m_{UBO}$, at increments of $0.1 m_b$ units in m_{UBO} . The vertical bars indicate 2 standard deviations on either side of the mean (i.e., 95-percent confidence bounds). Approximately 600 measurements were used in the determination of each point in the range $4.0 \leq m_{UBO} \leq 4.5$. Fewer observations were available outside this range, and this is reflected in the error bounds associated with each mean.

The solid curve shows the prediction of Eq. (I-4) using the following parameters:

$$B_2 - B_1 - \beta\sigma_1^2 = -0.40$$

$$\sigma_1^2 + \sigma_2^2 = 0.19$$

$$G^2 = 3.68$$

$$\gamma_2 = 0.32 \quad .$$

A very good fit can be obtained, though some questions about the uniqueness of these parameters remain.

A similar curve can be obtained from the same two stations, but using TFO as a reference. This is shown in Fig. I-10. The curve through the data corresponds to the parameters:

$$B_2 - B_1 - B\sigma_1^2 = -0.01$$

$$\sigma_1^2 + \sigma_2^2 = 0.19$$

$$G_2 = 4.15$$

$$\gamma_2 = 0.50$$

The bias levels in Figs. I-9 and -10 are consistent with the following:

$$B_{UBO} - B_{TFO} = 0.21$$

$$\sigma_{UBO} = 0.30$$

$$\sigma_{TFO} = 0.31$$

$$\beta = 2.30 \quad .$$

The difference in biases of 0.21 is in excellent agreement with the difference in bias found by a quite different method elsewhere in this report (Sec. A).

Provisional conclusions from these results are that the theoretical model appears to fit the observed data well, in certain cases. The assumption of linear seismicity appears to be valid. Note that the value $\beta = 2.30$ corresponds to a "b-value" of 1.0. In cases like those shown, it appears possible to derive valuable information on detection parameters and biases.

Other station pairs do not always behave so well. Two extreme examples are shown in Figs. I-11 and -12 for the station pairs ALQ - UBO and EUR - UBO. These curves do not show a well-defined base level. This is interpreted as being due to the effects of instrument saturation, which are overlapping with the effects of detection level in the range $5.0 \leq m_b \leq 5.5$. Efforts to extract useful parameters in cases of this type are continuing.

M. A. Chinnery
R. T. Lacoss

G. ESTIMATION OF SEISMIC SOURCE AT 1 Hz FROM $\log(A/T)$

Short-period magnitudes have traditionally been calculated by $m_b = \log(A/T) + Q(\Delta, h)$, where A is the waveform amplitude, peak to trough, corrected for instrument response at period T , and $Q(\Delta, h)$ is the Gutenberg-Richter correction for geometric spreading as a function of epicentral distance Δ and depth of focus h .

$\log(A/T)$ after instrument correction is usually interpreted to be a measure of the source energy at 1 Hz arriving at the seismometer. This is approximately true, but the effect of source function and instrument response on the time-domain waveform can produce a bias which varies with the corner frequency of the source model and the type of high-frequency decay, e.g., ω -square or ω -cube. Furthermore, earth attenuation which is frequency dependent has an effect which is not properly incorporated in the $Q(\Delta, h)$ term for obtaining m_b from $\log(A/T)$.

Figures I-13, -14, and -15 show curves of corrected $\log(A/T)$ for three source models, recorded on the standard short-period Vela seismometer. The Sharpe¹¹ and Brune models^{12,13} decay as ω^{-2} at high frequencies, and the Savage model¹⁴ decays as ω^{-3} . The spectra for these models are scaled so that at 0 Hz, the amplitude equals f_0^{-3} , where f_0 is the corner frequency. The spectra and time-domain waveforms are shown in Figs. I-21, -22, and -23.

In each of Figs. I-13, -14, and -15, the displacement source at 1 Hz is shown as a dashed line. The three curves show the effect of including earth attenuation, using a causal attenuation operator given by Carpenter.¹⁵ From these figures it is clear that there is a significant bias of $\log(A/T)$ about the source displacement at 1-sec period, which varies with attenuation and corner frequency of the source model. Curiously, the attenuated source with a $t^* = 0.25$, when passed through the seismometer produces an A/T value, which when corrected for Vela seismometer response is closest to the unattenuated source spectrum at 1 Hz, over a wide range of corner frequencies.

The bias of corrected values of $\log(A/T)$ from the source spectrum at 1 Hz is displayed in Fig. I-16 for each source model and several values of t^* as a function of corner frequency. One sees that the biases for the ω^{-2} and ω^{-3} models are rather similar for corner frequencies down to ~ 0.25 Hz.

One can calculate m_b for corner frequencies f_0 of explosions by using empirical relations for yield Y in kilotons, equivalent cavity radius a in meters and m_b (Ref. 16). If we assume that

$$a \sim 100 Y^{1/3}$$

$$m_b \sim 3.8 + \log_{10} Y$$

and

$$f_0 = \frac{\alpha}{\sqrt{3}\pi a}$$

in the Sharpe model, then, we can calculate m_b as a function of a . This gives

$$m_b \sim 3 \log(167/f_0)$$

where we have assumed that $\alpha = 5$ km/sec. Values of explosion m_b are tabulated between the biases for the Sharpe and Brune models in Fig. I-16. These m_b values are rough averages, so that individual events may not have corner frequencies consistent with the m_b scale shown. Also shown in Fig. I-16 are the estimates of corner frequencies for the explosion Milrow and four Aleutian earthquakes measured by Wyss, Hanks, and Liebermann from long-period teleseismic records.¹⁷ It is apparent that the corner frequencies for these earthquakes are an order of magnitude lower than for Milrow for roughly comparable m_b .

For smaller magnitude explosions between m_b 4 and 5, it appears that the bias may be higher than for earthquakes of similar magnitude, along similar transmission paths. This should produce a measurable effect on the $M_s:m_b$ discrimination criterion at low magnitudes.

The bias described above should vary with instrument response. We plan to calculate similar biases for WWSSN and SRO recording systems, and determine the necessary corrections for $\log(A/T)$ to obtain consistent estimates of the source spectrum at 1 Hz.

C. W. Frasier

H. EVIDENCE FOR ω -CUBE SCALING FROM SHORT-PERIOD AMPLITUDES AND PERIODS OF THE RAT ISLAND SEQUENCE (1965)

We are studying the effect of seismic scaling directly in the time domain by analyzing the amplitudes and periods of teleseismic P-waves from moderate-sized earthquakes of the Rat Island sequence. The motivation for this study is the clear linear trend of log amplitude with period for this sequence reported by USGS EDR. In the previous SATS,¹ we showed the trend of $\log(A/T)$ vs T for over 300 events recorded at four Vela arrays. Since then we have extended the data base to 868 events recorded at five Vela arrays and four WWSSN stations. We have also generated synthetic records of the far-field displacement including instrument response and earth attenuation for two ω -square models proposed by Sharpe¹¹ and Brune,^{12,13} and an ω -cube model by Savage.¹⁴

Under the assumption of geometric similarity of small- and moderate-sized earthquakes, it can be seen that predicted variations of $\log(A/T)$ with T are quite different for ω -square and ω -cube models when the corner frequency moves through the short-period band. Using the Vela station data, we can demonstrate that the ω -square models may be rejected in favor of the ω -cube model suggested by Savage.

The recording stations and the aftershock area are shown in Fig. 1-17. The Vela arrays are BMO, UBO, TFO, WMO, and CPO. They fall in the azimuthal sector 150° to 170° from the source region, and within the distance range 44° to 68° . WWSSN stations EUR and ALQ are located within the above sector, and stations COL and NUR outside the sector.

Figure I-18(a) shows the scatter of reported amplitudes with periods at the Vela station BMO with a histogram of the amplitudes in Fig. 1-18(c). In Fig. 1-18(b) the mean and standard deviation of the log amplitude values are displayed as a function of T . The linear trend of $\log A$ with period is quite striking and is typical of the data from the other Vela stations. In Fig. I-18(d), $\log(A/T)$ vs period is displayed, and the clear trend with T is still apparent although the slope is smaller. In the figures which follow, we plot $\log(A/T)$ rather than $\log A$ simply because it is a measure of m_b , and we shall attempt to relate m_b to corner frequency for these data.

The $\log(A/T)$ values for the four other Vela stations are shown in Fig. 1-19. The numbers for each station equal the number of events reported during the time period scanned in the EDR. Although some data scatter is apparent, the mean values of $\log(A/T)$ clearly increase with T over a wide range of periods with similar slopes at all Vela stations.

Figure I-20 contains similar plots of amplitudes reported by four WWSSN stations. In this figure, we see an increase in $\log(A/T)$ with T at EUR and NUR, but no reliable increase at ALQ and COL. Comparing this figure to Fig. 1-19, one can see several important differences between reported amplitudes at Vela and WWSSN stations. First, the number of events reported by Vela stations is 2 to 10 times the number reported by the WWSSN stations. The range of reported periods is wider at the Vela stations, and the lower limit of average amplitudes at short periods is below the lower limits at the standard stations. In terms of data quality and consistency of reported amplitudes, it appears that the Vela arrays, while operating, performed much better than the standard stations. This is discussed in another section on station biases by North.

The source models we used are those of Sharpe,¹¹ Brune,^{12,13} and Savage.¹⁴ We are primarily interested in scaling effects with corner frequency f_0 . Therefore, we ignore all frequency independent factors such as spherical spreading and consider only the far-field displacement wave shapes and Fourier spectra, including phase. The variation in both azimuth and

take-off angle of the rays as they leave the source is fairly small, except toward NUR and COL, so we shall assume that the variation in radiation pattern is negligible in the take-off direction to the Vela arrays.

The Fourier transforms of the scaled source functions are, in chronological order,

$$\text{Sharpe: } U_1(f) = f_0^{-3} / \{ 1 - (f/f_0)^2 + j \frac{2}{\sqrt{3}} (f/f_0) \} \quad (\text{I-6})$$

$$\text{Brune: } U_2(f) = f_0^{-3} / \{ 1 - (f/f_0)^2 + j 2(f/f_0) \} \quad (\text{I-7})$$

$$\text{Savage: } U_3(f) = f_0^{-3} / \{ 1 - 3(f/f_0)^2 + j [3(f/f_0) - (f/f_0)^3] \} \quad (\text{I-8})$$

These spectra equal f_0^{-3} at 0 frequency. In the Sharpe solution, $f_0 = \alpha / (\pi\sqrt{3}a)$ where a is the cavity radius and α is the compressional velocity of the medium.¹⁸ For a constant stress drop, the far-field spectrum scales exactly as f_0^{-3} , which is proportional to the cavity volume. This geometric similarity also is assumed to hold for the Brune and Savage source models.

Figure I-21 shows the amplitude spectra of each source model as a function of scaled frequency (f/f_0) . Sharpe and Brune displacements are ω -square models, and Savage's model is ω -cube at high frequency. In Fig. I-22, the time-domain waveforms obtained by inverting Eqs. (I-6), (-7), and (-8) are displayed as a function of scaled time $T = f_0 t$, where t is real time. These displacement waveforms are given by

$$\text{Sharpe: } u_1(t) = \sqrt{6}\pi f_0^{-2} \exp \left[\frac{-2\pi T}{\sqrt{3}} \right] \sin \left(2\sqrt{\frac{2}{3}} \pi T \right) \quad (\text{I-9})$$

$$\text{Brune: } u_2(t) = (2\pi)^2 f_0^{-2} T \exp [-2\pi T] \quad (\text{I-10})$$

$$\text{Savage: } u_3(t) = \frac{(2\pi)^3}{2} f_0^{-2} T^2 \exp [-2\pi T] \quad (\text{I-11})$$

The area of each waveform in normal time t equals f_0^{-3} , the spectral level at 0 Hz.

Synthetic records were generated for each source function using a set of corner frequencies $f_0 = 0.0625, 0.125, 0.25, \dots, 16$ Hz. The source functions were convolved with the Johnson-Matheson short-period seismometer response used at the Vela arrays,¹⁹ and a causal attenuation operator given by Carpenter.¹⁵ Figure I-23 shows the synthetic waveforms for an attenuation parameter $t^* = 0.1$, normalized to the same gain. t^* equals travel time divided by average Q .

The seismograms for the Sharpe and Brune source functions are very similar with a narrow range of pulse periods from ~ 0.3 to 0.8 sec. On the other hand, the seismograms for the Savage source show a wider range of periods from ~ 0.25 to 1.4 sec.

Similar synthetic records were calculated for attenuation parameters $t^* = 0.25, 0.50$, and 1.0 . Amplitudes and periods were measured and amplitudes were corrected for Vela instrument response. Corrected values of $\log(A/T)$ are displayed in Fig. I-24 for the three displacement models as a function of corner frequency f_0 and t^* .

$\log(A/T)$ is a measure of m_b except for an overall gain factor. In Figs. I-24(a) and (b), a hatched line of m_b vs pulse period T for U.S. explosions is shown. This line was obtained by P. D. Marshall²⁰ from EDR reports. The curves of $\log(A/T)$ of the Sharpe model were arbitrarily scaled so that the explosion line falls in the region between the curves for $t^* = 0.50$ and 1.0 , a reasonable assumption based on direct estimates of Q based on near-field and teleseismic

measurements.^{21,22} This scaling was then applied to the theoretical curves in Figs. I-24(b) and (c).

It is apparent that the range of periods and slope of the explosion line matches the theoretical curves for the Sharpe and Brune models reasonably well. However, the Rat Island earthquake data clearly cannot fit either ω -square model. In Fig. I-24(c), the Savage model seems to fit the earthquake well in view of the simplicity of the model. Both the wide range of periods and the slope of m_b vs T are adequately described by the Savage model. Thus, we can clearly reject the ω -square models for these events using only available bulletin data and without spectral analysis.

C. W. Frasier
R. G. North

I. CONTRIBUTION OF WWSSN STATIONS TO THE PDE BULLETIN

Three separate months of the USGS "Summary of Data Entered into ERL Hypocenter System and its Usage" reports were studied to evaluate the contributions from the WWSSN stations used to produce the Preliminary Determination of Epicenters (PDE) Bulletin. The three monthly reports were for January 1972, December 1972, and for July 1973. These three months appear to be average reporting periods to the USGS, so the percentages computed of the total events and the mean day/event of reporting times could be used as the approximate percentage and mean day/event time for any given period. Each station of the WWSSN network was evaluated as a function of the station's contribution to the total number of events, its contribution to m_b computations, and to the reporting lag time of the station. The WWSSN stations used for this evaluation are listed in the USGS "Seismograph Station Abbreviations and Coordinates," March 1974, deleting stations which are listed as closed.

A total of 115 WWSSN stations was evaluated. Thirty of these stations did not report to the USGS in any of the above-mentioned months. The percentage of the stations' time picks associated to the 1548 events reported for these three months varied from 43 percent for station KBL to 0.3 percent for station AKU, with the network station average association being 10.6 percent. Although many of the WWSSN stations reported amplitudes and periods for a large percentage of their reported time picks, their contributions to all events were small as the number of associated time picks was small. These percentages varied from 13.3 percent for station COL to 0.0 percent for 28 stations. The average WWSSN station contributed amplitude and period measurements for 3.7 percent of the 1548 events. The mean time in days for the stations of the WWSSN network to report events varied from 2.2 days for station WES to 61.5 days for station QUE. The mean delay for the entire WWSSN network was 19.3 days. Of the 85 stations which reported during these three months, 25 stations reported within 1 week, 34 stations within 2 weeks, 44 stations within 3 weeks, 64 stations within 4 weeks, and with the remaining 21 stations reporting more than 4 weeks after the event.

The USGS requires that at least 5 station arrival times be associated as an event to be reported by the PDE report. A total of 321 events with body wave magnitude 4.6 m_b was reported by the USGS for 1972. These events were evaluated to determine the number which would have met the 5 associated station arrival time requirements if only the WWSSN stations were reported. Two hundred fourteen events met this requirement with a loss of 107 events being reported. This does not mean that the associations of WWSSN time picks for these 214 events would meet the travel-time residual restrictions imposed by the USGS to be used in the hypocenter computation. One hundred fifty-three events of the 321 events would have met the required number of stations

associated as well as the restrictions on arrival time residuals. Fifty-two percent of the 321 events of magnitude 4.6 m_b would not have been reported by only the WWSSN network of stations. Body wave magnitudes for 107 of these 153 events would have been calculated from the amplitudes and periods reported by WWSSN stations, but 40 of these m_b values would have been single-station values.

A further investigation to determine the best 50 stations using existing methods of reporting to the USGS is being conducted. The determining factors for these stations will be the number of times the arrival times of these stations are associated and used to compute the hypocenter, the number of amplitude and period measurements reported, and the smallest mean day/event reporting time.

R. Needham

REFERENCES

1. Seismic Discrimination SATS, Lincoln Laboratory, M.I.T. (31 December 1975), DDC AD-A025777.
2. P. Molnar and J. Oliver, "Lateral Variation of Attenuation in the Upper Mantle and Discontinuities in the Lithosphere," *J. Geophys. Res.* 74, 2648-2682 (1969).
3. S. C. Solomon and M. N. Toksöz, "Lateral Variation of Attenuation of P and S Waves Beneath the United States," *Bull. Seismol. Soc. Am.* 60, 819-838 (1970).
4. S. C. Solomon, "Seismic Wave Attenuation and Partial Melting in the Upper Mantle of North America," *J. Geophys. Res.* 77, 1483-1502 (1972).
5. H. Acharya, "Magnitude-Frequency Relation and Deep-Focus Earthquakes," *Bull. Seismol. Soc. Am.* 61, 1345-1350 (1971).
6. Seismic Discrimination SATS, Lincoln Laboratory, M.I.T. (30 June 1975), DDC AD-A014793/4.
7. P. D. Marshall, private communication (1976).
8. J. F. Evernden, "Bias in Estimates of m_b at Small Magnitudes," preprint (1976).
9. J. F. Evernden and D. M. Clark, "Study of Teleseismic P: Part II, Amplitude Data," *Phys. Earth Planet. Inter.* 4, 24-31 (1970).
10. E. Herrin and J. Taggart, "Regional Variations in P Travel Times," *Bull. Seismol. Soc. Am.* 58, 1325-1337 (1968).
11. J. A. Sharpe, "The Production of Elastic Waves by Explosion Pressures, I. Theory and Empirical Field Observations," *Geophysics* 7, 144-154 (1942).
12. J. N. Brune, "Tectonic Stress and the Spectra of Seismic Shear Waves from Earthquakes," *J. Geophys. Res.* 75, 4997-5009 (1970).
13. J. N. Brune, "Correction," *J. Geophys. Res.* 76, 5002 (1971).
14. J. C. Savage, "Relation of Corner Frequency to Fault Dimensions," *J. Geophys. Res.* 77, 3788-3795 (1972).
15. E. W. Carpenter, "Absorption of Elastic Waves - An Operator for a Constant Q Mechanism," United Kingdom Atomic Energy Authority, AWRE Report No. 0-43/66 (October 1966).
16. J. R. Filson and C. W. Frasier, "Multisite Estimation of Explosive Source Parameters," *J. Geophys. Res.* 77, No. 11, 2045-2061 (1972).

17. M. Wyss, T. C. Hanks, and R. C. Liebermann, "Comparison of P-wave Spectra of Underground Explosions and Earthquakes," J. Geophys. Res. 76, 2716-2729 (1971).
18. M. E. O'Neill and J. H. Healy, "Determination of Source Parameters of Small Earthquakes from P-wave Rise Time," Bull. Seismol. Soc. Am. 63, 599-614 (1973).
19. "Operation of Two Observatories," Technical Report No. 66-54, Final Report, Project VT/5054, 1 May 1965 through 30 April 1966, Teledyne Geotech Corporation, Alexandria, Virginia (1 June 1966).
20. P. D. Marshall, personal communication from unpublished report (1976).
21. L. D. Trembly and J. W. Berg, "Seismic Source Characteristics from Explosion Generated P Waves," Bull. Seismol. Soc. Am. 58, 1833-1848 (1968).
22. C. W. Frasier and J. R. Filson, "A Direct Measurement of Earth's Short Period Attenuation along a Teleseismic Ray Path," J. Geophys. Res. 77, 3782-3787 (1972).

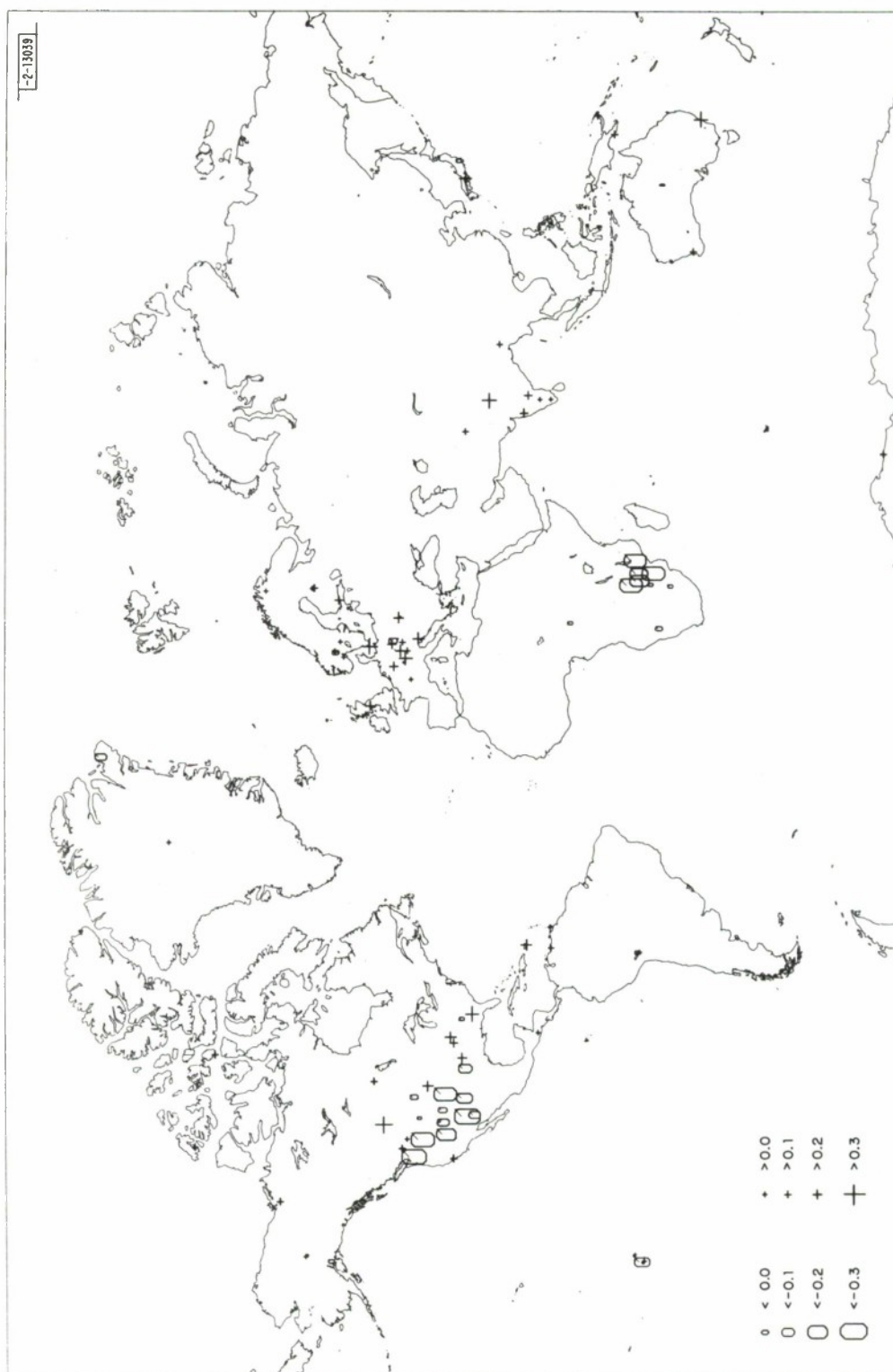


Fig. I-1. Mean biases measured for the 102 stations used in this study. Circles enlarge as biases become more negative, crosses enlarge as they become more positive.

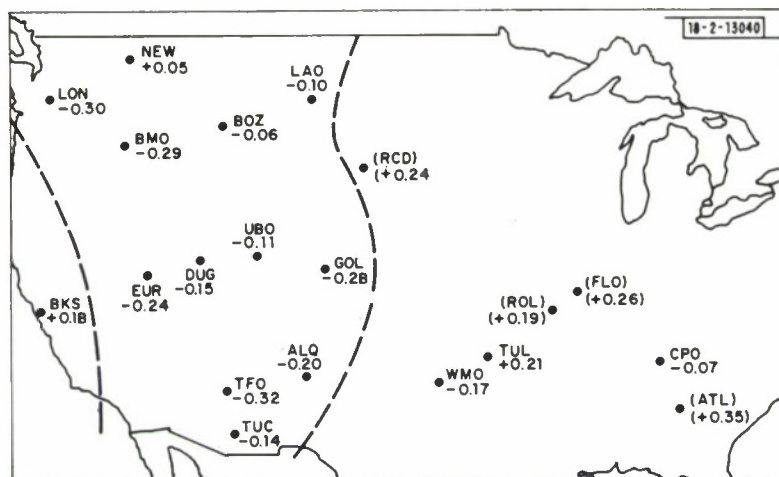


Fig. I-2. Mean biases measured for stations in the continental U.S. Values in parentheses are from Table I-2, all others from Table I-1. Dashed lines separate regions of negative and positive bias.

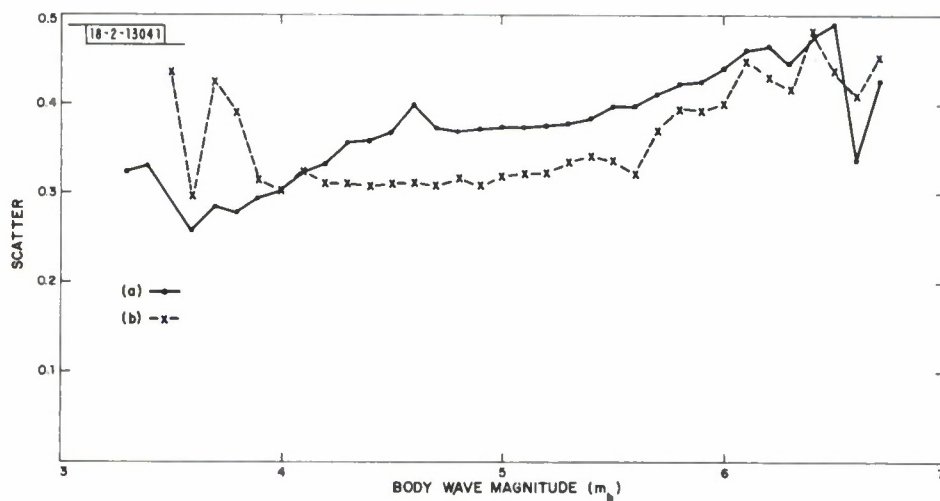


Fig. I-3. Scatter, as defined in the text, of station m_b values relative to average m_b , as a function of average m_b ; (a) and (b) show scatter prior to and after application of biases as station corrections.

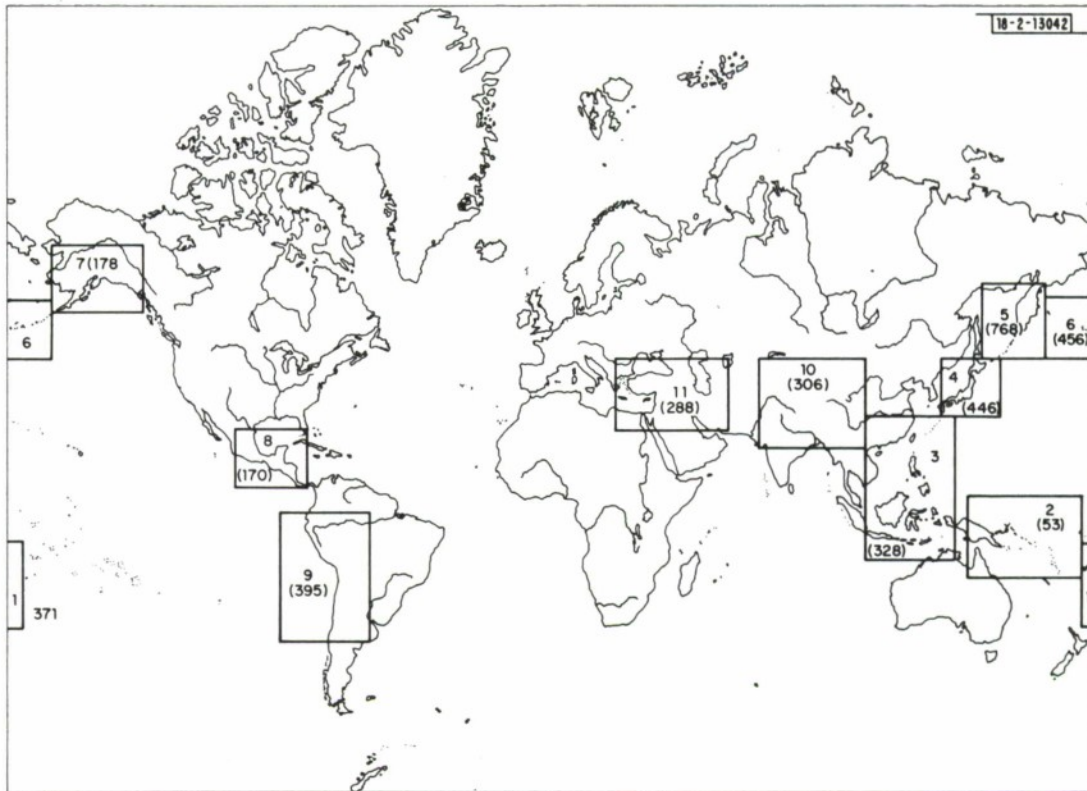


Fig. I-4. Seismic source regions for which station biases have been calculated. The number of events in each reported by 15 or more of the 72 stations in Table I-1 is shown in parentheses.

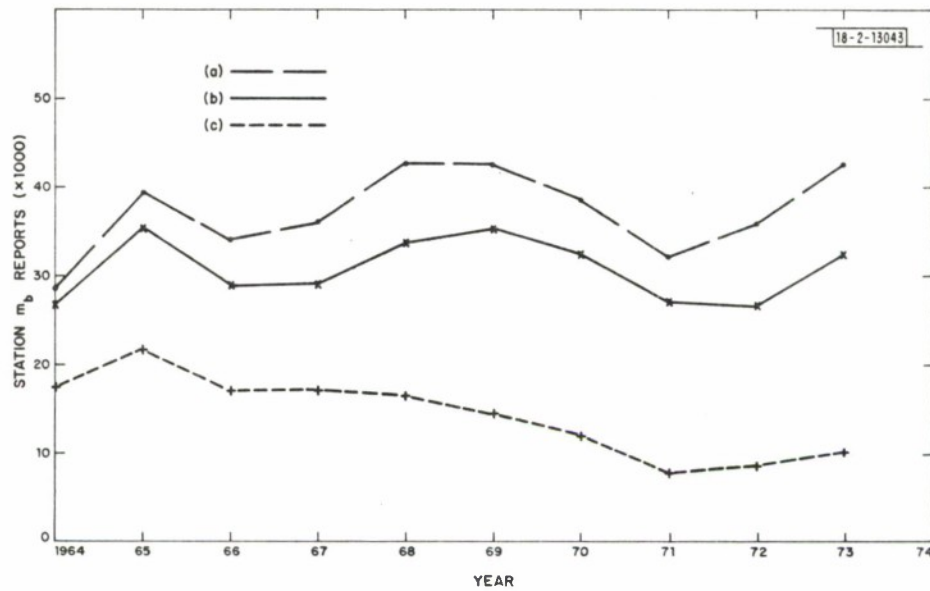


Fig. I-5. Annual numbers of station m_b reports as given in the ISC Bulletin for (a) all stations, (b) 72-station network, and (c) 13 stations in western U.S.

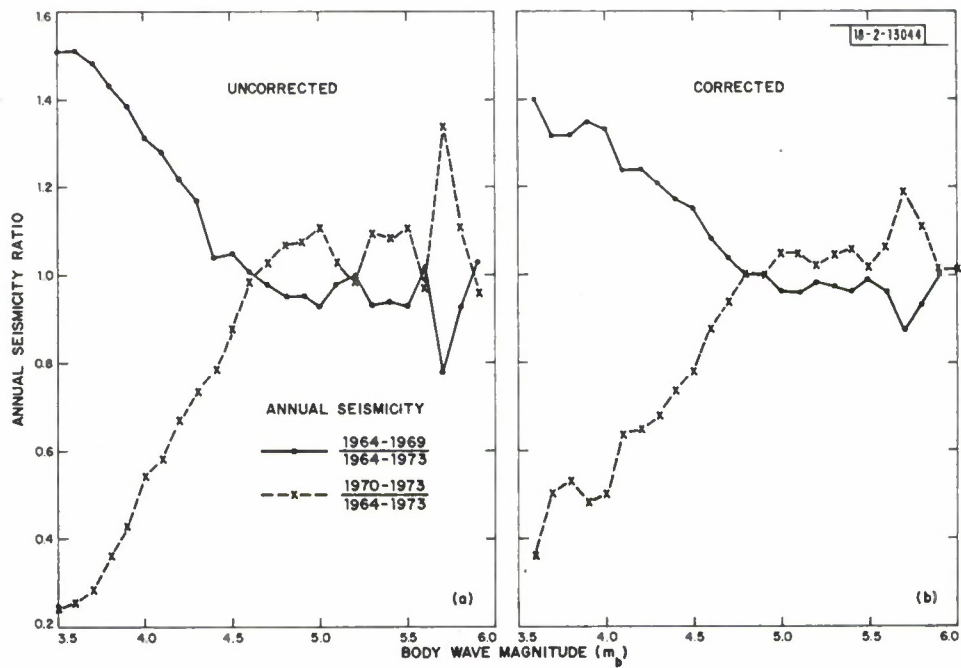


Fig. I-6. Ratios of annual seismicity as a function of average m_b for 1964-1969, 1970-1973 to that for 1964-1973, prior to and after application of biases as station corrections.

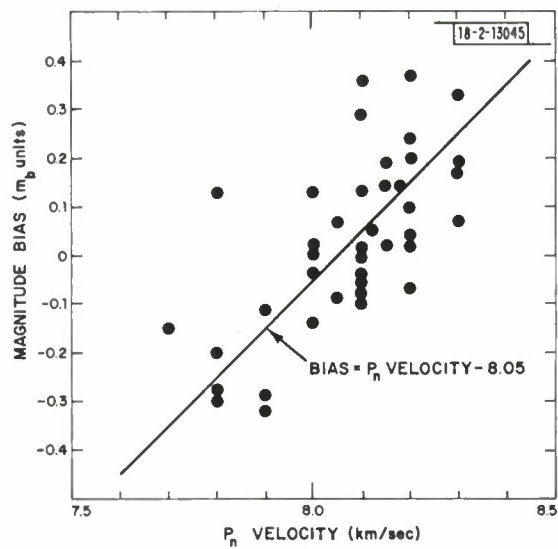


Fig. I-7. Plot of station magnitude bias (from Table I-1) against local P_n velocity (from Marshall⁷).

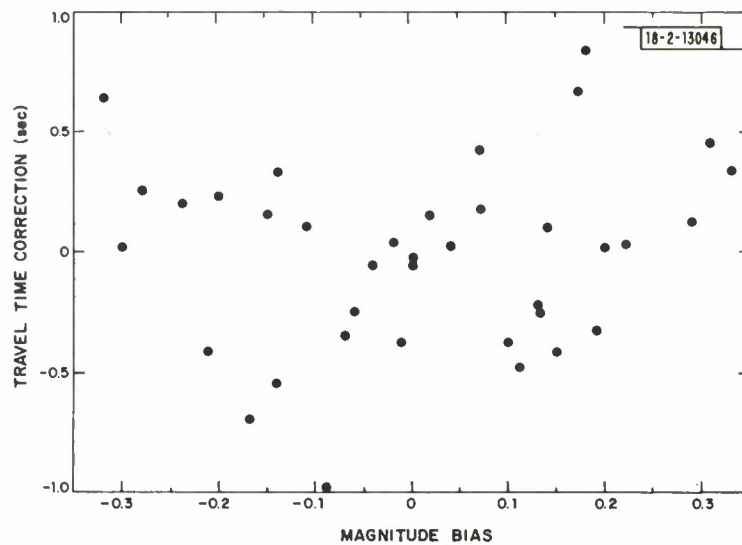


Fig. I-8. Plot of station magnitude bias (from Table I-1) against travel time correction (from Herrin and Taggart⁴).

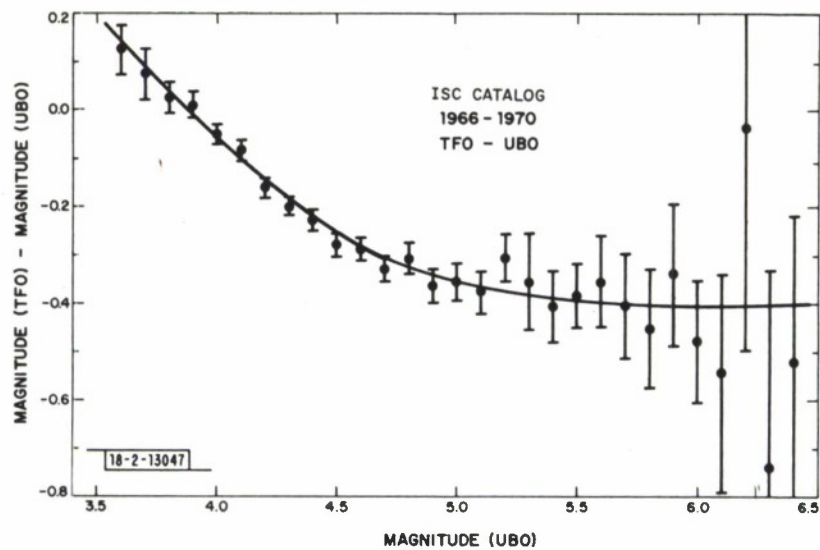


Fig.I-9. Magnitude differences for stations TFO and UBO, using UBO as a reference. Each point is the average of many observations. The vertical bars show 95-percent confidence bounds on the mean values. The solid line is a theoretical relation derived from parameters explained in the text.

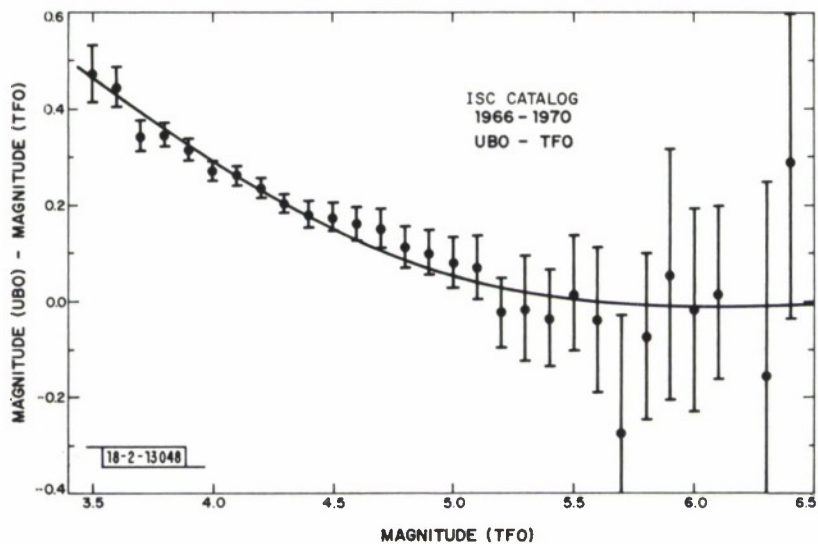


Fig.I-10. Magnitude differences for stations UBO and TFO, using TFO as a reference (compare Fig.I-9).

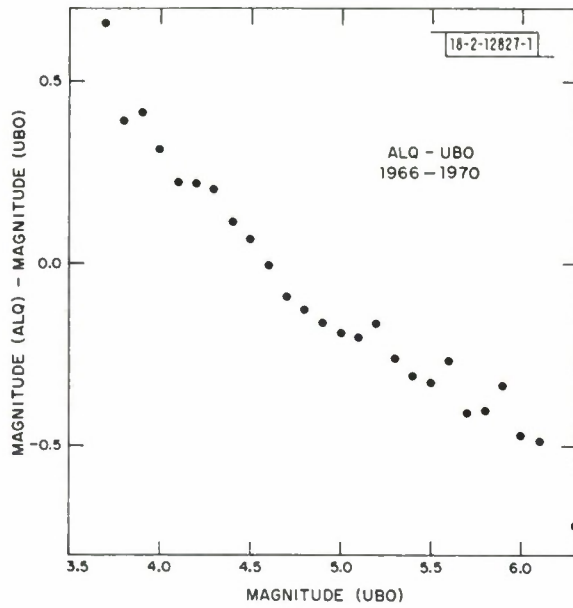


Fig. I-11. Magnitude differences for stations ALQ and UBO, using UBO as a reference.

Fig. I-12. Magnitude differences for stations EUR and UBO, using UBO as a reference.

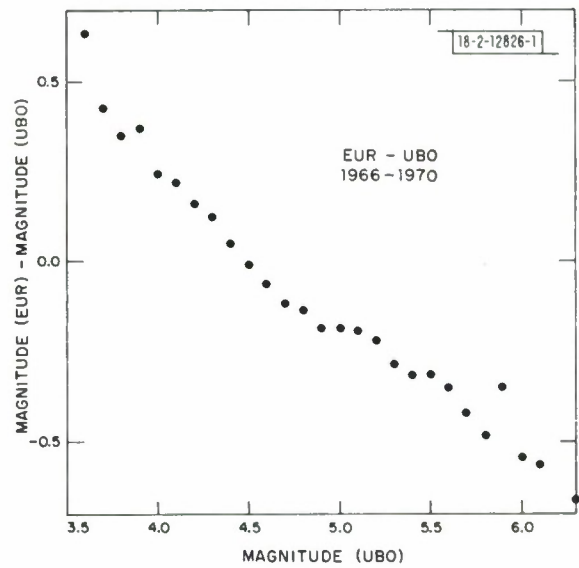


Fig.I-13. Corrected values of $\log(A/T)$ due to a Sharpe source model as a function of corner frequency and attenuation parameter t^* . The dashed line is the source amplitude at 1 Hz.

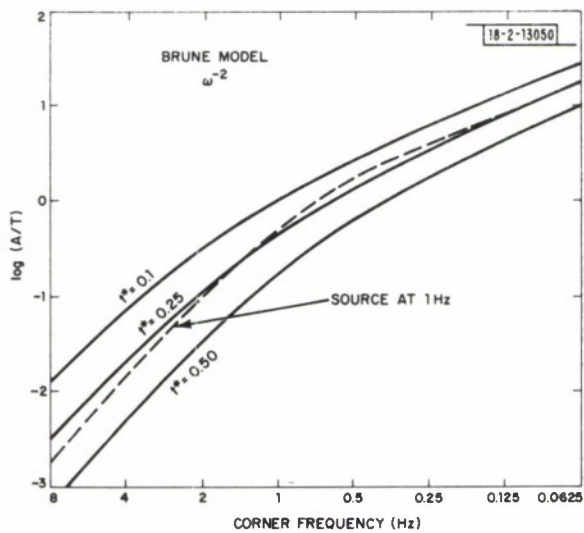
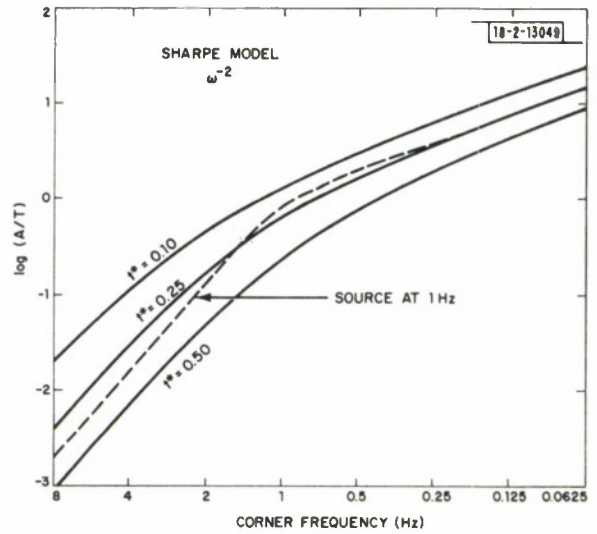


Fig.I-14. Corrected values of $\log(A/T)$ due to a Brune source model as a function of corner frequency and attenuation parameter t^* . The dashed line is the source amplitude at 1 Hz.

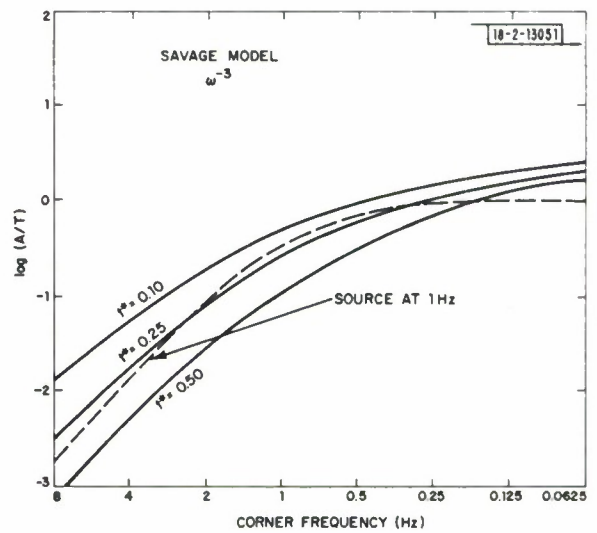


Fig.I-15. Corrected values of $\log(A/T)$ due to a Savage source model as a function of corner frequency and attenuation parameter t^* . The dashed line is the source amplitude at 1 Hz.

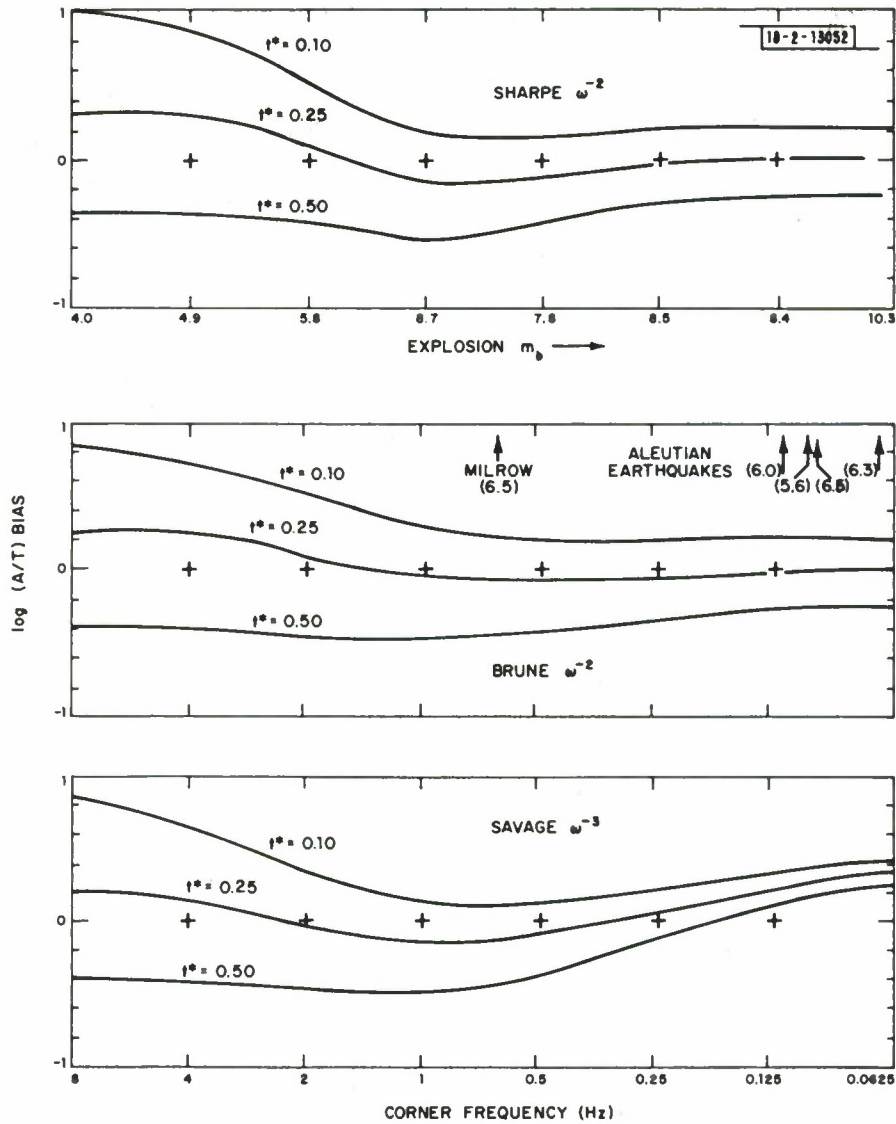


Fig. I-16. Bias of measured $\log(A/T)$ about true source amplitude at 1 Hz for Sharpe, Brune, and Savage source models. Each curve shows the bias for a given t^* as a function of corner frequency. The m_b explosion scale was obtained from Sharpe's model using empirical relations for magnitude m_b , yield Y , and cavity radius a . Numbers in parentheses are magnitudes for an explosion and four Aleutian earthquakes (see text).

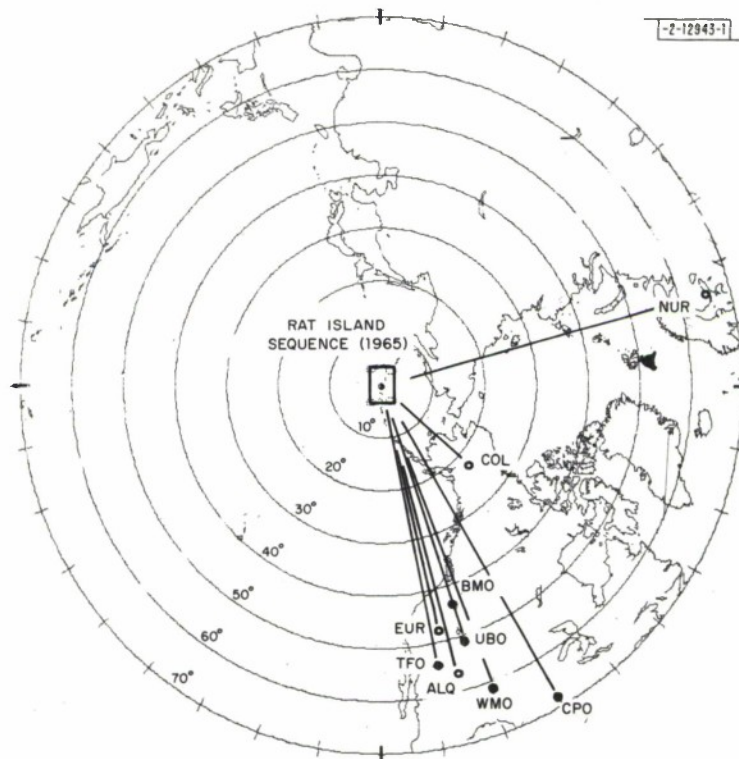


Fig.I-17. Map centered on the area of the Rat Island sequence of earthquakes (1965). Open circles are WWSSN stations and solid circles are Vela arrays.

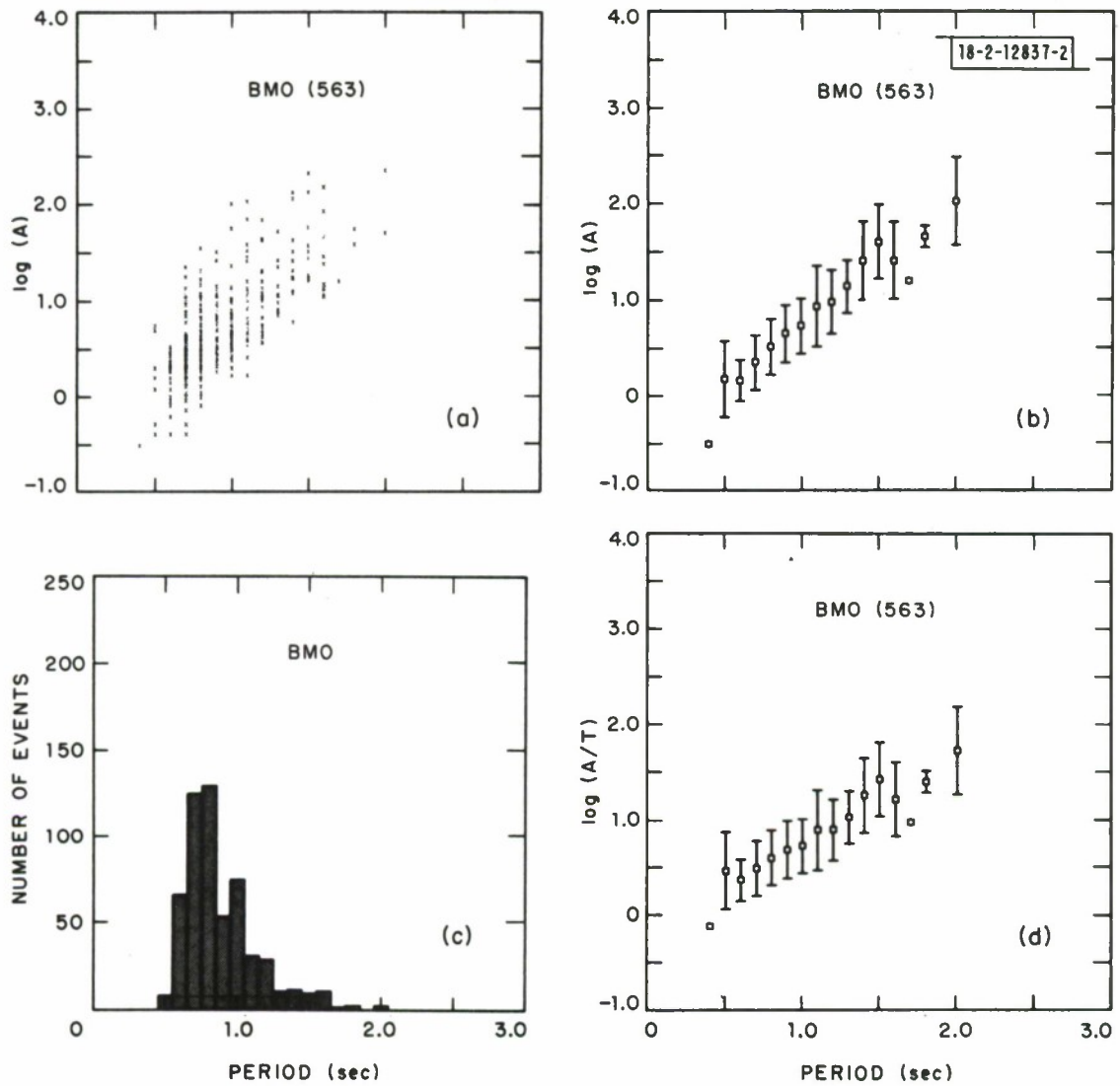


Fig. I-18. Amplitudes and periods of the 563 Rat Island earthquakes recorded at BMO: (a) shows the scatter of $\log(A)$ with T ; (b) displays the mean and standard deviation of $\log(A)$ at each T ; (c) is a histogram of reported periods; and (d) is a plot of mean and standard deviation of $\log(A/T)$ as a function of T .

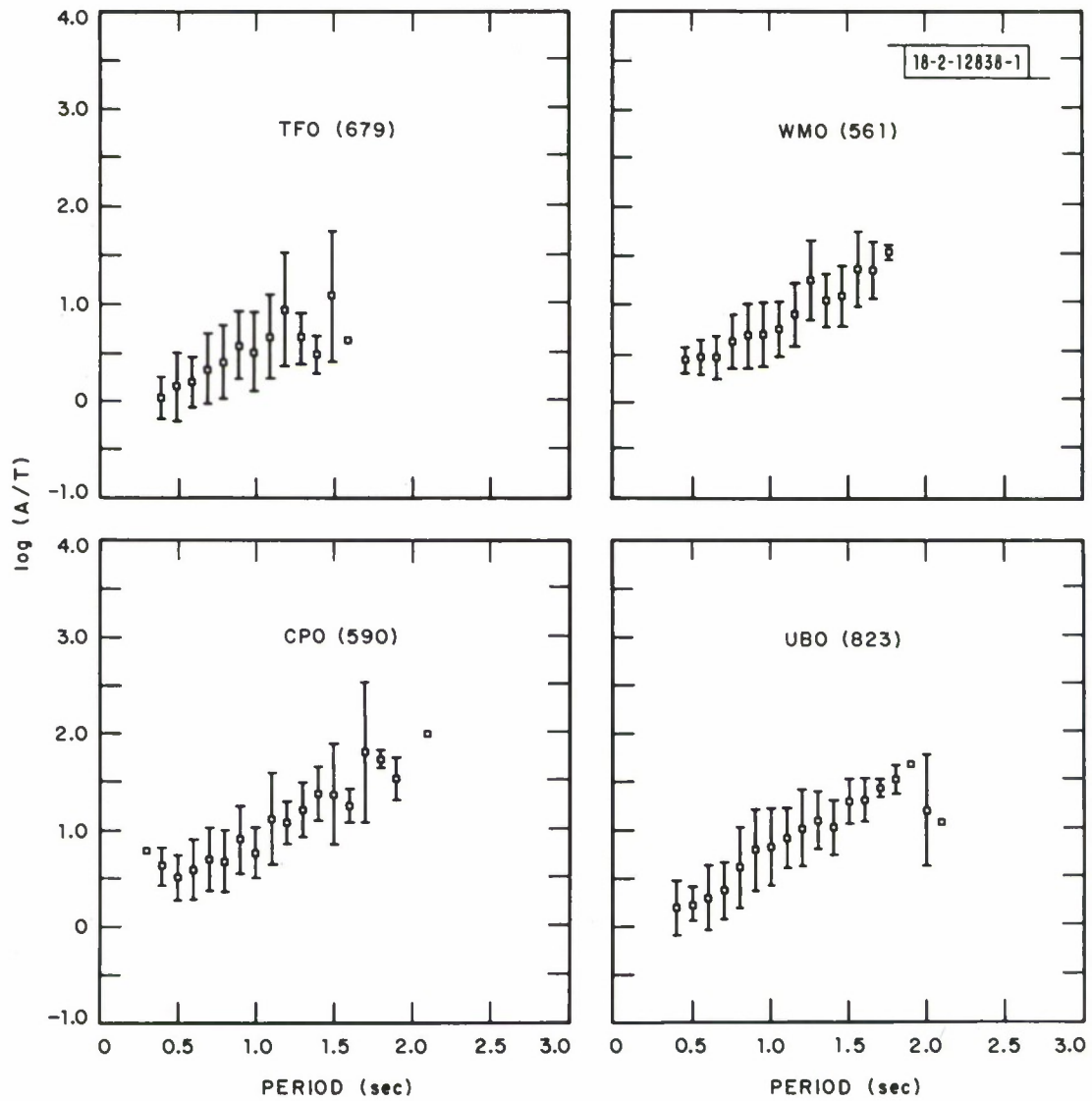


Fig. I-19. Mean and standard deviation of $\log(A/T)$ as a function of T for Rat Island earthquakes recorded for four Vela arrays.

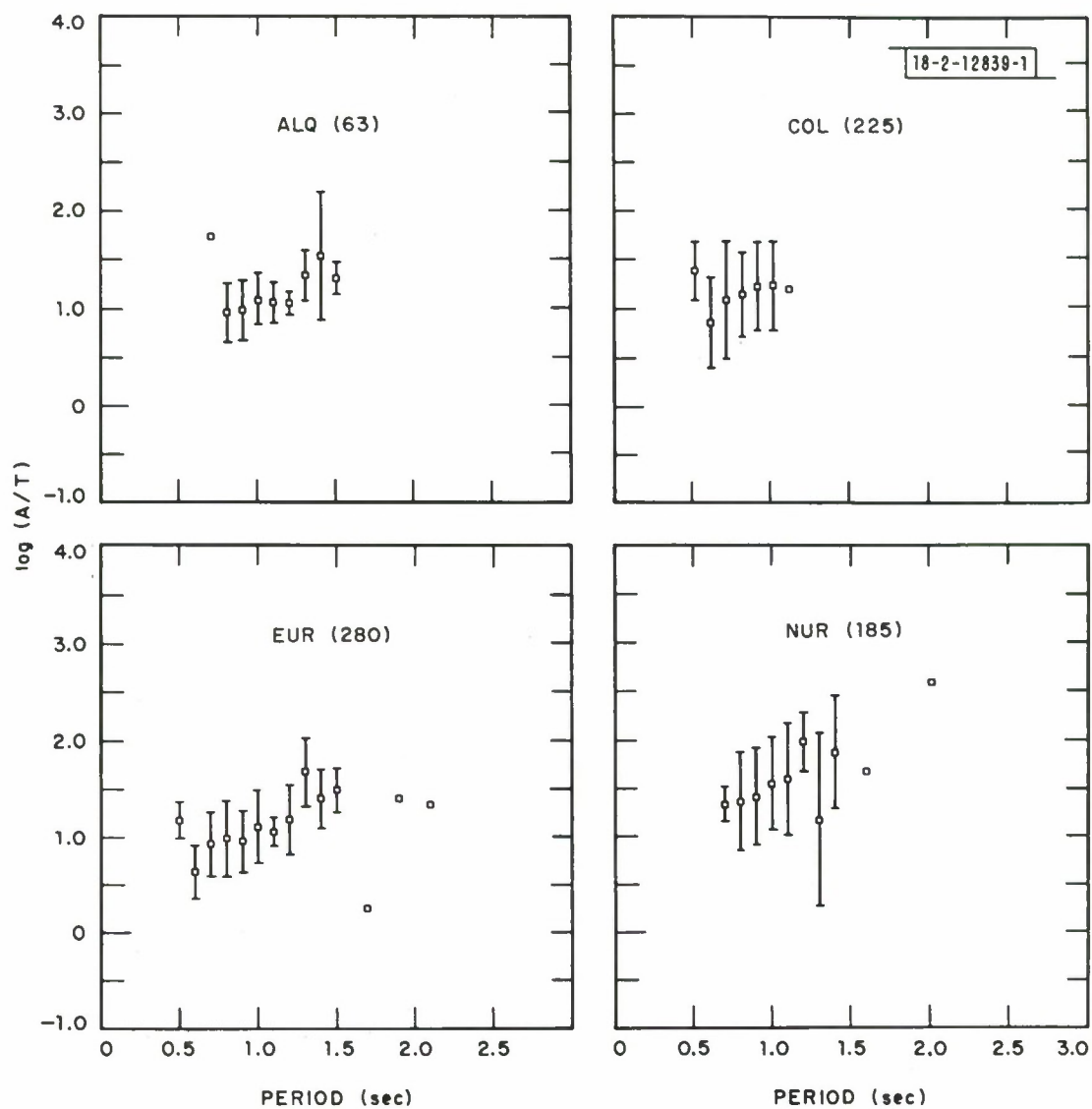


Fig. I-20. Mean and standard deviations of $\log(A/T)$ as a function of T for Rat Island earthquakes recorded at four WWSSN stations.

Fig. I-21. Amplitude spectra $U(f)$ for three source functions plotted as a function of scaled frequency f/f_0 , where f_0 is the corner frequency.

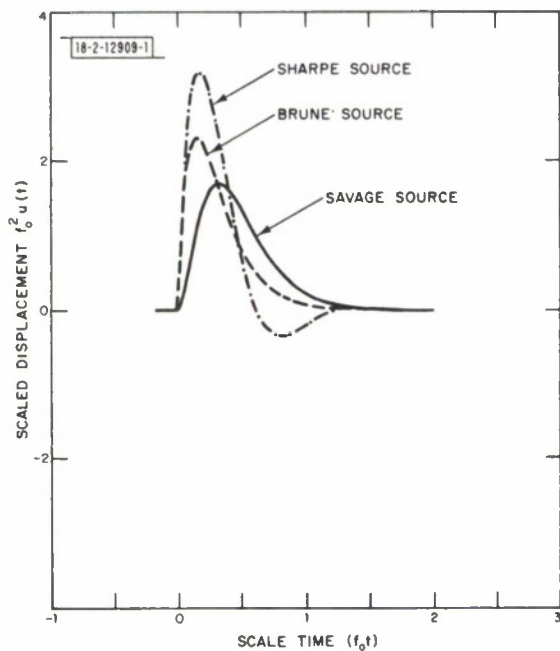
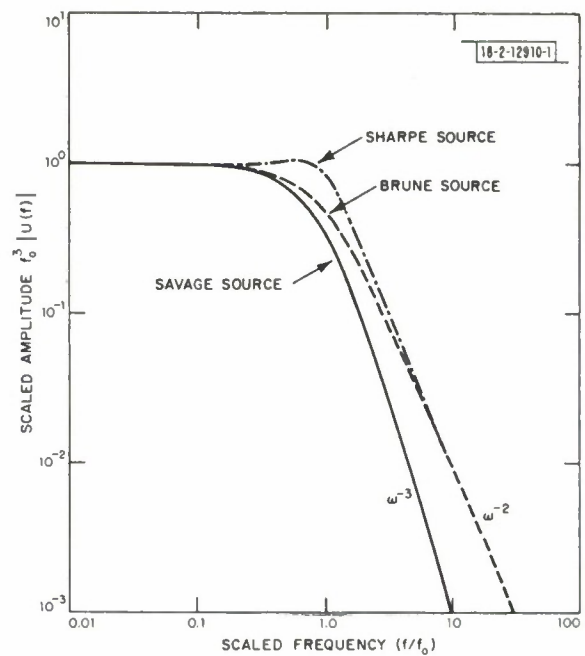


Fig. I-22. Far-field displacement $u(t)$ for three source functions plotted as a function of scaled time t/f_0 .

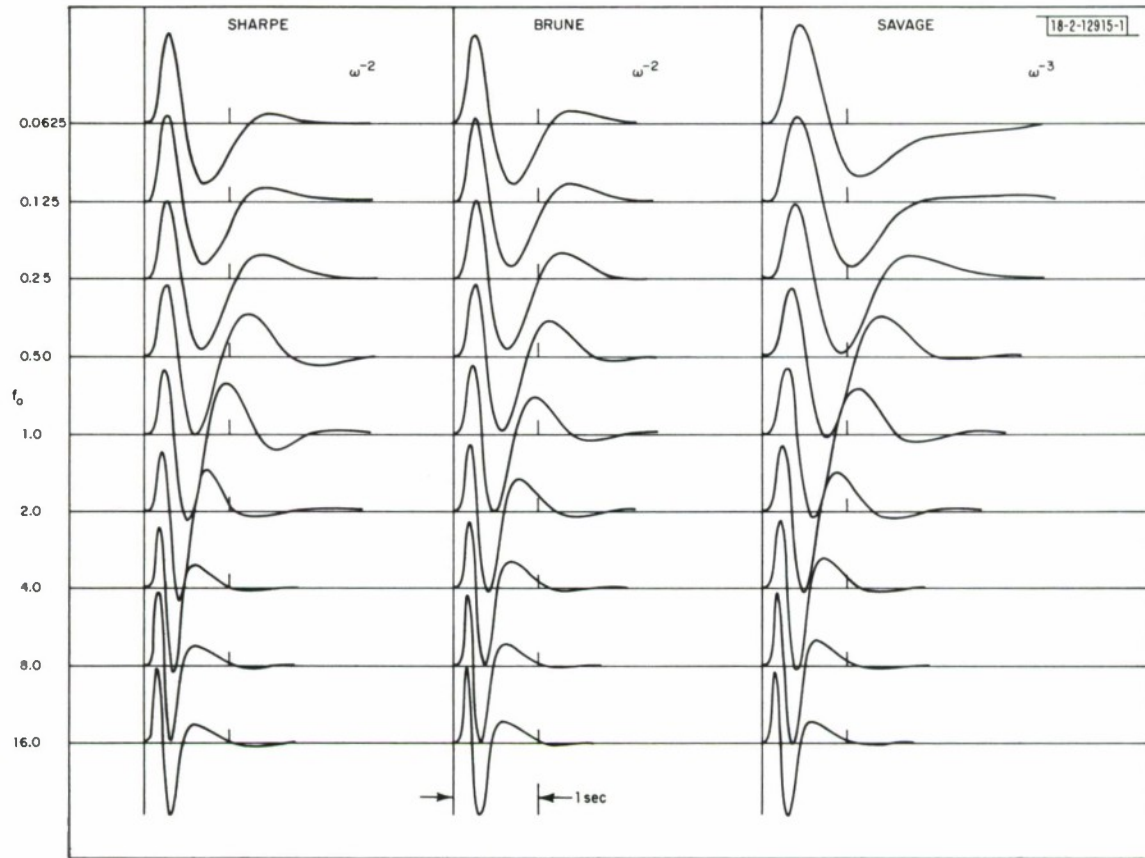


Fig.I-23. Synthetic seismograms obtained by convolving three source functions with the Vela short-period seismometer system. Corner frequencies range from $f_0 = 0.0625$ to 16 Hz. Earth attenuation for a $t^* = 0.10$ is included. Amplitudes of all seismograms are equalized for comparison.

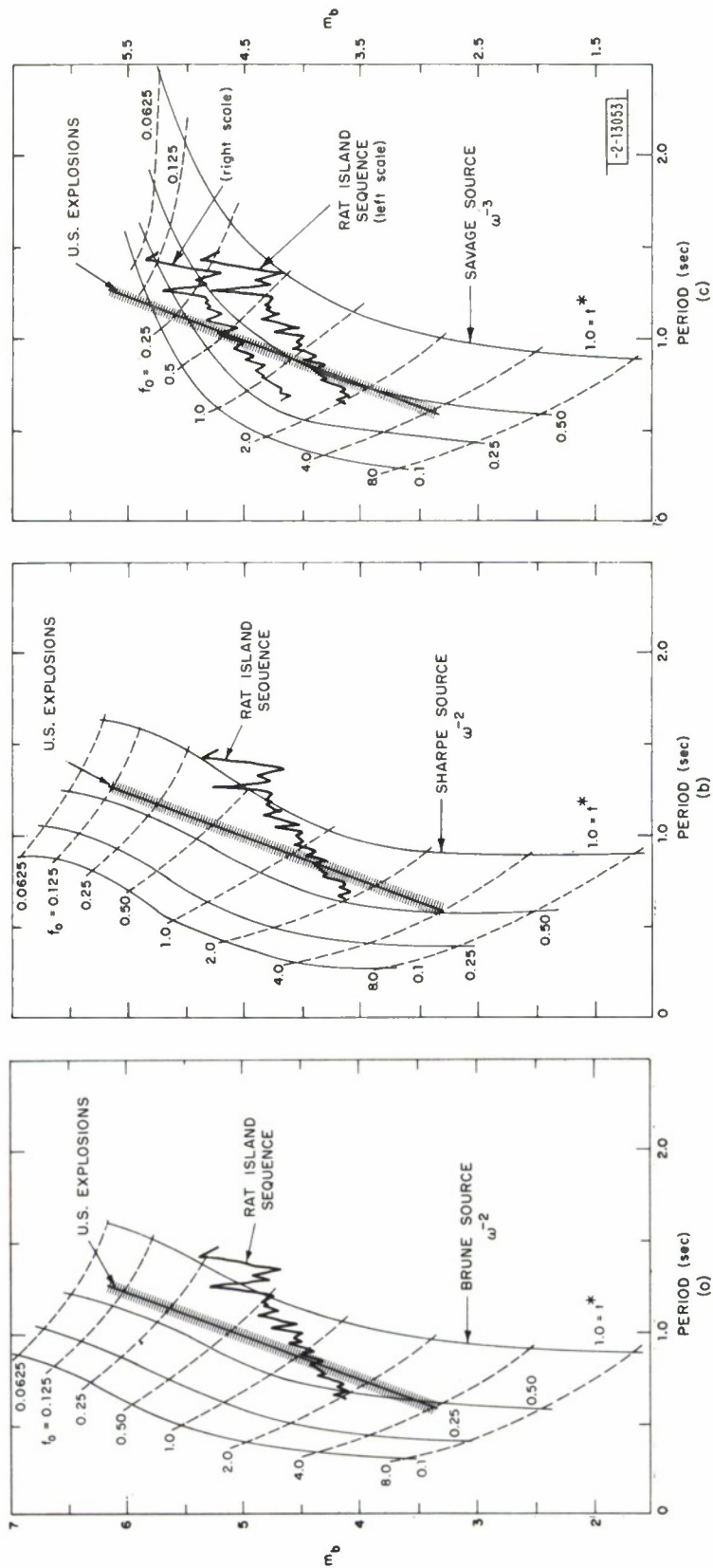


Fig. 1-24. Predicted m_b vs period T for three source functions. Solid lines are m_b vs T for four attenuation parameters, $t^* = 0.10, 0.25, 0.50$, and 1.0 . Dashed lines indicate corner frequencies f_0 in each source function. Hatched line shows trend of m_b vs T of U.S. nuclear explosions obtained from the EDR (P. D. Marshall 20). Jagged line is average m_b vs average T for Rat Island earthquakes recorded simultaneously at all five Vela stations.

II. SURFACE WAVE STUDIES

A. THE EFFECTS OF LATERAL HETEROGENEITY IN THE OCEANIC LITHOSPHERE UPON SURFACE WAVE PROPAGATION

Evidence from studies of Rayleigh wave dispersion indicates a systematic increase in phase velocity as the age of the sea floor increases away from the oceanic ridge.^{1,2} The greatest change takes place in the first few million years, due to the rapid cooling and solidification of the upper part of the lithosphere. Anisotropy of propagation such that the Rayleigh waves travel faster in the direction of spreading is also required by the data¹ - this feature is not incorporated here since it considerably complicates the differential equations to be solved in the ray tracing method used.

At a period of 33 sec, the values obtained for Rayleigh wave phase velocities are [for age zones 0 to 5 million years (MY), 5 to 10 MY, 10 to 20 MY, and 20 MY+] 3.794, 3.852, 3.920, and 3.966 km/sec, respectively.¹ These values of phase velocity may be assigned to the mean ages of the zones (2.5, 7.5, 15, and 25 MY), where the last is a reasonable value since very little of the ocean floor studied¹ is older than 38 MY. These data points are shown in Fig. II-1. A very good fit to these four points can be obtained by a second-order polynomial of the form

$$V(A) = aA^2 + bA + c \dots \quad (\text{II-1})$$

where V is the phase velocity at age A (MY). Least-squares values of (a, b, c) are $(-0.239 \times 10^{-3}, 0.1425 \times 10^{-1}, 3.759)$. The value of phase velocity at the ridge axis ($A = 0$) is given by a ; the value of 3.759 is close to that (3.769) given by an earth model for the mid-oceanic ridge.²

The ray tracing problem is considerably simplified in this context if we consider a spherical earth composed of two rigid hemispherical plates such that their axis of relative rotation coincides with the polar axis of the earth. The age of formation A of any part of the two plates at longitude φ is then given by

$$A = \frac{|\varphi - \varphi_0|}{|\underline{\omega}|} \quad (\text{II-2})$$

where φ_0 is the longitude of the ridge axis and $\underline{\omega}$ is the relative angular rotation vector of the two plates. The age A and, thus, phase velocity $V(A)$ are then conveniently independent of latitude Θ . The relative spreading rate at the ridge axis is a maximum at the equator and zero at the poles, expressed in cm/yr; it is, however, constant if expressed in degrees of longitude φ /yr.

The partial differential equations for surface wave ray tracing³ involve Θ , φ , azimuth ξ , and phase velocity V and its spatial derivatives $\partial V/\partial \Theta$ and $\partial V/\partial \varphi$. For the present case, taking $\varphi_0 = 0$ and $\underline{\omega}$ such that the spreading rate is 1° of longitude/MY (corresponding to 11.1 cm/yr at the equator) we have, from Eq. (II-1)

$$\begin{aligned} V(\varphi) &= a\varphi^2 + b\varphi + c \\ \frac{\partial V}{\partial \varphi} &= 2a\varphi + b \\ \frac{\partial V}{\partial \Theta} &= 0 \end{aligned} \quad (\text{II-3})$$

making the ray tracing equations particularly simple.

The results of ray tracing in the velocity model given by the above equations are shown in Fig. II-2. The rays extend to a distance of 25° , corresponding to the limit of validity of Eq. (II-1). The rays leave the source at 5° intervals in azimuth and can be seen to be slightly bent toward the ridge axis (running North-South). The velocity derivative $\partial V / \partial \varphi$ is fairly small and continuous; the azimuth derivation of the ray (azimuth at distance of 25° minus starting azimuth) is a maximum (2.66°) at a starting azimuth of 8° .

We may consider the error introduced in determination of phase velocity as a function of age (and thus longitude) by decomposition of the path into great circle segments as opposed to the "true" path given by ray tracing. The apparent phase velocity at a point P is given by

$$V_{rp} = \int_0^P \frac{d\ell}{T(\ell)} \quad \text{for the ray path} \quad (\text{ray}) \quad (\text{II-4})$$

and

$$V_{GC} = \int_0^P \frac{d\ell}{T(\ell)} \quad \text{for the great circle path} \quad (\text{great circle}) \quad (\text{II-5})$$

where $T(\ell)$ is the phase delay introduced by a particular segment ℓ of the path. The difference between V_{rp} and V_{GC} at points P at distances of 25° is a maximum at the azimuth of maximum azimuthal deviation of 8° ; it does not, however, exceed 0.0015 km/sec and, thus, the neglect of horizontal refraction cannot be the cause of the apparent anisotropy observed.¹ Since the azimuthal deviations are small, the effect of the velocity structure upon surface wave amplitudes is also small. Figure II-3 shows the variation of spectral amplitudes with azimuth due to non-geometrical spreading. The amplitudes can be seen to be enhanced in the direction of the ridge axis. This implies that measurements of Q beneath the ridge axis from surface wave amplitudes may be biased upward by the effect of nongeometrical spreading.

R. G. North

B. SYNTHETIC RAYLEIGH WAVE SEISMOGRAMS FOR THE FALLON EARTHQUAKE

The event pair consisting of the Fallon earthquake (20 July 1962) and the Shoal explosion (26 October 1963) is notable because it is one of the few occurrences of both an earthquake and an explosion in the same location with good azimuthal station coverage. Consequently, it has a long history of inquiry into its surface wave features.⁴⁻⁸ This present study of the Fallon earthquake is an attempt to derive its source parameters by making use of a seismic moment tensor representation of the Rayleigh wave point source equations.⁹ Ultimately, we hope to obtain these parameters by systematic inversion. The results presented here are those from solutions of the forward problem (calculate the radiation from a given moment tensor) and were found by an ad hoc trial and error procedure.

As implemented, the theory assumes that the location of the event and its depth are known. Then, using a plane layered structure, synthetic Rayleigh waves are calculated for the case of a step function of applied moment. Other source time functions can easily be accommodated by the appropriate convolution operation. The seismometer instrument response is also included to allow direct comparison with the data. The synthetic seismograms presented here consist of the fundamental and first higher Rayleigh wave modes.

Both Fallon and Shoal occurred in the Fairview-Dixie Valley region of Nevada and were recorded by Long-Range Seismic Measurements (LRSM) stations principally situated in the Basin and Range province. Exceptions are the California stations. Figure II-4 shows the event locations and the 11 LRSM stations which were used. The earth structure is composed of a crust appropriate to Fallon (the Fallon-Ruth model of Toksöz *et al.*⁷) underlain by a typical continental mantle with both a P- and S-wave low velocity zone. Phase and group velocity dispersion curves as a function of horizontal wavenumber (necessary to implement the theory) are shown in Fig. II-5. The data plotted to the same amplitude and time scales are shown in Fig. II-6.

Synthetic seismograms from the best double-couple fault plane solution are shown in Fig. II-7. They indicate a double-couple seismic moment near 1.1×10^{23} dyn-cm. In fitting the observed data, it was noticed that the solution was most sensitive to the slip angle λ and least sensitive to the strike angle Θ . Solutions with only a few degrees different slip were unacceptable, but the solution persisted over 15° to 20° of strike variation.

TABLE II-1 FALLON FAULT PLANE SOLUTIONS				
	Strike (°E of N)	Dip (deg down)	Slip (deg up HW block)	Depth (km)
Present study	5	75	190	10
Lombert <i>et al.</i> (1971)	10	82	16	15
Toksöz <i>et al.</i> (1965)	355	76	230	20

A comparison with two other Fallon fault plane solutions is presented in Table II-1. The present study solution, in addition to being the best fit to the data in the vicinity of its fault angles, comes closest to matching that of Lambert *et al.*⁸ The principal differences are in the direction of slip (NNE for Lambert *et al.*, SSW for the present study) and the amount of dip slip motion. The Fallon data given here favor left lateral movement with relatively little dip slip motion. The solution by Toksöz *et al.*⁷ is based on only three stations and bears little resemblance to the present solution.

There is some tectonic information available from the literature. Van Nostrand and Helterbran⁶ show surface fault breaks from a 1954 earthquake in the Dixie Valley region of Nevada. The Fallon location, computed using arrival times corrected for Shoal, is to the east of one of the 1954 fault breaks. A crude measurement from the map indicates a strike of 20° and a dip of 79° which tends to support both the Lambert *et al.* and present fault plane solutions.

The results from trying to add compensated linear vector dipole (CLVD) and monopole (MP) moment sources to the double-couple (DC) solution are shown in Fig. II-8. The most obvious effect of this is in the reduced amplitude of the WINV seismogram. The addition of either of these source mechanisms to the DC solution tends to hurt the fit. Thus, the actual source mechanism of Fallon must have appreciably less than 10 percent CLVD or MP components.

These results, though preliminary in that they represent a subjective solution criterion, indicate that the Fallon earthquake was a left lateral predominantly strike slip event with its

fault plane generally aligned with known tectonic features in the source region. The double-couple seismic moment was approximately 1.1×10^{23} dyn-cm and there appeared to be less than 10 percent of this moment in either the CLVD or MP mechanism. Further work along this line should consist of automating the inversion process partly to reduce the manual labor involved and also to remove the subjective judgment factor.

D. W. McCowan

REFERENCES

1. D. W. Forsyth, "The Structural Evolution and Anisotropy of the Oceanic Upper Mantle," *Geophys. J. R. Astr. Soc.* **43**, 103-162 (1975).
2. A. R. Leeds, "Lithospheric Thickness in the Western Pacific," *Phys. Earth Planet. Inter.* **11**, 61-64 (1975).
3. B. R. Julian, "Ray Tracing in Arbitrarily Heterogeneous Media," Technical Note 1970-45, Lincoln Laboratory, M. I. T. (31 December 1970), DDC AD-720795.
4. J. N. Brune and P. W. Pomeroy, "Surface Wave Radiation Patterns for Underground Nuclear Explosions and Small-Magnitude Earthquakes," *J. Geophys. Res.* **68**, 5005-5028 (1963).
5. "Fallon Earthquake," Technical Report No. 63-122 (Rev. 1964), Teledyne Geotech Corporation, Alexandria, Virginia (1964).
6. R. Van Nostrand and W. Helterbran, "A Comparative Study of the Shoal Event," Seismic Data Laboratory Report 109, Teledyne Geotech Corporation, Alexandria, Virginia (1964).
7. M. N. Toksöz, D. G. Harkrider, and A. Ben-Menahem, "Determination of Source Parameters by Amplitude Equalization of Seismic Surface Waves," *J. Geophys. Res.* **70**, 907-922 (1965).
8. D. G. Lambert, E. A. Flinn, and C. B. Archambeau, "A Comparative Study of the Elastic Wave Radiation from Earthquakes and Underground Explosions," Seismic Data Laboratory Report 284, Teledyne Geotech Corporation, Alexandria, Virginia (1971).
9. D. W. McCowan, "Surface Wave Representation of Surface Wave Sources," *Geophys. J. R. Astr. Soc.* **44**, 595-599 (1976).

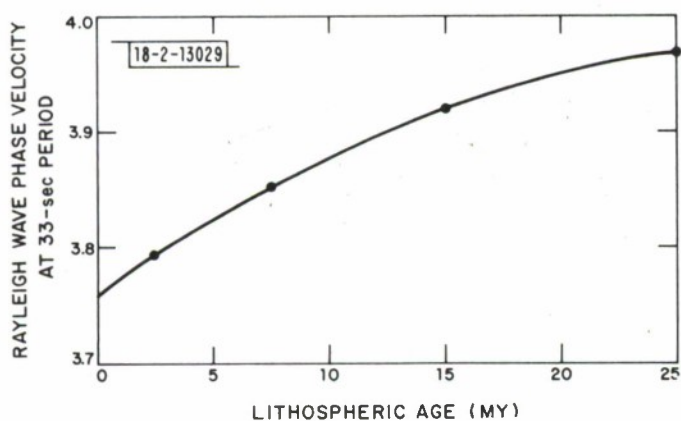


Fig. II-1. Rayleigh wave phase velocity V at 33-sec period as a function of age of formation A of oceanic lithosphere. Points are published values of Forsyth¹ for 2.5, 7.5, 15, and 25 MY; line is polynomial fit $V(A) = -0.239 \times 10^{-3}A^2 + 0.1425 \times 10^{-1}A + 3.759$.

Fig. II-2. Result of ray tracing in velocity model given by velocity function of previous figure, for spreading rate of 1° longitude/MY. Polar projection, with origin centered on ridge axis: great circle paths are straight lines from the origin; circles denote distances of 5, 10, 15, 20, and 25° .

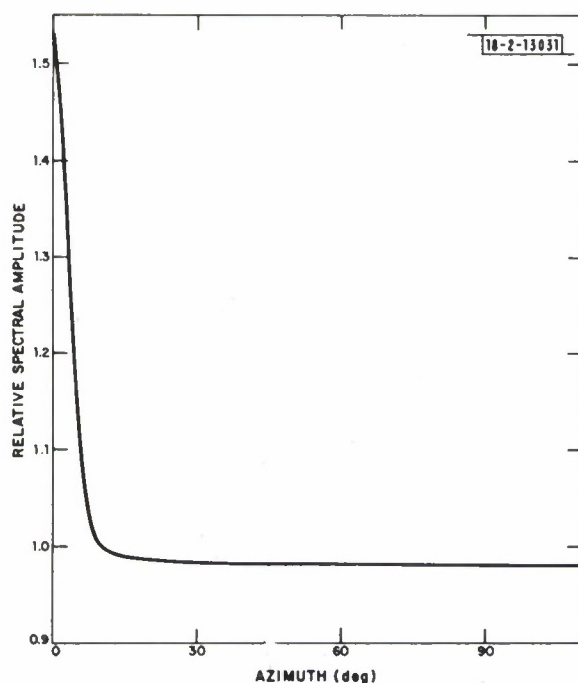
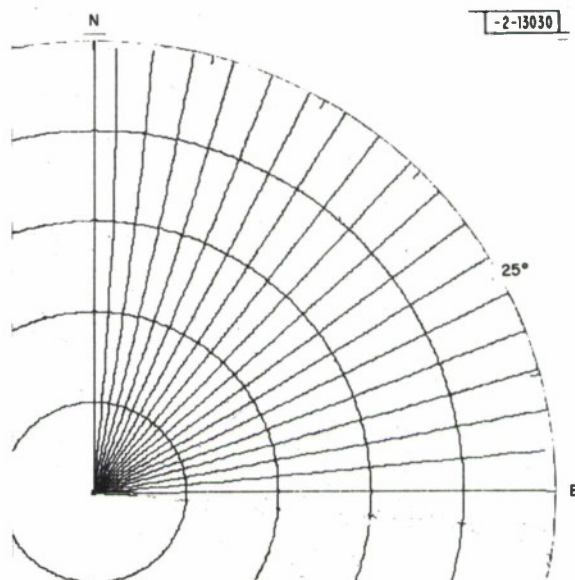


Fig. II-3. Relative spectral amplitudes of 32-sec Rayleigh waves as a function of azimuth with respect to ridge axis, derived from Fig. II-2 through amplitude $\propto (\text{ray density})^{1/2}$.

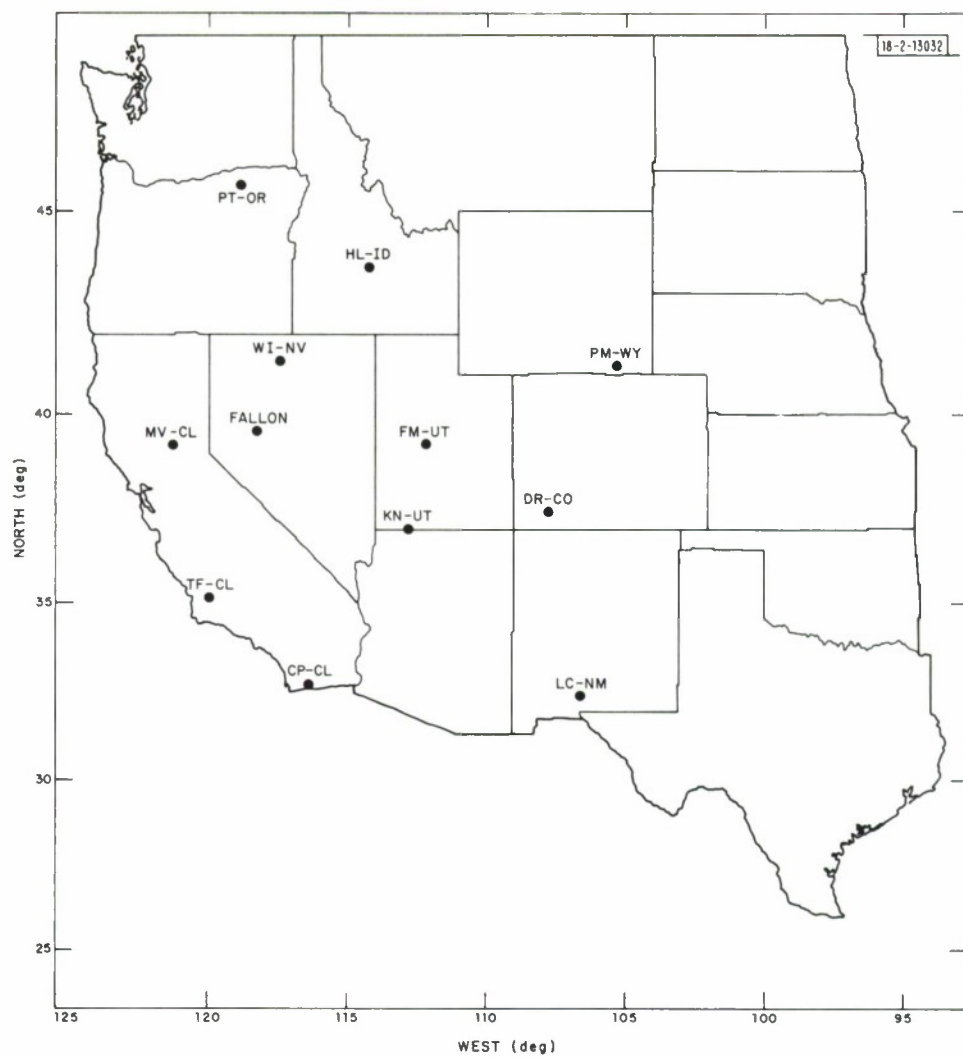


Fig. II-4. Event and recording station locations for the 20 July 1962 Fallon earthquake. Stations are temporary LRSM installations. Data set consisted of long-period vertical components.

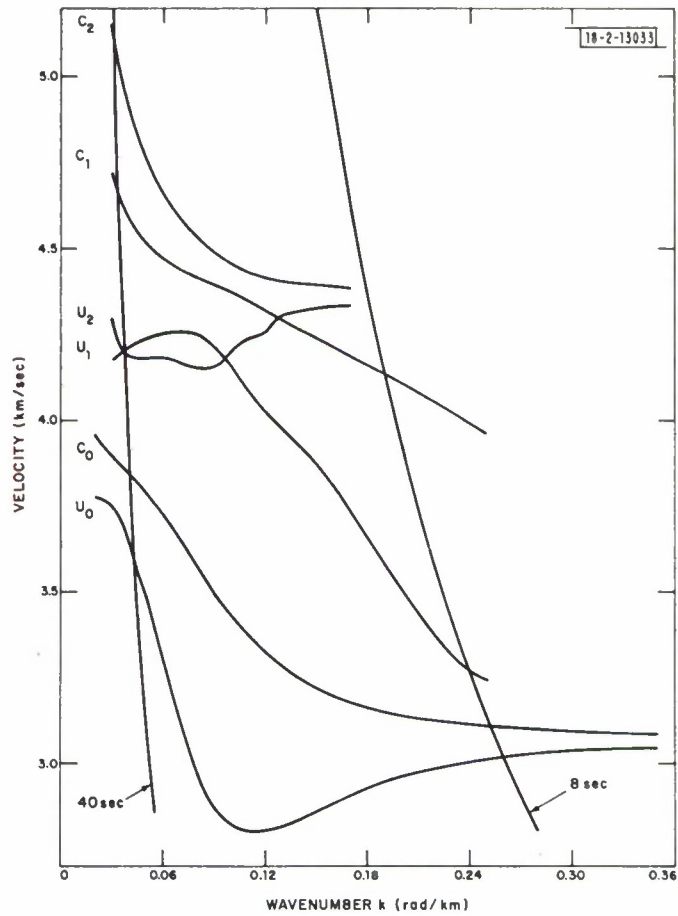


Fig. II-5. Phase and group velocity dispersion curves for 72T plane layered earth structure. First three modes shown. Lines of equal period are hyperbolas.

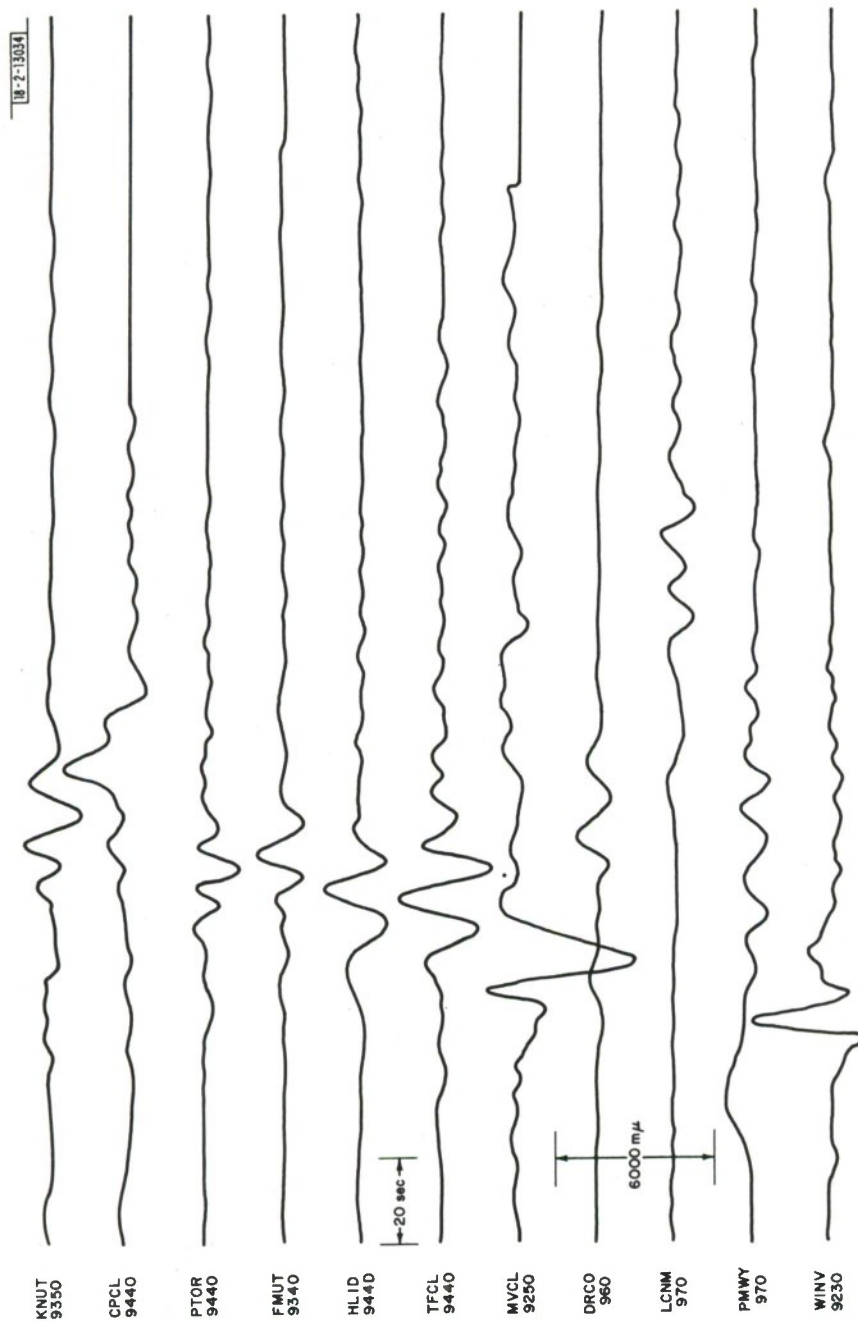


Fig. II-6. Fallon LPZ data. Station codes and start times of individual traces are given at the left.

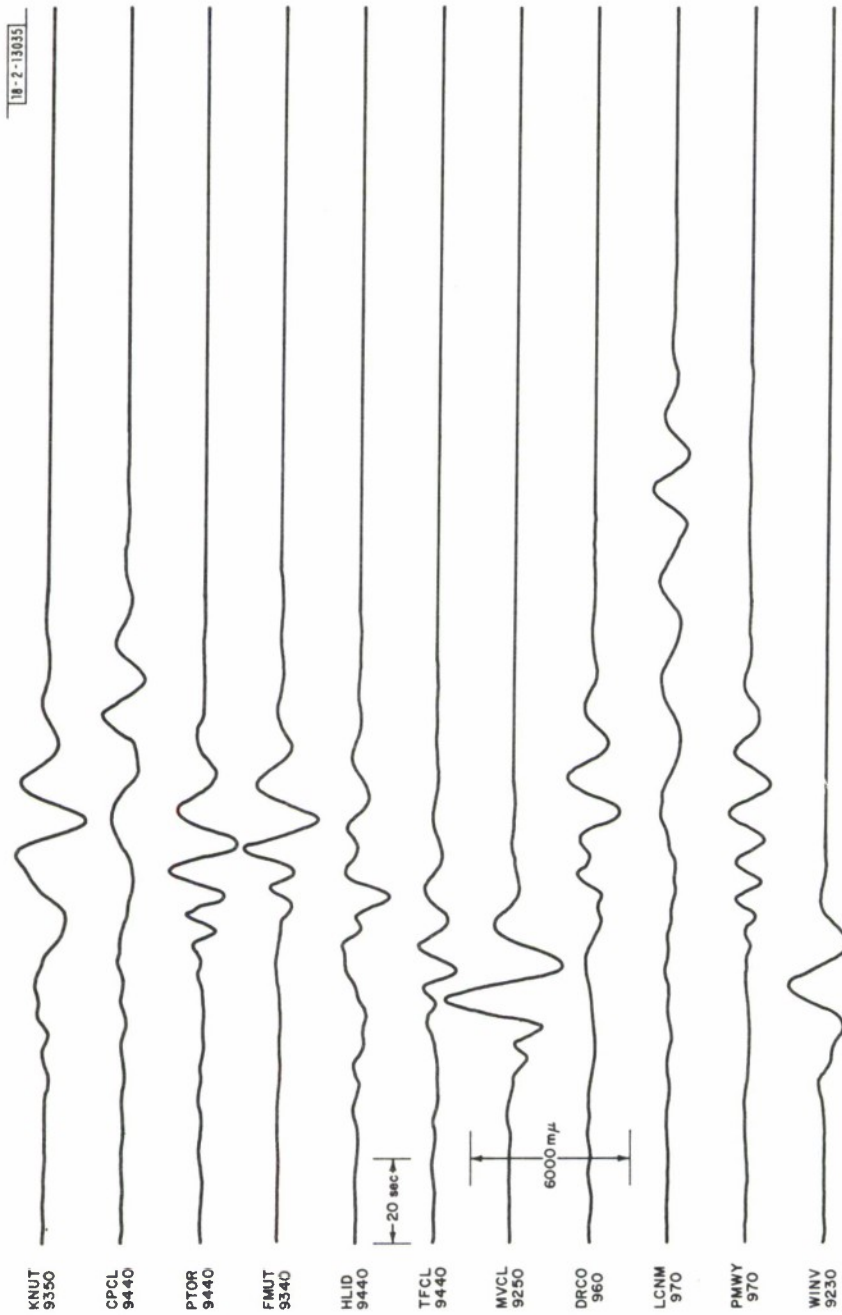


Fig. II-7. Double-couple synthetic Rayleigh wave LPZ seismograms for best fault plane solution. Plotted to same scales as data. Fault angles are strike: 5° E of N; dip: 75° down; slip: 190° up HW block. Seismic moment is 1.1×10^{23} dyn-cm. Fundamental plus first higher modes used in solution.

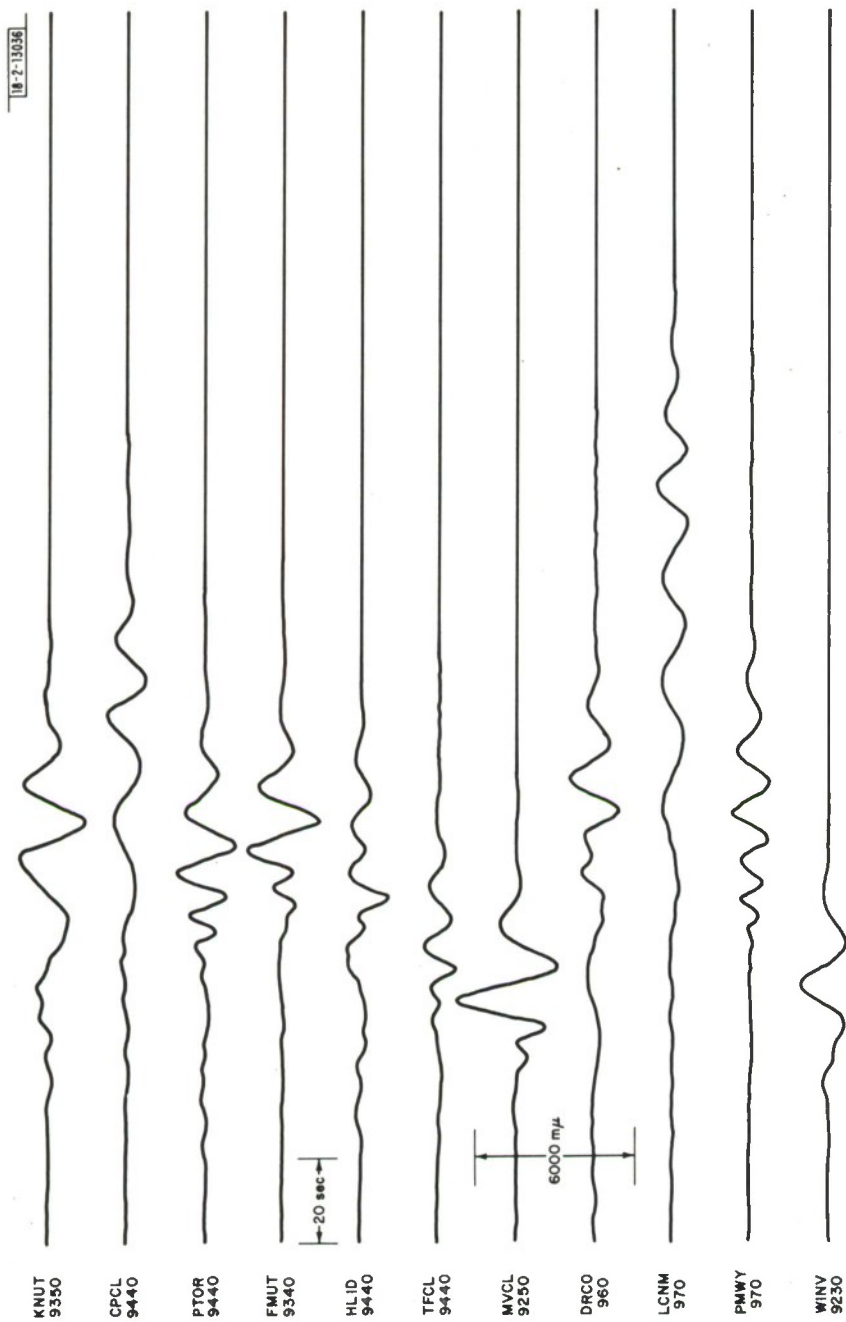


Fig. II-8. Synthetic Rayleigh wave LPZ seismograms for 16/18 DC, 1/18 CLVD, 4/18 MP source. Plotted to same scales as data. Fault angles same as best solution. Total moment is 1.1×10^{23} dyn-cm. Fundamental plus first higher modes used in solution.

III. EVASION

A. DETECTING MULTIPLE EVENTS IN NARROWBAND SEISMOGRAMS

It has been suggested^{1,2} that multiple explosions, suitably timed, can be used to simulate the seismic signature of an earthquake. Two different schemes have been derived. By firing small explosions followed by several large ones spaced over a few seconds, the complexity and $M_s:m_b$ of an earthquake can be mimicked and the first motion obscured. Alternatively, the explosions may be spread out in time such that the overall trace has the appearance of a first arrival followed by a depth phase. By suitable timing, the second arrival can even be made to appear inverted. If the delay time indicates a depth deeper than is technically feasible to emplace an explosive device, the events may be misidentified as a single earthquake. In the absence of close-in stations or sufficiently broadband signal-to-noise ratios at teleseismic distances,³ evasion by these approaches seems possible to achieve when normal discrimination techniques are employed.

If one considers that in both instances the composite seismograms consist of approximately the same signal delayed, scaled, and summed several times, the problem may be solved by determining the arrival time of each signal, and so showing the trace to be the result of multiple events rather than a single event. What we wish to do, then, is to deconvolve observed seismograms. If the source function is known, the problem reduces to the classical Wiener filtering problem. Unfortunately, signal shapes from various explosions are too different for that technique to be definitive. When neither the source nor the echo string is known, the problem is referred to as blind deconvolution.⁴ The solution to such a problem can be obtained through homomorphic deconvolution.⁵ When the source function is long compared to the size of the echo train, many segments of log spectral estimates may be averaged to yield the log spectrum of the echo train alone. For the previously mentioned evasion scenarios, the echo train and the source are comparable in size. In addition, the recording response of short-period seismometers is narrow and the log spectrum is uncontaminated by noise only over that small interval. In such a case maximum entropy cepstral analysis⁶ is an appropriate method to effect the deconvolution. The following experiments were conducted to illustrate the usefulness of using maximum entropy cepstral analysis on narrowband short-period teleseismic recordings to detect multiple arrivals that appear as a single earthquake recording.

Figure III-1(a) shows the recording of a single Nevada Test Site (NTS) explosion observed at NORSAR. Figure III-1(b) shows the complexity simulation and Fig. III-1(c) the depth phase simulation, according to the delays given by Landers.² If the seismogram in Fig. III-1(a) is denoted by $S(t)$, then the signature in Fig. III-1(b), $C(t)$ is

$$C(t) = S(t) \otimes [2\delta(t) + 5\delta(t - 1) + 9\delta(t + 2) \\ + 20\delta(t - 4) + 20\delta(t - 6) + 40\delta(t - 7) + 30\delta(t - 8) + 25\delta(t - 9)]$$

and in Fig. III-1(c), $D(t)$ is

$$D(t) = S(t) \otimes [8\delta(t) + 3\delta(t - 7) + 7\delta(t - 7.7) + 4\delta(t - 8.1) \\ + 5\delta(t - 10.5)]$$

where \otimes signifies convolution.

For $C(t)$, the record is sufficiently complex so that such a seismogram could not have been written if the source were a single explosion. Additionally, the body wave magnitude, as

conventionally measured in the first cycle, would be approximately 0.6 smaller than that due to the largest single explosion. The surface wave magnitude would be increased by approximately 0.4 over that for the largest single explosion, since the energy from all the explosions would simply sum in the 20-sec band. The combination of the decrease in m_b and increase in M_s would result in their ratio falling in the earthquake population. Taking the log spectrum of $C(t)$, correcting for instrument response, and using maximum entropy spectral analysis (in the good signal-to-noise band, 0.2 to 1.5 sec), the cepstrum of $C(t)$ shown in Fig. III-2 is obtained. The 1- and 2-sec delays clearly indicate the multiple arrivals. The depth phase in $S(t)$ is near 1 sec and, so, not resolvable.

For the depth phase simulation, $D(t)$ appears to be composed of the P, pP and sP phases for a single event whose depth is near 30 km, thus indicating that the event is an earthquake. Using that band of $D(t)$ near the apparent depth phase pP, the cepstrum shown in Fig. III-3 is obtained. The cepstrum indicates a triple event consisting of a smaller arrival preceding the major arrival by 0.7 sec and a larger arrival following it at 0.5 sec. These delays are in good agreement with the actual delays of 0.7 and 0.4 sec, respectively.

We conclude, then, that for explosions at the lower magnitudes where the usefulness of broadband recording is negated by poor signal-to-noise ratios, the occurrence of multiple events appearing as single earthquakes on teleseismic recordings can be deciphered. The techniques used in these experiments and the advent of the Seismic Research Observatory (SRO) network from which the necessary high-quality digital data can be obtained, make evasion by multiple events a difficult goal to achieve.

T. E. Landers

B. COMPARISON OF DIFFERENT PREDICTION ERROR FILTERS ON A SYNTHETIC COMPOSITE EVENT

In an attempt to determine the effectiveness of prediction error filtering in unraveling composite events, we applied different types of filters to a synthetic event made up of multiple recordings of an Eastern Kazakh presumed explosion. The presumed explosion, recorded by a LASA D2 subarray SPZ instrument, was on 24 July 1970 and is shown as the top trace in Fig. III-4.

The first part of the experiment consisted of designing a 30-point ($1\frac{1}{2}$ sec) unit span prediction error filter using 30 sec of this waveform. The algorithm was the usual least-squares Wiener-Hopf method which has been successfully used in the petroleum industry for many years. The output from this filter is shown as the bottom trace in Fig. III-4. The filter condenses the original waveform which is approximately 4 sec long to a compact waveform consisting of a small positive spike followed by a larger negative spike 0.33 sec delayed followed by a broad positive excursion 0.76 sec delayed. The total length of the condensed waveform is on the order of 1 sec.

The synthetic composite event was constructed using the amplitudes and delays formulated by Landers.² These were selected to simulate the pP phase in deep events and are given below:

<u>Phase</u>	<u>Relative Amplitude</u>	<u>Delay (sec)</u>
1	8	0.0
2	3	4.0
3	7	4.7
4	4	5.1
5	5	7.5

The synthetic composite event (first trace) and the results of using 30-point unit span prediction error filters designed on 30 sec of the original waveform (second trace) and 30 sec of the composite waveform (third trace) are shown in Fig. III-5.

As can be seen, there is very little difference in the results between designing the filters on the original vs the composite waveform. In general, however, the results will not be this similar when an actual composite event is used because the noise will not have been delayed and summed the same way the composite was constructed. By keying on the large negative spike, four of the five phases used to construct the composite can be readily identified and their time delays measured to within 5 percent. To eliminate the subjective judgment element as much as possible, these results were submitted to a trained analyst (L. Lande) for examination. He, too, was able to identify and measure four of the five phases in the filtered output. The fifth phase (the fourth in the tabulation above) can be seen in the output only when its time delay is known. Since this phase occurs with the smallest delay between itself and its predecessor (0.4 sec), we conclude that such a small delay is beyond the resolution of our method.

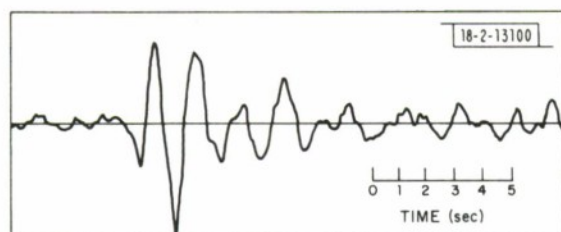
The composite event was then processed using a 30-point prediction error filter designed with the adaptive algorithm described by Griffiths *et al.*⁷ The results for three different learning rates are shown in Fig. III-6. As shown by Griffiths, small values of α (< 0.5) produce slow learning rates but good convergence in the limit and large values of α (< 1.0) produce rapid but noisy convergence to the optimum least-squares filter. Again, four out of the five phases in the composite can be identified and their time delays accurately measured. The best results, in terms of balance between noise and resolution, appear to be with $\alpha = 0.5$.

To summarize, we have shown from these results in prediction error filtering a synthetic composite event that either the least squares or adaptive algorithms is able to provide the resolution necessary to identify four out of the five individual phases in our composite. Neither method can resolve the last phase occurring at a relative delay of 0.4 sec to its predecessor. Furthermore, the results between designing a least-squares filter on the original vs the composite waveforms are quite similar.

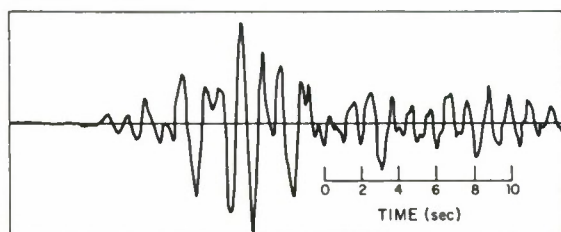
D. W. McCowan

REFERENCES

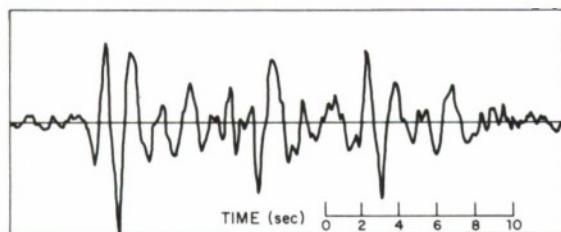
1. O. C. Kolar and N. L. Purvost, "Earthquake Simulation by Nuclear Explosions," *Nature* 253, 242-245 (1975).
2. Seismic Discrimination SATS, Lincoln Laboratory, M.I.T. (30 June 1973), DDC AD-766559/9.
3. P. D. Marshall and R. W. Hurley, "Recognizing Simulated Earthquakes," *Nature* 259, 378-380 (1976).
4. T. G. Stockham, Jr., T. M. Cannon, and R. B. Ingebretsen, "Blind Deconvolution Through Digital Signal Processing," *Proc. IEEE* 63, No. 4, 678-692 (April 1975).
5. A. V. Oppenheim, R. W. Schafer, and T. G. Stockham, Jr., "Non-linear Filtering of Multiplied and Convolved Signals," *Proc. IEEE* 56, 1264-1291 (August 1969).
6. Seismic Discrimination SATS, Lincoln Laboratory, M.I.T. (31 December 1975), DDC AD-A025777.
7. L. J. Griffiths, F. R. Smolka, and L. D. Trembly, "Adaptive Deconvolution I: Theory," paper presented to the annual meeting of the Society of Exploration Geophysicists, Denver, 15 October 1975.



(a)



(b)



(c)

Fig. III-1. Basic source function, complexity simulation, and depth phase simulation, respectively, discussed in the text: (a) $S(t)$, (b) $C(t)$, and (c) $D(t)$.

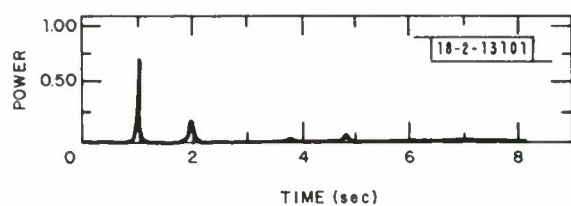


Fig. III-2. Maximum entropy cepstrum of $C(t)$.

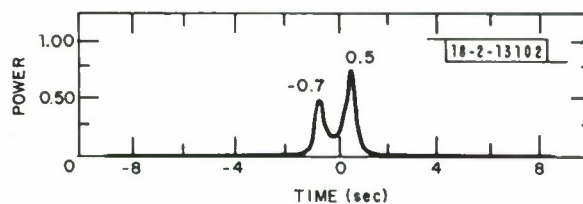


Fig. III-3. Maximum entropy cepstrum of the apparent depth phase pP portion of $D(t)$.

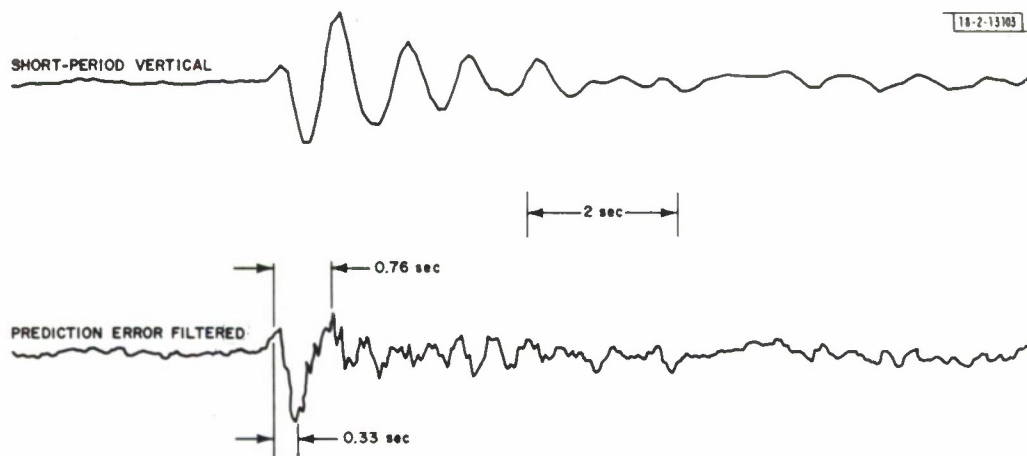


Fig. III-4. Presumed explosion from Eastern Kazakh, 24 July 1970, recorded at the D2 LASA subarray prediction error filtered with a 30-point unit span predictor designed on 30 sec of the waveform. Five percent white noise has been added to the filter design equations.

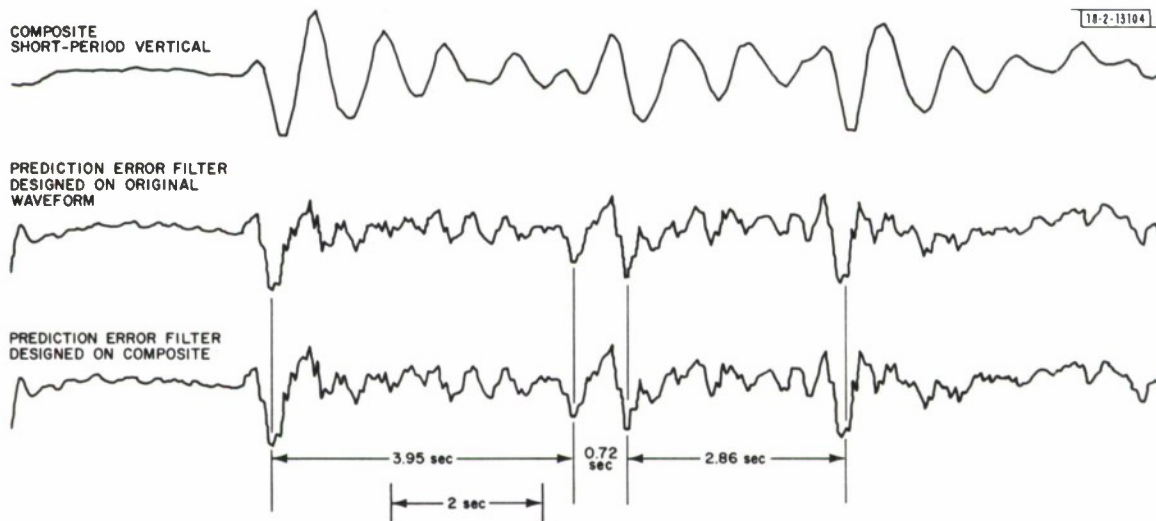


Fig. III-5. Composite event prediction error filtered with 30-point unit span predictors designed on both the original waveform and the composite event waveform. Five percent white noise has been added to the filter design equations.

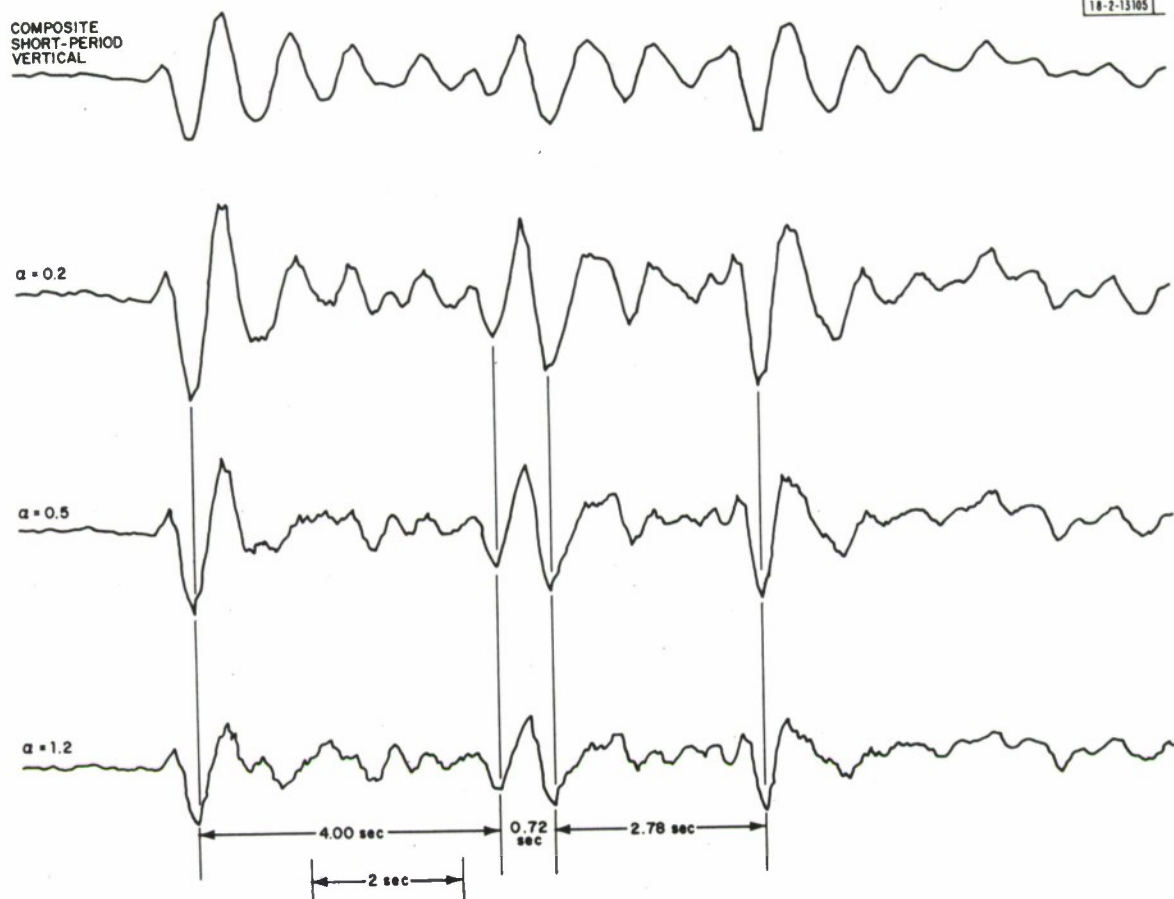


Fig. III-6. Composite event prediction error filtered with 30-point unit span adaptive predictors. Constant α controls the learning rate of the predictor.

IV. EARTH HETEROGENEITY

A. ANALYSIS OF SCATTERING FROM NOVAYA ZEMLYA EXPLOSIONS

In two previous SATS,^{1,2} we studied the codas of three component short-period data from six presumed explosions at Novaya Zemlya recorded at LASA. Using a polarization filter, it was shown that P codas are extremely sensitive to small changes in source location, implying that observed body phase components are not primarily generated by structure under LASA.

We have continued this study by investigating the arriving azimuth and emergence angle of the strongly polarized phases in the codas, in an attempt to isolate possible scattering regions in the earth. First, we pick the strongest arrivals in the coda by calculating the amplitude of the particle motion. An envelope is constructed by convolving the instantaneous amplitude of the polarized waves with a triangular window. The envelope is then fitted with a least-squares exponential decay to approximate the average coda level with time. An example of this is shown in Fig. IV-1 using event 1, which occurred on 14 October 1969 with an m_b of 6.1. All envelope peaks which are above a fraction of the exponential decay curve plus background noise are selected. The apparent dip and azimuth of the selected peaks are then calculated, and these angles are plotted on an equal area projection. Figures IV-2 to -5 are some examples of these projections for event 1, each figure representing a minute of data after the P arrival. Figure IV-6 shows an equal area projection for selected amplitude peaks in the fourth minute.

If the coda waves are generated near source region, the emergence angles should be concentrated around the initial P-wave direction. Some projections, however, show that the waves arrive from all directions, and many phases have very shallow apparent emergence angles (see Fig. IV-5). For a P-wave incident on a free surface, due to the reflected SV wave, the apparent emergence angle will be about 19° even at near zero true emergence angle for a medium obeying Poisson's relation. Thus, the peaks showing up near the rim of the equal area projection are most likely to be shear waves.

The existence of these shear waves shows that a considerable part of the coda energy is not direct P or P-to-P scattering from regions near the source. The arrival time of these shear waves in coda is not consistent with any known shear phases in travel-time tables. It is unlikely that the shear phases in Figs. IV-5 and -6 are P-to-S conversion under LASA, because there are not so many P phases preceding them in Fig. IV-4. It is thus likely they are scattered shear waves of P-to-S type from somewhere along the path.

Statistically, shear energy is important for scattering of P-waves by small inhomogeneities only when ka is not much larger than one, where k is the wavenumber and a is the correlation distance of inhomogeneities.^{3,4} If we assume the P-wave velocity is in the order of 6 km/sec, the existence of scattered S-wave about 1 Hz would mean that somewhere along the P-wave hit a region of inhomogeneity with correlation distance not much larger than 1 km.

It is thus inferred that the impulsive looking body phases in codas are scattered from inhomogeneities in a rather broad region not limited to near source or near receiver regions. The short duration and high linearity of these phases indicate that the area of these inhomogeneities is not too large.

Lacking an array with three component short-period seismometers, at the present time, we cannot locate the exact scattering region for these phases. However, we can try to match strong coda arrivals with broad scattering regions in the earth using travel-time tables. To illustrate

this we chose two phases which appear on the records of all four northern events. In Fig. IV-7, a possible P-to-P scattered phase arrives at 1 min. 17 sec after P, and in Fig. IV-8, a possible P-to-S scattered phase occurs at 2 min. 55 sec after P. Figures IV-9 and -10 show the epicentral lines of scattering regions which produce P-to-P and P-to-S arrivals at the times given above. Each line is a projection onto the earth's surface of the scattering locus at the indicated depth. It can be seen that the compatible S-scattering region is limited within 20° from LASA, while the compatible P-scattering region extends to larger distances.

M. Yang
C. W. Frasier

B. MISLOCATION PATTERNS FOR SEISMIC NETWORKS

In previous communications, attention has been drawn to the array diagram at LASA⁵ and NORSAR.⁶ Lateral heterogeneity in the deep mantle and near the source region or, alternatively, possibly small-scale inhomogeneities in the upper mantle under the arrays,⁷ have been proposed to explain certain anomalous features in the pattern of slowness vectors. Since the effect of small-scale upper-mantle inhomogeneities diminishes with increasing array aperture, it makes sense to compare conventional array data with data from an extended network of stations in the same region. Here we compare mislocations for NORSAR with those for the Scandinavian network, and mislocations for LASA with those for a network in Montana. Stations reporting to ISC have been used; the Scandinavian network also includes Finland; the Montana network has been restricted to latitudes 38° to 54° N, longitudes 98° to 115° W. Reference locations are from NOAA and arrival time data from the ISC bulletins.

Previously, array mislocations have been obtained from slowness vector anomalies.⁵ With increasing aperture of the array or network, sphericity of the earth's surface and curvature of the wave front become important. These aspects may be taken into account by computing slowness vectors from a parameterized travel time response.⁸ Alternatively, mislocations may be obtained from a first-order perturbation of the initial event latitude and longitude. Provided a suitably damped iteration scheme is used, the latter method more often converges to a stable solution. Stability criteria were: RMS time residue ≤ 1.4 sec, number of stations ≥ 5 . Typically, number of stations were 10 in Scandinavia and 7 in Montana. This method has been used and applied to three source regions (China-Russia border, Central America, Bonin Arc and surroundings), where pronounced and rapidly varying slowness anomalies at LASA and NORSAR have been reported.^{5,6} Figures IV-11 to -13 summarize the resulting mislocations, which may be compared with similar previously published figures from LASA and NORSAR data. Some points in this comparison are noted here:

- (1) China-Russia Border Region:- From the Hindu Kush to the explosion site in Eastern Kazakh, about 1700 km to the North-East and corresponding with only a few degrees in azimuth from NORSAR, there is a complete reversal of the large NORSAR mislocations.⁶ Data from the Scandinavian network (Fig. IV-11) show no significant anomalies throughout the entire region considered. A preliminary evaluation of this result places the source of the NORSAR anomaly in the near array structure.

- (2) Central America:- NORSAR mislocations vary significantly with geographic region throughout Central America. In particular, a pronounced splitting in location occurs for events in the Oaxaca district of Mexico (near 15°N, 90°W).⁶ The overall trend of mislocations in the same region obtained with the Scandinavian network (Fig. IV-12) appears to be radically different, but some important details are remarkably similar (discarding 6 unusual large arrows, which correspond to $dT/d\Delta$ near or below the core shadow boundary value). For example, there is clear evidence for lateral variation in $dT/d\Delta$ anomalies and, in particular, the splitting of NORSAR mislocations near (15°N, 90°W) also seems to be present in Fig. IV-12. This result supports the suggestion of a related anomaly in the deep mantle on the source side of the ray path.
- (3) Bonin Arc Region:- LASA mislocations of events in the Bonin Arc region contrast sharply with mislocations of neighboring events in the regions of the Ryukyu and Mariana Islands.⁵ Mislocations with the Montana network (Fig. IV-13) do not reflect a proposed source related Bonin anomaly. There are other, less conspicuous, features which need further analysis. For example, locations of Mariana Islands events with the Scandinavian network (not shown here) exhibit a splitting phenomenon similar to, though less striking than, the Central American anomaly.

In summary, most of the large array anomalies seem to be related to structure near the receiver, but some have their cause in the deep mantle or near the source region. The latter anomalies were surprisingly well resolved by the localized networks, in view of the scatter in bulletin data, variability in effective number of stations, and the lack of suitable station corrections. It is to be expected that more interesting features emerge from other source-receiver combinations.

D. J. Doornbos†
J. M. Vermeulen†

C. LARGE-SCALE HETEROGENEITIES IN THE LOWER MANTLE; CORRELATION WITH THE GRAVITY FIELD

In our previous report,¹ we described preliminary results of a three-dimensional inversion of over 700,000 P-wave travel-time residuals taken from the ISC Bulletin for the years 1964-1970.

During the last year, we have reanalyzed the data using different discretization patterns. The shell boundaries were changed with respect to those listed in Table IV-1 of Ref. 1, by subdivision of Region II into two shells: Region IIA extending from 670- to 1100-km depth and Region IIB from 1100 to 1500 km. The upper boundary of Region III was lowered from 1400- to 1500-km depth. This subdivision of Region II has significantly reduced the compensation in velocity anomalies, obvious in Figs. IV-1(a) and (b) of Ref. 1. It appears that there is an important change in the pattern of velocity anomalies at a depth of approximately 1000 km. With

† Vening Meinesz Laboratory for Geophysics and Geochemistry, University of Utrecht, The Netherlands.

the horizontal boundaries located as in Ref. 1, we have now 150 unknown parameters δv ; we shall identify the result of this inversion as Case I.

In order to test the stability of the solution with respect to a change in location of the boundaries, we rotate the meridional boundaries by 30° ; the result of this inversion is identified as Case II (we do not present the full numerical details here; the complete report⁹ is now in the process of publication).

From the beginning, we have intended to represent lateral variations of velocity in terms of the spherical harmonic expansion; the discretization approach has been adopted only for reasons of computational efficiency.

In the process of inversion, we have determined velocity perturbations δv_{ijk} , with standard errors σ_{ijk} where i is the shell index, and j and k are the indices of latitudinal and longitudinal zones, respectively. If all the δv should have equal weight, the simplest way of determining coefficients of the spherical harmonic expansion is to evaluate integrals:

$$\frac{A_{ilm}}{B_{ilm}} = \int_{\Omega} d\Omega \delta v_i(\Theta, \ell) P_{\ell}^m(\cos \Theta) \frac{\cos m\varphi}{\sin m\varphi} \quad (IV-1)$$

We call the set of coefficients obtained in this way the T solution. It is also possible to obtain coefficients A and B by the least-squares solution of an overdetermined system of observational equations:

$$\sum_{\ell=0}^L \sum_{m=0}^{\ell} A_{ilm} \overline{[P_{\ell}^m(\cos \Theta)]_j} \overline{[\cos m\varphi]_k} + \sum_{\ell=0}^L \sum_{m=1}^{\ell} B_{ilm} \overline{[P_{\ell}^m(\cos \Theta)]_j} \overline{[\sin m\varphi]_k} = \delta v_{ijk} \quad (IV-2)$$

weighted by σ_{ijk}^{-1} . The bars over the P_{ℓ}^m and $\cos m\varphi$ or $\sin m\varphi$ designate the average value for the j^{th} latitudinal or k^{th} longitudinal zone. It would appear that the weighted least-squares solution (W) should be preferred over the T solution, but the values of σ_{ijk} must be treated with some caution, as the sampling of individual blocks may be uneven. Thus, differences between the sets of A_{ilm} and B_{ilm} obtained using Eqs. (IV-1) and (IV-2) represent a measure of uncertainty in the actual values of the spherical harmonic coefficients.

We compute cross-correlation coefficients:

$$r = \frac{\sum_{\ell, m} A_{ilm} A'_{ilm} + B_{ilm} B'_{ilm}}{\left[\sum_{\ell, m} (A_{ilm}^2 + B_{ilm}^2) \cdot \sum_{\ell, m} (A'_{ilm}^2 + B'_{ilm}^2) \right]^{1/2}} \quad (IV-3)$$

(1) between the T and W solutions for each case separately to establish the level of consistency of the velocity perturbations depending on the method of derivation of coefficients, and (2) between Case I and II coefficients, separately for the T and W solutions, to investigate the stability of the solution with respect to a change in the discretization of the model. The coefficients A_0^0 are excluded; the coefficients B_3^3 and A_3^3 are excluded when cross-correlation between Case I and II solutions is evaluated, as one is indeterminate for each solution, respectively.

In Table IV-1, we list for these four cases the diagonal elements of the cross-correlation matrix. We note that in most cases the cross-correlation coefficients between the T and W solutions are on the order of 0.9; this means that these two different methods do not lead to

TABLE IV-1 CROSS-CORRELATION COEFFICIENTS BETWEEN T AND W SOLUTIONS				
	I T/I W†	II T/II W	I T/II T	I W/II W
Region I	0.960	0.793	0.085	0.276
Region IIA	0.913	0.813	0.064	0.009
Region IIB	0.854	0.502	0.315	0.541
Region III	0.881	0.833	0.895	0.930
Region IV	0.875	0.855	0.895	0.828
† Cross-correlation between T solution, Case I, and W solution, Case I. Other columns are labeled similarly.				

grossly different representations of velocity anomalies in terms of spherical harmonics. We also note that we obtain coefficients of cross-correlation between the Case I and Case II solutions that are nearly zero for Regions I and IIA, assume intermediate values for Region IIB, and are high (0.9) for Regions III and IV.

A plausible, but by no means unique, interpretation of this pattern of correlation coefficients is that lateral heterogeneities in the mantle above 1100 km depth are dominated by short wavelength features, with dimensions considerably below those of our grid pattern; the incoherent results represent the effect of a wavenumber bias due to uneven sampling by sources and receivers. The mantle below 1500 km on the other hand, could be dominated by heterogeneities of dimensions comparable with our block size, or greater, as the results do not appear to be sensitive to the position of boundaries between blocks. There may be a transition in the scale of heterogeneities in the depth range between 1100 and 1500 km.

In order to derive the final \bar{T} and \bar{W} solutions, we combine velocity perturbations determined for Case I and Case II. For the integration method (\bar{T}), this corresponds simply to averaging the coefficients obtained for both grid patterns, except for the terms A_3^3 and B_3^3 . The weighted least-squares solution (\bar{W}) is obtained by solving the system of 60 observational equations for each layer. The spherical harmonic coefficients obtained in this way are listed in Table IV-2.

The decay with angular order number of the magnitude of the spherical harmonic coefficients of the observed gravitational potential suggests that the source of the low-order anomalies is located in the deep mantle; such an interpretation is, of course, not the only one possible. We test this hypothesis by assuming that the density perturbations should be proportional to velocity perturbations. We supplement Eq. (IV-2) by equations of constraint:

$$\sum_i H_{il} A_{ilm} = \alpha C_{lm} \quad ; \quad \sum_i H_{il} B_{ilm} = \alpha S_{lm} \quad (\text{IV-4})$$

TABLE IV-2
SPHERICAL HARMONIC EXPANSION COEFFICIENTS OF FINAL \bar{T} AND \bar{W} SOLUTIONS

	Region I		Region IIA		Region IIB			Region III			Region IV		
	\bar{T}	\bar{W}	\bar{T}	\bar{W}	\bar{T}	\bar{W}	G^\dagger	\bar{T}	\bar{W}	G^\dagger	\bar{T}	\bar{W}	G^\dagger
A_0^0	1.9	1.6	-3.3	-1.5	22.0	21.0	23.9	-9.8	-10.3	-8.5	24.7	22.2	24.1
A_1^0	1.2	1.1	-1.5	-2.6	1.6	3.5	-0.3	-0.4	0.5	-1.7	4.2	6.3	4.7
A_1^1	-1.3	-1.8	2.3	1.2	0.4	0.0	-1.1	-0.8	-0.6	-0.8	-12.8	-12.3	-11.4
B_1^1	-1.5	-0.8	2.1	-0.1	0.4	1.2	0.2	0.3	0.2	-0.1	-1.9	-2.3	-1.8
A_2^0	-0.4	0.1	0.9	-0.4	2.4	0.6	2.9	5.2	4.5	5.8	0.6	-0.1	1.7
A_2^1	-0.7	-0.9	-2.0	0.3	1.0	4.9	5.9	-0.4	-0.5	0.1	4.9	1.4	2.3
B_2^1	1.6	3.8	-0.4	-1.3	-2.3	-2.3	0.0	0.9	1.2	3.2	1.8	1.8	3.1
A_2^2	0.6	-1.6	2.3	7.6	-8.6	-9.7	-10.6	2.0	4.8	5.0	-0.8	-2.5	-0.6
B_2^2	-0.4	-0.8	1.3	2.2	-1.7	-1.6	3.0	-2.9	-4.0	-1.3	-1.7	-0.1	2.7
A_3^0	3.1	4.6	0.3	0.6	0.2	1.0	2.3	-4.9	-3.5	-2.6	-6.1	-8.5	-8.0
A_3^1	1.8	3.1	0.7	-1.8	3.2	-4.1	-3.8	-0.2	-2.8	-2.9	-3.4	-2.0	-2.5
B_3^1	-0.9	-3.6	4.3	7.6	0.3	-0.6	-1.6	0.1	0.7	-0.6	1.5	4.6	3.3
A_3^2	0.8	2.0	-2.5	-5.7	1.2	-3.3	3.0	-3.1	-8.8	-5.0	-4.1	-5.4	-2.2
B_3^2	-3.1	-4.6	-0.2	-1.0	1.4	2.7	2.4	2.6	3.2	3.5	0.1	-7.3	-7.0
A_3^3	-1.1	-4.2	2.5	6.0	-2.2	-1.8	1.7	-3.9	-4.9	-2.5	-8.0	-5.8	-3.4
B_3^3	-3.9	-5.7	7.8	6.7	-3.5	-4.5	-3.1	-0.3	0.9	1.4	-7.2	-11.3	-10.3

† Columns G list coefficients of the velocity anomalies that give an exact match to geopotential of degree 2 and 3 assuming $\delta v/\delta \rho = -6(\text{km/sec})/(\text{g/cm}^3)$. These values have been obtained by an appropriate perturbation of the \bar{W} solutions for Regions IIB, III, and IV. The units are m/sec.

where $H_{i\ell}$ is the density kernel:

$$H_{i\ell} = \frac{3}{\bar{\rho}(2\ell + 1)(\ell + 3)} [(r_{i+1}/a)^{\ell+3} - (r_i/a)^{\ell+3}] \quad ; \quad (IV-5)$$

$C_{\ell m}$ and $S_{\ell m}$ are the observed geopotential coefficients (for C_2^0 we have used the value of Jeffreys¹⁰ and the results of Gaposchkin¹¹ for the remaining 9 coefficients) and α is the proportionality coefficient:

$$\delta v = \alpha \delta \rho \quad .$$

Solutions are found for a wide range of values of the parameter α . We choose the value of α that requires the minimum perturbation in the observed velocity field.

We find the "best" value of α to be $-6 \text{ (km/sec)/(g/cm}^3\text{)}$, assuming that the density perturbations are limited to Regions IIA, III, and IV. In Fig. IV-14, we compare the contours of velocity anomalies obtained from the original \bar{W} solution (broken lines) with the solution that gives an exact match to the gravity field for $\alpha = -6$ (solid lines). The spherical harmonic coefficients obtained from this solution are incorporated in Table IV-2, columns G. The changes in the pattern of velocity anomalies are not substantial. It should be remembered that the velocity distribution maps contain contributions of all the harmonics with $\ell = 1, 2, 3$. Some of these harmonics are not considered in comparison with the gravity field.

The negative value of the proportionality coefficient α suggests several possibilities for the origin of the lower mantle velocity anomalies: (1) sinking of dense, low-velocity material into the lower mantle from regions of lithospheric subduction;^{12,13} (2) chemical plumes of light, high-velocity material originating near the core-mantle boundary;¹⁴ (3) temperature differences and perturbation of the core-mantle boundary and the Earth's surface associated with mantle wide convection, and (4) static chemical heterogeneities in a non-convecting mantle.

The first three alternatives, all involving flow in the lower mantle, may be complementary, but act on a different time scale.

There appears to be a westward or northwestward translation of some anomalies with respect to the pattern obtained for the innermost shell. In particular, the direction of translation of a large negative anomaly under the Pacific is in agreement with the sense of motion of the Pacific plate. We must caution the reader, however, that this is a highly speculative interpretation. If correct, it would favor the convective hypotheses.

A. M. Dziewonski
B. H. Hager[†]
R. J. O'Connell[†]

D. INTERNAL DISCONTINUITIES IN THE EARTH'S STRUCTURE AND PERTURBATION THEORY

Inversion of free oscillation data¹⁵⁻¹⁷ has led to the currently preferred value for the radius of the core-mantle boundary ($3485 \pm 3 \text{ km}$).¹⁸ This value has since been strongly supported by body wave studies.¹⁹ This "success" may be in retrospect somewhat surprising, as it has recently become apparent that the differential kernels used to predict changes in eigenfrequencies of spheroidal and radial modes due to perturbations in the core radius were, in fact, grossly erroneous.

[†] Department of Geological Sciences, Harvard University, Cambridge, MA 02138.

Backus and Gilbert²⁰ were the first to propose an expression for perturbation of the eigenfrequency of a normal mode due to a change in location of a discontinuity (see their Appendix B). Their equation (52), hereafter referred to as L, was derived by what is now known to be an incomplete application of the Rayleigh variational principle. The L formula was criticized by Wiggins,²¹ but he failed to provide a rigorous alternative procedure. In Table IV-3, we compare results obtained by application of the L formula with exact calculations. The values listed correspond to a relative change in eigenfrequency due to a 1-km increase in the radius of a discontinuity. The "exact" values represent the relative difference between the eigenfrequencies of the perturbed and original model PEM-A (Ref. 22) computed by solving the appropriate system of differential equations. These eigenfrequencies are determined with a relative precision of

TABLE IV-3						
RELATIVE CHANGE IN EIGENFREQUENCY ($\times 10^3$) DUE TO A 1-km INCREASE IN THE RADIUS OF DISCONTINUITIES IN MODEL PEM-A (Ref. 22)						
Mode	Core-Mantle Boundary			670-km Disk		
	L	Exact	H	L	Exact	H
$0S_0$	-0.0968	-0.0955	-0.0954	-0.0092	-0.0024	-0.0024
$5S_0$	0.0785	-0.0781	-0.0780	-0.0254	0.0158	0.0157
$0S_2$	-0.4652	-0.2271	-0.2270	-0.0117	0.0149	0.0149
$0S_{15}$	-0.0012	-0.0026	-0.0026	-0.1262	0.0884	0.0884
$0S_{30}$	0.0000	-0.0004	-0.0005	-0.0821	0.1089	0.1085
$0S_{60}$	0.0000	-0.0001	-0.0001	-0.0042	0.0072	0.0071
$1S_8$	-0.6586	-0.1077	-0.1081	-0.0187	0.0162	0.0162
$1S_{61}$	0.0000	-0.0001	-0.0001	-0.1260	0.1276	0.1271
$6S_1$	0.0211	-0.0133	-0.0131	-0.0317	0.0241	0.0240
$0T_4$	-0.0345	-0.0346	-0.0345	-0.0407	0.0609	0.0608
$0T_{15}$	0.0000	0.0000	0.0000	0.0251	0.0940	0.0938
$0T_{30}$	0.0000	0.0000	0.0000	0.0058	0.0370	0.0368
$0T_{60}$	0.0000	0.0000	0.0000	0.0003	0.0032	0.0032
$1T_{43}$	0.0000	0.0000	0.0000	0.0819	0.1376	0.1371
$2T_4$	0.1716	0.1717	0.1716	-0.0776	0.0697	0.0694
† Columns L and H refer to the Lograngian and Homiltonion representotions, respectively.						

at least 10^{-7} . The corresponding values differ significantly; for the 670-km discontinuity, the L formula yields a wrong sign for all the radial and spheroidal modes listed, with the exception of ${}_0S_0$.

This result was communicated to several scientists, and the source of the error in the L formula was detected almost immediately by Dr. J. H. Woodhouse. He has shown²³ that a correct application of the Rayleigh principle, in which all pertinent variations are included, leads to an expression (formula H) that is significantly different from the L formula, with the exception of those boundaries at which tractions vanish (free surface, core-mantle boundary for toroidal modes). Algebraic details can be found in Woodhouse²³ and Dziewonski and Sailor.²⁴ Results obtained using the H formula are incorporated in Table IV-3; the agreement with "exact" calculations is excellent.

Note that for the toroidal modes ${}_0T_4$ and ${}_2T_4$ both L and H formulas give identical results at the core-mantle boundary. Also, for spheroidal modes, the signs are the same even though the absolute values differ. It is for this reason that inversion of a combined set of over 1000 normal modes yielded, after several iterations, a correct value for the core radius,¹⁷ in spite of the fact that the incorrect L formula was applied.

Differential kernels for perturbations in the phase velocity due to a change in depth to a discontinuity (such as Moho) are required in the inversion of surface wave dispersion data. For an increase δh in the depth of a discontinuity located in the original model at $z = -h$, the change in phase velocity c measured at a constant frequency ω is

$$(\delta c/c)_{\omega} = \frac{1}{2} \frac{c}{u} \delta h [\kappa \tilde{K} + \mu \tilde{M} + \rho \tilde{R}]_{z=-h}^+,$$

where u is the group velocity and

$$\tilde{K} = k^2 V^2 - (\partial_z U)^2,$$

$$\tilde{M} = \frac{1}{3} [(2\partial_z U)^2 - (kV)^2] + (kU)^2 - (\partial_z V)^2 + (kV)^2 - (\partial_z W)^2 + (kW)^2,$$

$$\tilde{R} = -\omega^2 (U^2 + V^2 + W^2);$$

U and V are the scalar vertical and horizontal displacement functions for Rayleigh waves, W is the displacement function for Love waves, and k is the wavenumber. The functions U , V , and W are normalized such that:

$$\omega^2 \int_{-\infty}^0 \rho (U^2 + V^2) dz = 1; \quad \omega^2 \int_{-\infty}^0 \rho W^2 dz = 1.$$

The effect of changes in radii of discontinuities is also important in evaluation of multiplet splitting for a laterally heterogeneous earth. The original equations^{25,26} for the splitting due to ellipticity were derived using the same incorrect approach that led to the L formula. Numerical calculations²⁷ based on this approach give very large ellipticity splitting parameters for earth models with discontinuities in the upper mantle. It was this intuitively unexpected result that originally led the first two of us to reexamination of the entire problem. Dziewonski and Sailor²⁴ and Dahlen²⁸ have now derived correct equations for the ellipticity splitting. Further theoretical development is needed for the general case of a laterally heterogeneous earth model.

In Figs. IV-15 and -16, we compare for three earth models the results obtained for the ellipticity splitting parameter α_ϵ defined by Dahlen²⁵ using the correct (H) and incorrect (L) formulas for contribution from discontinuities. All three models yield numerical results which are very close to each other when the correct equations are applied. Differences in α_ϵ , in the period range shown, are of the order of 1/300 for spheroidal modes, much below the thickness of the line. They reach 1.5 percent for the toroidal modes at 150 sec, but for simplicity we have shown only $\alpha(T)$ for PEM-A as representative of all three models.

Since both ellipticity and rotational splitting are, for practical purposes, essentially independent of the details of an acceptable earth model, in Table IV-4 we list for future reference

TABLE IV-4 FUNCTIONS χ_1 AND χ_2 ($\times 10^3$) OF DAHLEN ²⁷ COMPUTED FOR MODEL PEM-A (Ref.22)						
Period (sec)	Rayleigh Wave			Love Wave		
	c_0/u_0	χ_1	χ_2	c_0/u_0	χ_1	χ_2
100	1.066	-0.015	0.617	1.052	0.014	0.610
125	1.110	-0.004	0.656	1.069	0.023	0.629
150	1.158	0.004	0.699	1.086	0.034	0.650
175	1.212	0.007	0.746	1.103	0.047	0.672
200	1.268	0.004	0.797	1.120	0.064	0.695
225	1.325	-0.010	0.846	1.138	0.083	0.720
250	1.373	-0.039	0.889	1.155	0.102	0.745
275	1.405	-0.089	0.918	1.171	0.132	0.770
300	1.418	-0.160	0.930	1.186	0.161	0.795
325	1.414	-0.249	0.926	1.199	0.194	0.819
350	1.398	-0.346	0.912	1.211	0.231	0.842
375	1.378	-0.443	0.894	1.221	0.272	0.865
400	1.357	-0.531	0.876	1.229	0.316	0.886
425	1.338	-0.605	0.859	1.235	0.363	0.906
450	1.320	-0.662	0.843	1.239	0.414	0.925
475	1.301	-0.697	0.826	1.241	0.468	0.942
500	1.279	-0.705	0.806	1.242	0.526	0.959

functions $\chi_1(T)$ and $\chi_2(T)$ in Eq. (27) of Dahlen²⁷ for the apparent length of a great circular path:

$$L_{app}(T, \Theta) = 2\pi a [1 - \chi_1(T) \cos \Theta - \chi_2(T) (1 - 3 \cos^2 \Theta)]$$

where a is the average earth radius, T is the period, and Θ is the colatitude of the pole of the great circular path ($\Theta = 0^\circ$ for a wave traveling along the equator from west to east; $\Theta = 180^\circ$ for the wave traveling in the opposite direction), and χ_1 and χ_2 are functions dependent on the

rotational and ellipticity splitting, respectively. The values, listed together with the ratios c_0/u_0 , have been computed for model PEM-A (Ref. 22).

A. M. Dziewonski
R. V. Saylor[†]
F. A. Dahlen[‡]

E. TRANSMISSION HOLOGRAPHY WITH IMPULSIVE SOURCES

The isolation of that part of the seismogram due to scattering provides data on the non-radially symmetric part of the velocity structure and an accurate picture of the source waveform. In the high-frequency limit, the path effect can be approximated by ray theory but as much as 50 percent of the energy in a short-period seismogram cannot be so explained and must be attributed to higher order scattering. Chernov's²⁹ acoustic scattering model has been applied to array data from NORSAR, LASA,³⁰ Garm, and California. The spatial correlation function determined for LASA and NORSAR² reveals that the scattering is not due to isotropic random inhomogeneities. Additionally, high-resolution frequency-wavenumber analysis of seismic energy from local strip-mine explosions at LASA³¹ demonstrates that single scattering is not the cause of observed near-field seismic signatures.

An alternative to statistical studies is the direct inversion of travel-time residuals into estimates of the velocity structure.³² The method requires: a large number of events whose ray paths uniformly sample the structure under consideration, an initial phase assumption for each event, and a known first-order velocity structure. The over-determined inverse problem is numerically difficult to solve and may result in non-unique solutions. An entirely different approach to the scattering problem is to downward propagate the observed wavefields. This backward propagation technique is analogous to optical holography methods and can be expressed in the same mathematical form. Application of the holographic technique and the resulting differences from a ray theory inversion can be illustrated by a homogeneous half-space model containing a number of anomalous velocity structures. In Fig. IV-17, it can be seen that the ray path A-A' does not sample the anomalous velocity regions l_1 and l_2 . However, the recorded wavefield will contain not only the unperturbed signal but also the scattered wavefronts from l_1 and l_2 . The superposition of the waves from all the sources, both virtual and primary, can be represented by a time-dependent complex amplitude distribution over the surface plane (x, y) . The amplitude distribution at a given time can be represented by:³³

$$A(x, y, 0) = a(x, y) \exp[i\varphi(x, y)]$$

The relation between this complex amplitude distribution and the complex amplitude distribution $B(x, y, z_0)$ at depth z_0 can be written as:

$$B(x, y, z_0) = \frac{i}{\lambda} \iint A(\xi, \eta, 0) \cdot T(x, y, \xi, \eta) d\xi d\eta$$

where

$$T = \frac{1}{r} \exp[-ikr] \cos(\hat{n} \cdot \hat{r}) ,$$

[†] Department of Geological Sciences, Harvard University, Cambridge, MA 02138.

[‡] Department of Geological and Geophysical Sciences, Princeton University, Princeton, NJ 08540.

\hat{n} is the normal vector to the (x, y) plane, and \hat{r} is the vector connecting the point (x, y, z_0) with the point $(\xi, \eta, 0)$.

It can be seen from this relation that each point $(\xi, \eta, 0)$ maps to every point in the (x, y, z_0) plane and vice versa. This is essentially Huygen's principle which states that each point on a plane which intersects a wavefield can be considered a point radiator. Thus, theoretically, only one recorded wavefield over a plane is needed to recover lateral variations in velocity beneath the plane. In practice, many events will be needed to average the effects of errors in the data and errors due to undersampling in the observation plane.

The actual mechanics of recovering the wavefield at various depths can take a number of forms. The most straightforward technique is to merely replace the double integral in the above equation and evaluate the contributions from each point in the surface plane. This brute-force technique was used to obtain results shown earlier.² Another promising method being studied utilizes backward wave equation propagation based on the theory of Claerbout³⁴ and Landers and Claerbout.³⁵ For these techniques, better resolution can be obtained by utilizing broadband sources.

In conjunction with the numerical experiments, a laboratory experiment using impulsive sources is currently nearing completion. The apparatus uses a broadband piezoelectric source which generates 2-MHz pulses, a movable transducer that records P-waves and epoxy block velocity models. The source and receiver may be used in any array geometry by summing the results of different experiments. The laboratory experiments will provide data about wavefields produced by a number of known inhomogeneities. Experiments involving irregular interfaces and irregularly shaped velocity anomalies including liquid-filled cavities similar to magma chambers are planned.

J. Scheimer
T. E. Landers

REFERENCES

1. Seismic Discrimination SATS, Lincoln Laboratory, M.I.T. (30 June 1975), DDC AD-A014793/4.
2. Seismic Discrimination SATS, Lincoln Laboratory, M.I.T. (31 December 1975), DDC AD-A025777.
3. L. Knopoff and J. A. Hudson, "Scattering of Elastic Waves by Small Inhomogeneities," *J. Acoust. Soc. Am.* 36, 338-343 (1964).
4. L. Knopoff and J. A. Hudson, "Frequency Dependence of Amplitudes of Scattered Elastic Waves," *J. Acoust. Soc. Am.* 42, 18-20 (1967).
5. D. Davies and R. M. Sheppard, "Lateral Heterogeneity in the Earth's Mantle," *Nature* 239, 318-323 (1972).
6. Seismic Discrimination SATS, Lincoln Laboratory, M.I.T. (30 June 1973), DDC AD-766559.
7. K. A. Berteussen, "Array Analysis of Lateral Inhomogeneities in the Deep Mantle," *Earth Planet. Sci. Lett.* 28, 212-216 (1975).
8. E. S. Husebye, R. Kaneström, and R. Rud, "Observations of Vertical and Lateral P-velocity Anomalies in the Earth's Mantle Using the Fennoscandian Continental Array," *Geophys. J. R. Astr. Soc.* 25, 3-16 (1971).
9. A. M. Dziewonski, B. H. Hager, and R. J. O'Connell, "Large Scale Heterogeneities in the Lower Mantle," *J. Geophys. Res.* (in press).
10. H. Jeffreys, "On the Hydrostatic Theory of the Figure of the Earth," *Geophys. J. R. Astr. Soc.* 8, 196-202 (1963).
11. E. M. Gaposchkin, "Earth's Gravity Field to the Eighteenth Degree and Geocentric Coordinates for 104 Stations from Satellite and Terrestrial Data," *J. Geophys. Res.* 79, 5377-5411 (1974).
12. A. E. Ringwood, "Composition and Evolution of the Upper Mantle," in *The Earth's Crust and Upper Mantle*, P. Hart, Ed., *Am. Geophys. Union Monograph* 13, 1-17 (1969).
13. A. E. Ringwood, "Phase Transformations and Mantle Dynamics," *Earth Planet. Sci. Lett.* 14, 233-241 (1972).
14. D. L. Anderson, "Chemical Plumes in the Mantle," *Geol. Soc. Am. Bull.* 86, 1593-1600 (1975).
15. F. Gilbert, A. M. Dziewonski, and J. N. Brune, "An Informative Solution to a Seismological Inverse Problem," *Proc. Natl. Acad. Sci.* 70, 1410-1413 (1973).
16. T. H. Jordan and D. L. Anderson, "Earth Structure from Free Oscillations and Travel Times," *Geophys. J. R. Astr. Soc.* 36, 411-460 (1974).
17. F. Gilbert and A. M. Dziewonski, "An Application of Normal Mode Theory to the Retrieval of Structural Parameters and Source Mechanisms from Seismic Spectra," *Phil. Trans. R. Soc. London* A278, 187-269 (1975).
18. A. M. Dziewonski and R. A. W. Haddon, "The Radius of the Core-Mantle Boundary Inferred from Travel Time and Free Oscillation Data; A Critical Review," *Phys. Earth Planet. Inter.* 9, 28-35 (1974).
19. E. R. Engdahl and L. E. Johnson, "Differential PcP Travel Times and the Radius of the Core," *Geophys. J. R. Astr. Soc.* 39, 435-456 (1974).
20. G. E. Backus and J. F. Gilbert, "Numerical Applications of a Formalism for Geophysical Inverse Problems," *Geophys. J. R. Astr. Soc.* 13, 247-276 (1967).
21. R. A. Wiggins, "Terrestrial Variational Tables for the Periods and Attenuation of Free Oscillations," *Phys. Earth Planet. Inter.* 1, 201-266 (1968).

22. A. M. Dziewonski, A. L. Hales, and E. R. Lapwood, "Parametrically Simple Earth Models Consistent with Geophysical Data," *Phys. Earth Planet. Inter.* 10, 12-48 (1975).
23. J. H. Woodhouse, "On Rayleigh's Principle," *Geophys. J. R. Astr. Soc.* 46, 11-22 (1976).
24. A. M. Dziewonski and R. V. Sailor, "Comments on 'The Correction of Great Circular Surface Wave Phase Velocity Measurements from the Rotation and Ellipticity of the Earth' by F. A. Dahlen," *J. Geophys. Res.* (in press, 1976).
25. F. A. Dahlen, "The Normal Modes of a Rotating, Elliptical Earth," *Geophys. J. R. Astr. Soc.* 16, 329-367 (1968).
26. F. A. Dahlen, "Inference of the Lateral Heterogeneity of the Earth from Eigenfrequency Spectrum: A Linear Inverse Problem," *Geophys. J. R. Astr. Soc.* 38, 143-167 (1974).
27. F. A. Dahlen, "The Correction of Great Circular Surface Wave Phase Velocity Measurements from the Rotation and Ellipticity of the Earth," *J. Geophys. Res.* 80, 4895-4903 (1975).
28. F. A. Dahlen, "Reply to Comments by A. M. Dziewonski and R. V. Sailor on 'The Correction of Great Circular Surface Wave Phase Velocity Measurements from the Rotation and Ellipticity of the Earth' by F. A. Dahlen," *J. Geophys. Res.* (in press, 1976).
29. L. A. Chernov, in Wave Propagation in a Random Medium, translated by R. A. Silverman (McGraw-Hill, New York, 1960).
30. K. Aki, "Scattering of P-waves Under the Montana LASA," *J. Geophys. Res.* 78, 1334-1358 (1973).
31. J. F. Scheimer, "Analysis of Coherent and Incoherent Energy in LASA Seismograms as Related to Single and Multiple Scattering Theory" (in preparation).
32. K. Aki, A. Christoffersson, and E. S. Husebye, "Three-Dimensional Seismic Structure of the Lithosphere Under Montana LASA," *Bull. Seismol. Soc. Am.* 66, 501-524 (1976).
33. A. Sommerfeld, Optics (Academic Press, New York, 1964), pp. 199-201.
34. J. F. Claerbout, in Fundamentals of Geophysical Prospecting (McGraw-Hill, New York, 1976), pp. 184-263.
35. T. E. Landers and J. F. Claerbout, "Numerical Calculations of Elastic Waves in Laterally Inhomogeneous Media," *J. Geophys. Res.* 77, No. 8, 1476-1482 (1972).

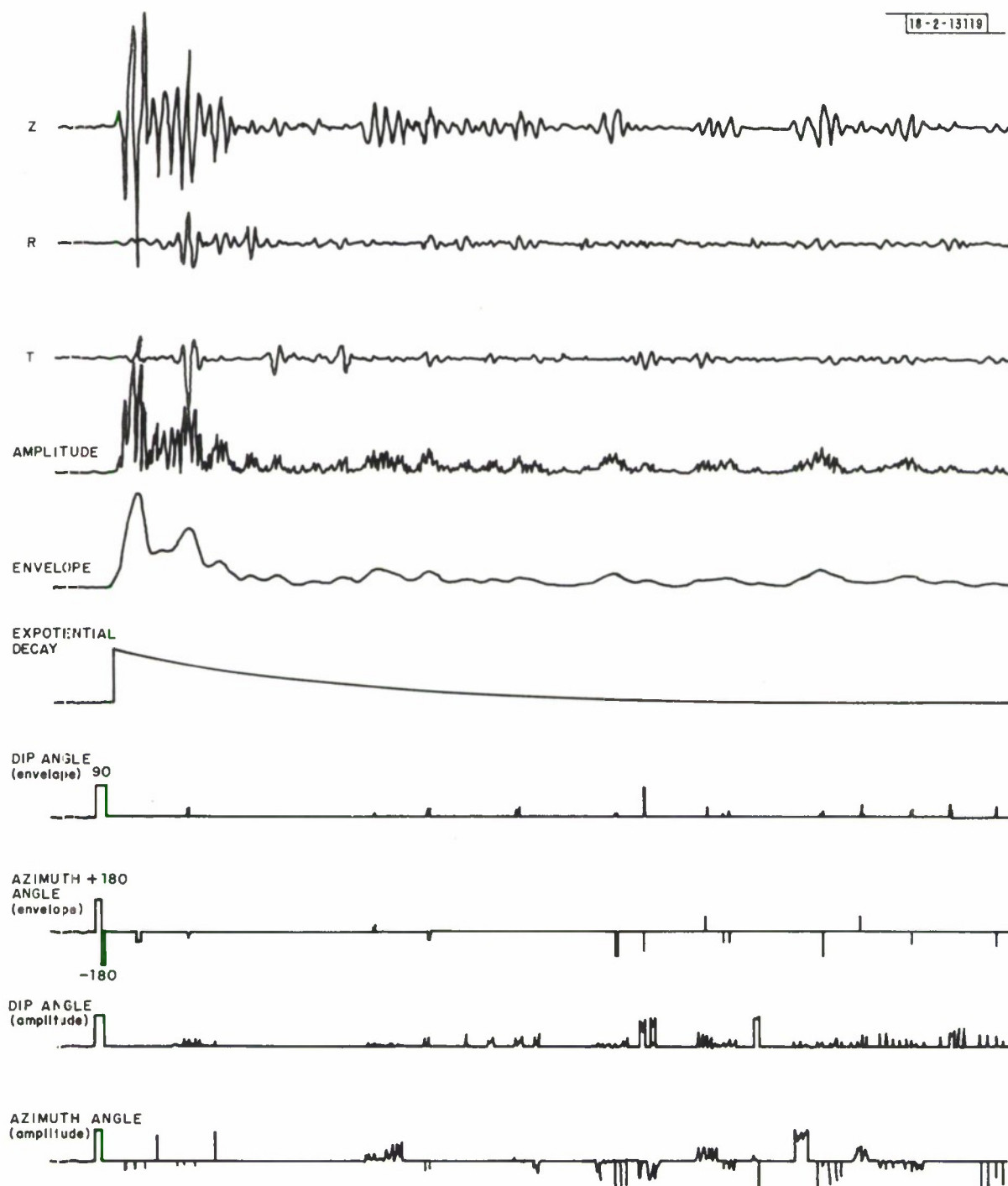


Fig. IV-1. Amplitude, envelope, and exponential traces for the polarized coda of event 1.

TOWARD NOVAYA ZEMLYA

18-2-13120

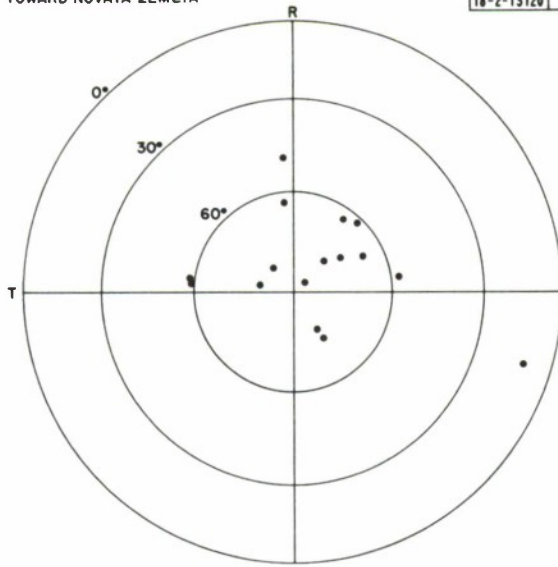


Fig. IV-2. Equal area projection of particle motion direction for peaks of envelope trace for the 1st minute data of event 1. The rings are at 60°, 30°, and 0° emergence angle.

TOWARD NOVAYA ZEMLYA

18-2-13121

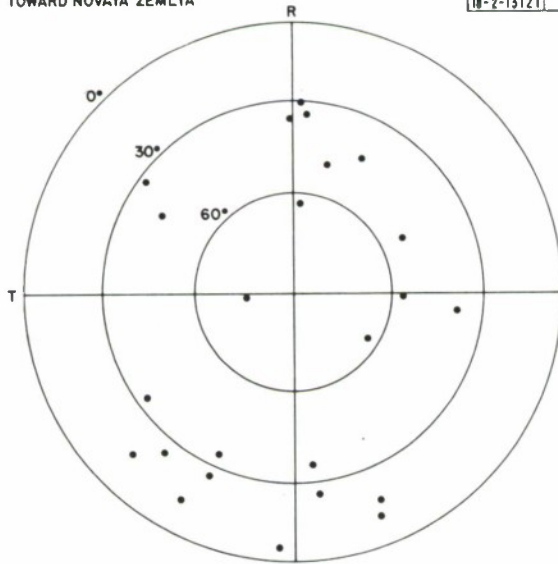


Fig. IV-3. Equal area projection envelope peaks of 2nd minute data.

TOWARD NOVAYA ZEMLYA

18-2-13122

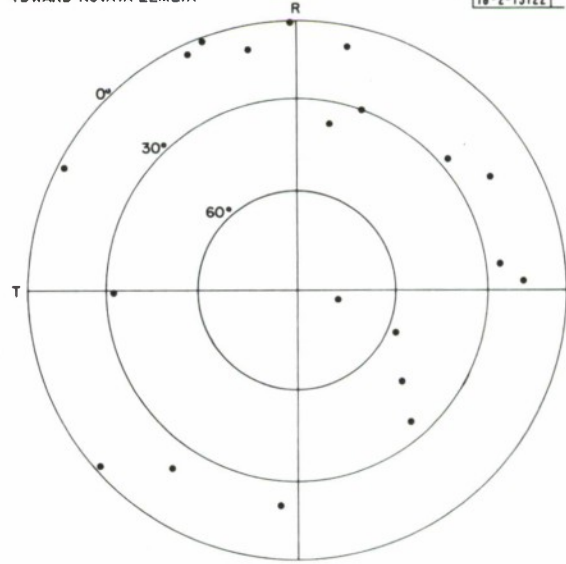


Fig. IV-4. Equal area projection envelope peaks for 3rd minute data.

Fig. IV-5. Equal area projection envelope peaks for 4th minute data.

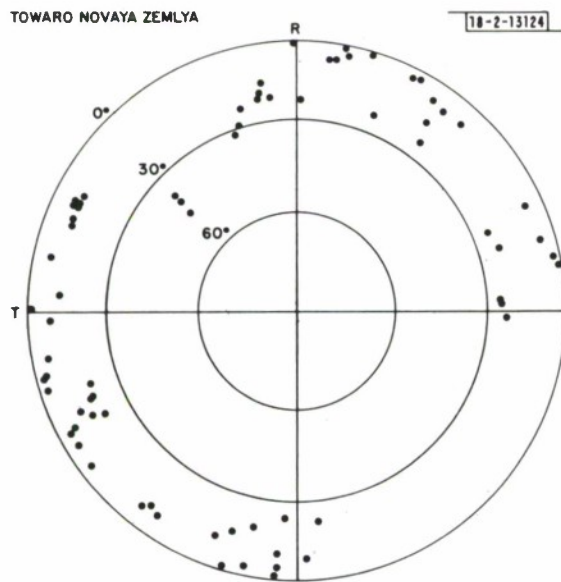
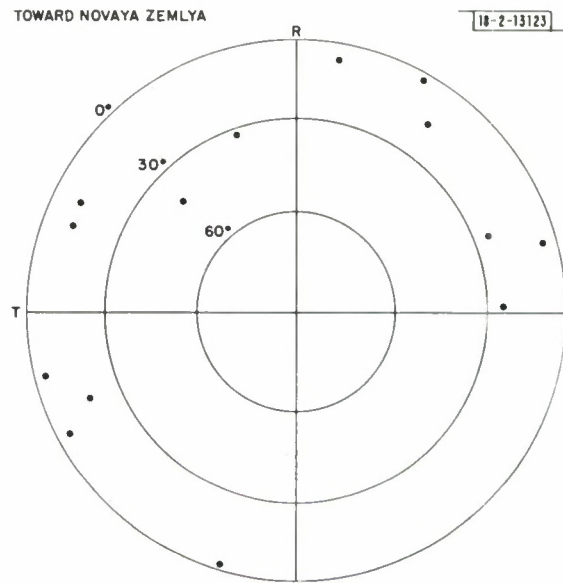


Fig. IV-6. Equal area projection for 4th minute data using peaks in amplitude trace.

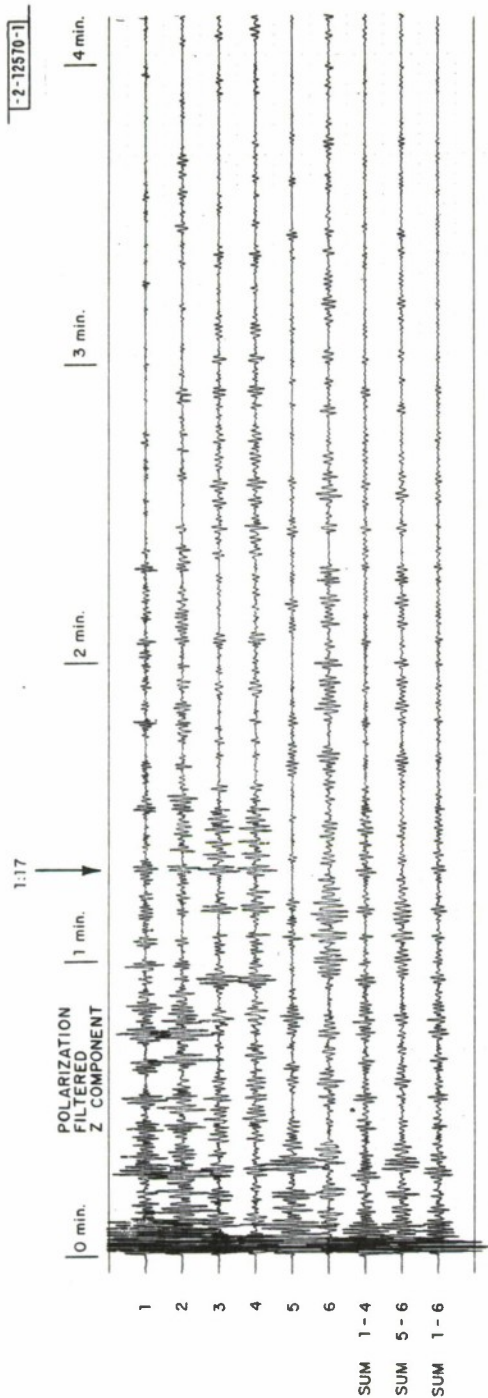


Fig. IV-7. Z components of the polarized data for 6 Novaya Zemlya events. The impulsive pulses are body waves predominantly P type.

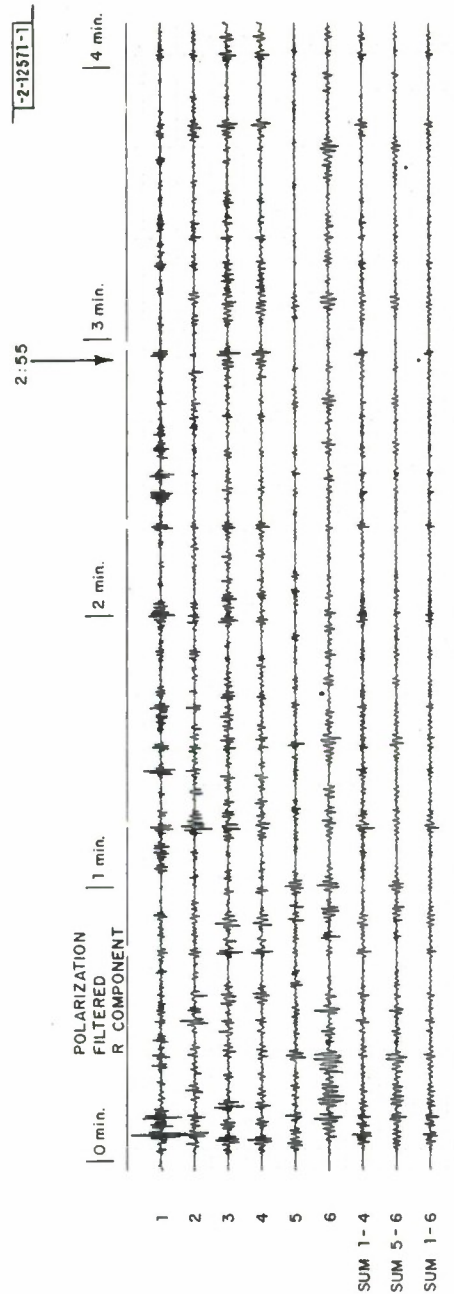


Fig. IV-8. Radial component of the polarized data for 6 Novaya Zemlya events. Plotting gain is the same as for Fig. IV-7.

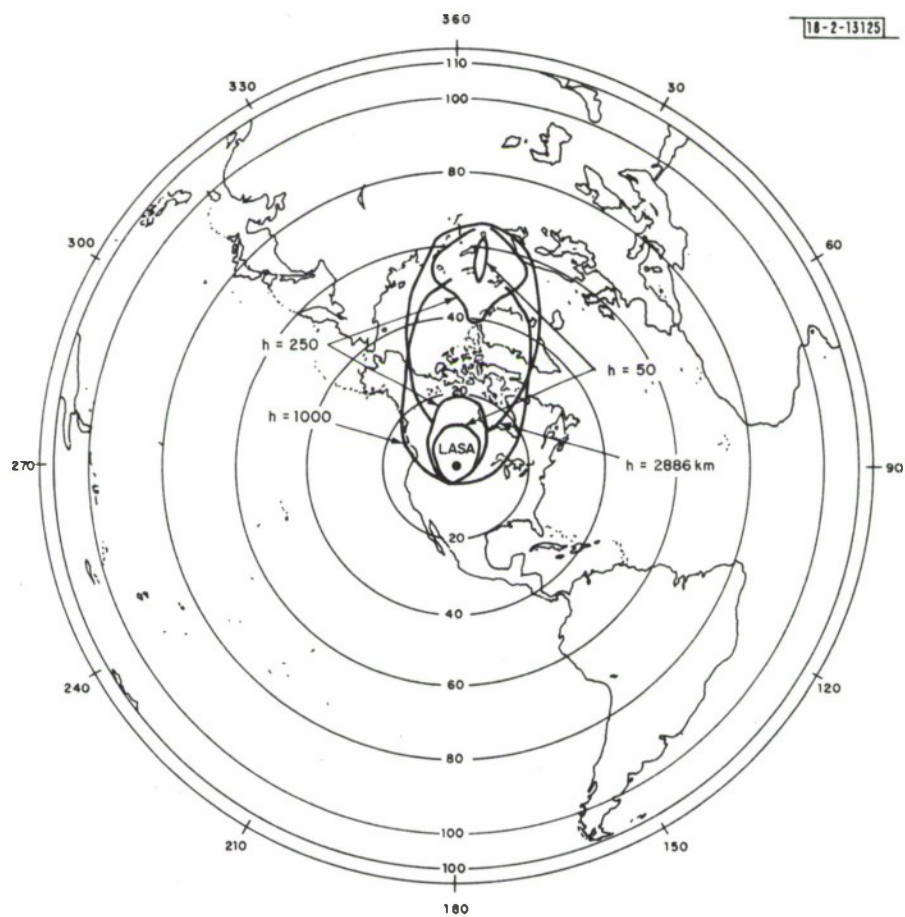


Fig. IV-9. P-to-P scattering region for phase arriving at 1 min. 17 sec after initial P phase. Contours indicate epicenter for the same depth.

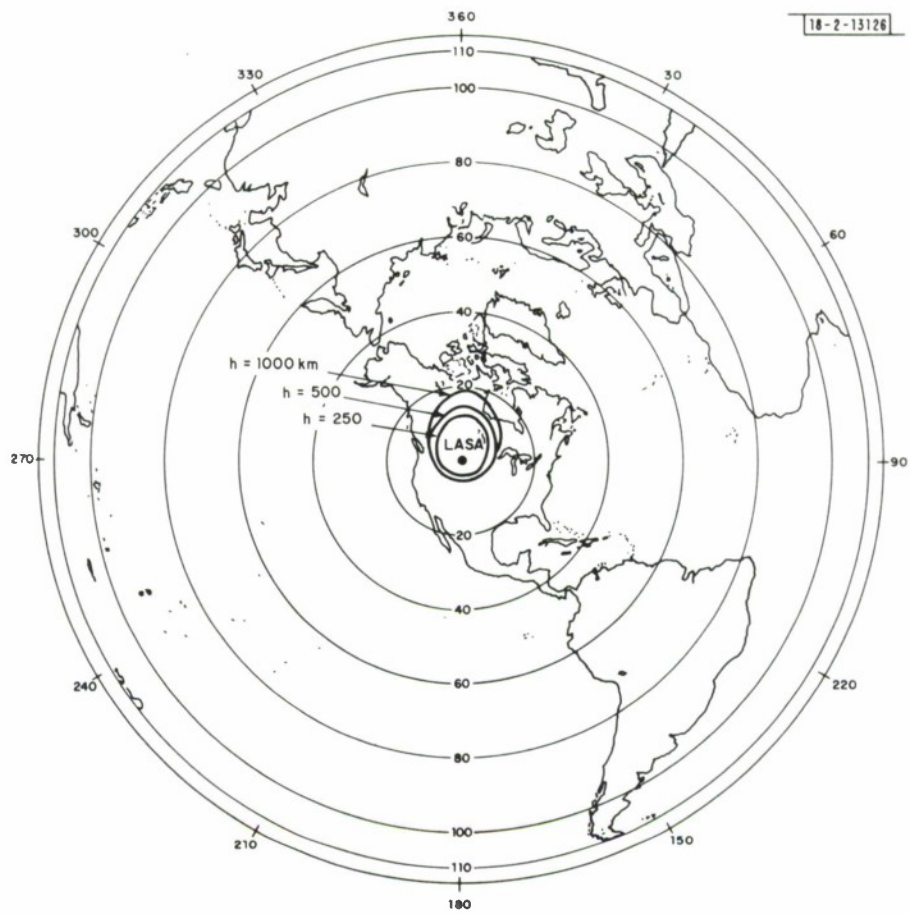


Fig. IV-10. P-to-S scattering region for phase arriving at 2 min. 55 sec after initial P phase. Contours indicate epicenter for the same depth.

Fig. IV-11. Mislocations on Scandinavian network of events in the China-Russian border region. Head and tail of the arrows represent the reference and the observed location, respectively. The explosion site in Eastern Kazakh is near (50°N , 78°E).

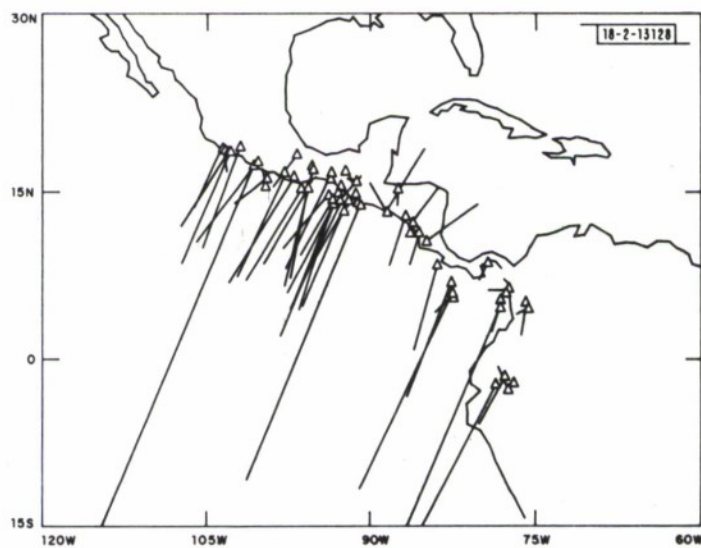
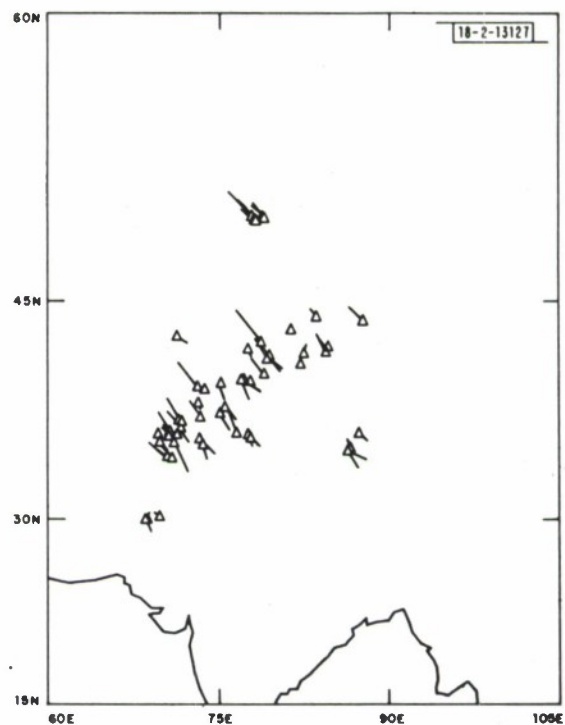


Fig. IV-12. Mislocations on Scandinavian network of events in Central America.

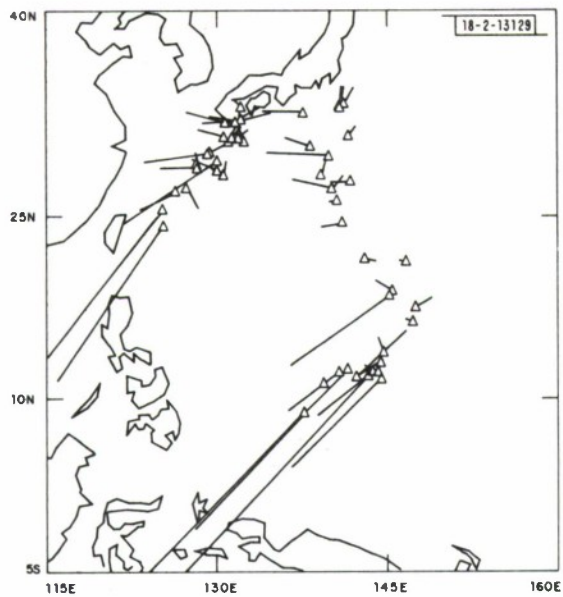
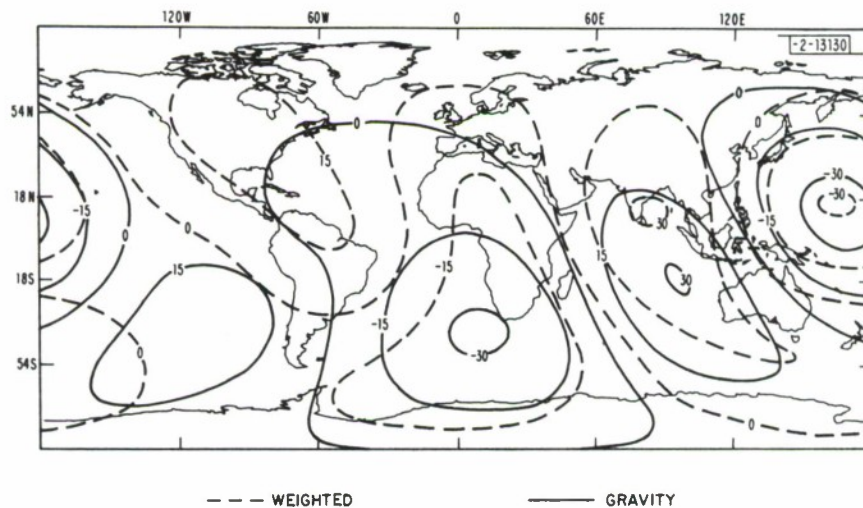
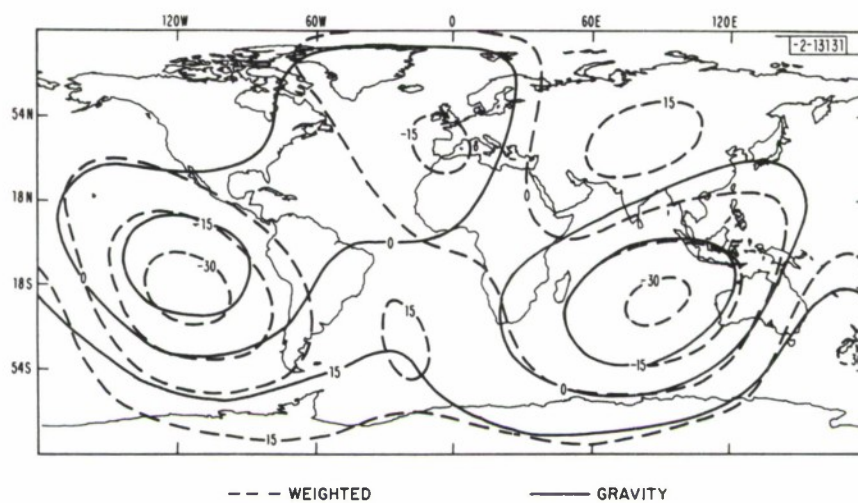


Fig. IV-13. Mislocations on Montana network of events in Bonin, Mariana, and Ryukyu.

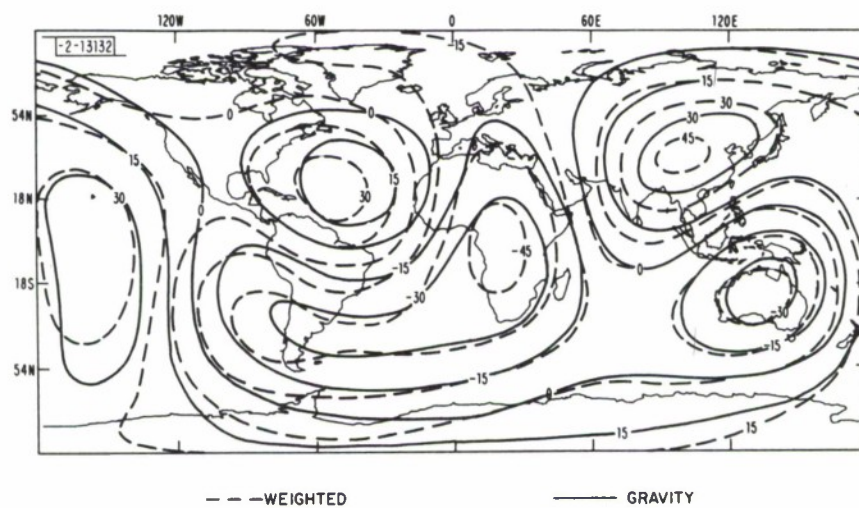


(a)

Fig. IV-14. Velocity anomalies in (a) Region IIB (1100 to 1500 km), (b) Region III (1500 to 2200 km), and (c) Region IV (2200 km to core-mantle boundary). Contours indicated by broken line represent the \bar{W} solution of Table IV-2; solid contours correspond to the solution perturbed to satisfy the gravity data (G). The results in this figure correspond to inversion for a five-shell model of 693,495 data corrected for ellipticity and station anomalies. Contour units - m/sec.



(b)



(c)

Fig. IV-14. Continued.

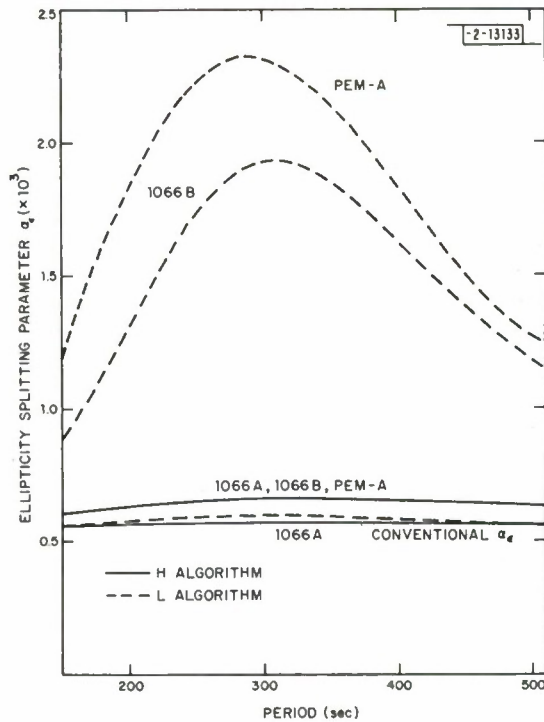


Fig. IV-15. Comparison of ellipticity splitting parameters for the fundamental spheroidal mode computed for three earth models. Only the algorithm based on Hamiltonian representation (H algorithm) gives correct results. The horizontal line represents the asymptotic value ($l \rightarrow \infty$) of the splitting parameter.

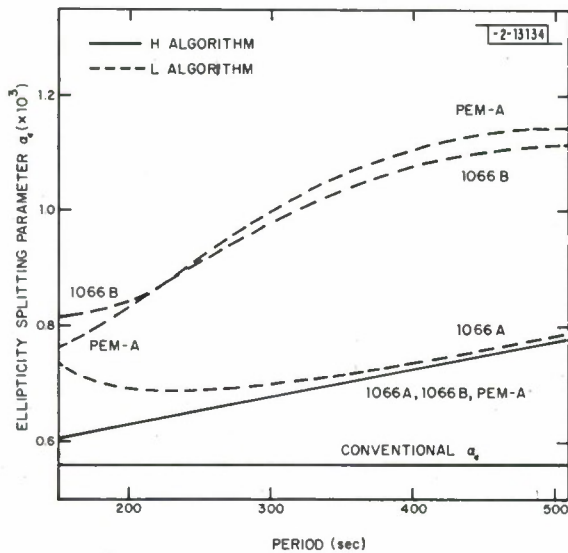


Fig. IV-16. Same as Fig. IV-15, but for the fundamental toroidal mode.

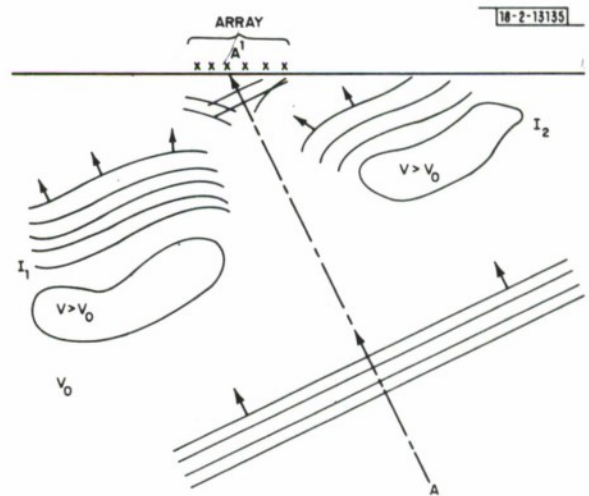


Fig. IV-17. Model of a simple medium illustrating that the array receives information from inhomogeneities that are not intercepted by the geometrical ray path. The inhomogeneities are regions of higher velocity than the surrounding medium.

V. MISCELLANEOUS STUDIES

A. MODEL ORDER CRITERIA APPLIED TO AUTOREGRESSIVE AND NON-AUTOREGRESSIVE PROCESSES

Determining the proper filter length to use is crucial to estimating the spectrum by the maximum entropy method. Several estimating procedures for determining the order of autoregressive series have been developed and the equivalence between maximum entropy and autoregressive analysis demonstrated.¹ Here a study of these procedures for both autoregressive and non-autoregressive series is presented.

Zero mean autoregressive processes have the following form

$$X_t = A_1 X_{t-1} + A_2 X_{t-2} + \dots + A_p X_{t-p} + \epsilon_t$$

where ϵ_t is zero mean and uncorrelated. ϵ_t is referred to as the innovation. Thus, the time series X_t is predictable from a linear combination of its past values to a random error. Various ways of estimating the A_i 's are available² and will not be discussed here. The determination of the value of the order of the process, p , is a major problem in the analysis and is the subject of this research.

The following methods have been proposed to estimate p . Akaike³ suggested that the minimum of the average error due to estimating the autoregressive coefficients and the innovation for one step prediction gives the model order, p . The criterion, called the final prediction error, FPE, to be minimized is

$$FPE(M) = P_M [N + (M + 1)] / [N - (M + 1)]$$

where P_M is the residual squared error for an M^{th} length filter and N is the length of X . The M for which FPE is a minimum is taken as p . Alternatively, Akaike⁴ suggested minimizing the log likelihood of the innovation variance as a function of filter length to find p . This criterion, called the information theoretic criterion, AIC, is estimated by

$$AIC(M) = \ln (P_M) + 2M/N$$

Again, the M for which AIC is minimized is taken as p . The third method considered here was proposed by Parzen⁵ and is known as the autoregressive transfer function criterion, CAT. The order p is given where the estimate of the difference of the mean square error between the true filter, which exactly gives the innovation, and estimated filter is a minimum. Parzen showed that this difference can be calculated, without explicitly knowing the exact infinite filter, by

$$CAT(M) = \left(\frac{1}{N} \sum_{j=1}^M \hat{P}_j^{-1} \right) - \hat{P}_M^{-1}$$

where

$$\hat{P}_j = N / (N - j) P_j$$

The following examples were generated to compare the method on both auto- and non-autoregressive series. For each example the Burg method¹ was used to determine the A_i 's.

For plotting purposes, noting that $\log \text{FPE}$ asymptotically approaches AIC, we define

$$F(M) = \log_{10} \{ \log_{10} [\text{FPE}(M)] - \log_{10} [\text{FPE}(p)] + 1 \}$$

$$A(M) = \log_{10} [\text{AIC}(M) - \text{AIC}(p) + 1]$$

$$C(M) = \log_{10} [\text{CAT}(M) - \text{CAT}(p) + 1]$$

such that the value of each criterion at the predicted order number, p , is 0.

The first time series considered is one cycle of the complex harmonic $\exp[\sqrt{-1} (2\pi/100) t]$ shown in part (a) of Fig. V-1. Part (b) of the same figure shows the three order criteria, FPE, AIC, and CAT. Each curve has its minimum at the same value, the CAT being much more robust. Using that value for p results in the correct spectrum shown in part (c). Parts (d) and (e) show the order criteria and spectra, respectively, for the real part of the time series and parts (f) and (g), the same for the imaginary part. In each case the same order number is indicated and the corresponding correct spectrum generated. Again, the CAT criterion is more robust even though the behavior is somewhat artificial due to the use of logarithms.

Figure V-2 shows the results for the same time series plus 50 percent uniformly distributed white noise added independently to the real and imaginary parts. Part (a) is the time series, part (b) the order criteria for the complex case, and part (c) the spectrum assuming the predicted order number. Parts (d), (e), and (f) are the order criteria and spectra, based on CAT and AIC and the FPE minimas, respectively, for the real part of the time series. The CAT and AIC gave the same lower value for p but failed to produce the correct spectrum, while the FPE criterion gave the higher value of p and the correct spectrum. The FPE does have a local minimum of almost the same value as the absolute minimum where the AIC and CAT curves had a minimum. In parts (g), (h), (i), and (j), the order criterion and spectra at p , $2p = p$ (at the FPE real value), and $3p$ for the imaginary part of the time series are shown, respectively. In this instance, the predicted value of p was the same for the AIC, FPE, and CAT criteria; however, that value gave a poor spectral estimate. The spectra for a filter length of $3p$ gave the best result.

The second experiment used the Ricker wavelet

$$R(t) = \frac{\partial^2}{\partial t^2} \exp[-\pi(kt)^2]$$

whose power spectrum is

$$R(f) = \left(\frac{2\pi f}{k}\right)^4 \exp\left[-2\pi\left(\frac{f}{k}\right)^2\right]$$

as the time series whose order was to be estimated and corresponding spectrum computed. This function is not autoregressive. The top curves of Fig. V-3 show the three symmetric portions of the wavelet for $k = 1, 2$, and 10 , respectively. The next three curves show the filter length criteria for the corresponding wavelet above. For each wavelet the AIC, FPE, and CAT had the same value, although it increased as the wavelet became compacted. The next set of curves are the exact log and linear spectra and the last set of curves are the log and linear spectra computed using the predicted filter length criteria. In each case acceptable spectra were computed.

To summarize the results, we note that in the case where little noise is present, AIC, FPE, and CAT give an order number that produces an acceptable spectra for both an auto- and a non-autoregressive time series. When the innovation was large, the criteria gave inconsistent results and for the case we examined, larger filter lengths produced the correct spectra.

It should be noted that the criteria for order number are based on minimizing or predicting the innovation and, thus, they produce not what one usually wants to observe (the spectra without the influence of any noise that is present) but a spectra including the effects of noise. In addition, they are influenced by the technique used to get the autoregressive coefficients. We note that using the Burg technique, we obtained a large filter length when $\exp[\sqrt{-1} \omega_0 t]$ can be exactly predicted by the one point prediction error wavelet $\{1, -\exp[\sqrt{-1} \omega_0]\}$. Work is continuing to generalize the observations made in this report.

T. E. Landers

B. APPLICATION OF THE ENERGY-MOMENT TENSOR RELATION TO FINITE DURATION SOURCES

Previously,⁶ we derived an expression relating the total radiated seismic energy from an arbitrary point source mechanism to the moment tensor of the source. This expression is formulated in terms of the free oscillation normal modes of the earth which limits its applicable bandwidth to that of a given normal mode catalog. We showed results for two large earthquakes (Chile, 1960; Alaska, 1964) for each of two source time functions: a step and a ramp increase in applied moment. In this report, we show results from a third source time function, a half-sine-wave increase in applied moment, and discuss the physical implications and limitations on the radiated energy.

The three source time functions are shown in Fig. V-4. The first two are as previously described; the third is the same as that used by Kanamori and Anderson.⁷ From these functions, energy-moment tensor relations may be easily derived for the total radiated energy. These are:

$$E = \frac{1}{2} \sum_n \frac{|M_0 \cdot S_n(\vec{r}_s)|^2}{F_n \omega_n^2} \quad (\text{step})$$

$$E = \frac{1}{2} \sum_n \frac{|M_0 \cdot S_n(\vec{r}_s)|^2}{F_n \omega_n^2} \left(\frac{\sin \frac{\omega_n T}{2}}{\frac{\omega_n T}{2}} \right)^2 \quad (\text{ramp})$$

$$E = \frac{1}{2} \sum_n \frac{|M_0 \cdot S_n(\vec{r}_s)|^2}{F_n \omega_n^2} \left(\frac{\pi^2 \cos \frac{\omega_n T}{2}}{\pi^2 - \omega_n^2 T^2} \right)^2 \quad (\text{half sine wave})$$

where M_0 is the final value of the moment tensor, $S_n(\vec{r}_s)$ is the strain tensor of the n^{th} normal mode evaluated at the source position, F_n is the normalization integral (previously described), ω_n is the angular frequency of the n^{th} normal mode, and T is the source duration.

We present below results for the 1960 Chilean earthquake based on Plafker and Savage's⁸ fault plane solution with a seismic moment of 8.6×10^{29} dyn-cm. These are computed from a normal mode catalog originally supplied to us by Buland and Gilbert⁹ and now extended to provide complete coverage down to a 45-sec period for both poloidal and toroidal modes.

Figures V-5 to -7 show the effect of changing the source time function on the spectral distribution of energy in the toroidal modes. The results are similar for the poloidal modes. These plots are cumulative energy in 0.004 rad/sec intervals of angular frequency. The period range of the plots is from 18,000 sec at the left-hand side to 45 sec at the right-hand side. This was chosen to encompass the limits of our normal mode catalog.

The results in these figures show that the step function source produces an energy spectrum which continues to increase as $\omega^{1.85}$ at short periods. This is clearly impossible because it implies an infinite radiated energy. The ramp function source results decrease as $\omega^{-0.32}$ at short periods which, although they are certainly preferable to those of the step function source, still fail to guarantee a finite radiated energy. Only the third source time function, a half-sine-wave increase, produces an energy spectrum which is convergent. The drop-off in radiated energy varies as $\omega^{-2.6}$ for this source. We must therefore reject the step and ramp source time functions as physically unrealizable because of their asymptotic behavior at short periods.

Because of the difficulties of measuring the amplitude decay of spectra from their envelopes, particularly when the bandwidth is as limited as ours, we cannot give any certainty to the values of the exponents given above. Experience suggests the fractional error in the slope of a line measured off a graph to be bounded by twice the largest fractional error in the ordinates. If this is true, then we expect the values of the exponents to be accurate to within 10 percent. Thus, we cannot say for sure whether the exponent for the step function frequency dependence, 1.85, precludes a frequency squared behavior. On the other hand, the half-sine-wave source, dropping off in frequency with a measured exponent of 2.6 seems to rule out either frequency squared or frequency cubed behavior.

The dependence of the radiated energy on the source duration for the half-sine-wave source time function is shown in Fig. V-8. As can be seen, there is a dramatic decrease in the total radiated energy on the order of a factor of 400 between 0- and 200-sec source duration. Furthermore, this decrease is logarithmically nonlinear; dropping off most rapidly at short source durations. The relative distribution of radiated energy into poloidal and toroidal components is also dependent on source duration. At short durations, the poloidal component dominates; at long durations, the radiated energy approaches equipartition between poloidal and toroidal components.

It is apparent from the energy-moment tensor relation that the partition of energy between the toroidals and poloidals will depend on the fault plane solution and the source depth. Since we have studied⁶ only large thrust events at shallow depths (i.e., Alaska, 1964 and Chile, 1960), our results cannot be extended to deep events of different mechanisms without modification.

We feel the physical significance of this phenomenon lies in the nature of the forces resisting the earthquake faulting process. Short source duration (i.e., rapid release of tectonic stress) implies there are low frictional or deformational forces resisting the rupture formation. Thus, relatively little energy is expended in overcoming those resisting forces. Long source duration implies the opposite: that the resisting forces are large and therefore consume much of the tectonic strain energy available to produce the rupture. In the former case, the seismic efficiency is high. In the latter case, it is low because the bulk of the energy is wasted in non-seismic processes. The results of Fig. V-8 show the extent of this variation which, for our model, spans almost 2 surface wave magnitude units.

D. W. McCowan
A. M. Dziewonski

C. CONTRIBUTION OF LARGE EARTHQUAKES TO EXCITATION OF POLAR MOTION FOR YEARS 1901 TO 1970

Since its discovery in 1891, the Eulerian free nutation of the earth (properly called the Chandler wobble) has been of considerable interest to astronomers, meteorologists, oceanographers, and solid-earth geophysicists. Throughout this time, the mechanisms exciting the wobble have remained elusive, and although atmospheric motions, core-mantle interactions and earthquakes have all been considered, none of these has been either clearly identified as the principal source of excitation or entirely rejected as a partial contributor.

In this report, we consider the cumulative effect of major earthquakes that occurred between 1901 and 1970 as a source of excitation of the wobble. Previous investigations of the role of earthquakes in exciting the wobble have yielded no clear conclusions. Although Munk and MacDonald,¹⁰ among others, had concluded that displacements associated with earthquakes were too small to excite the wobble, Smylie and Mansinha¹¹ presented evidence for a correlation between times of occurrence of major earthquakes and changes in the direction of polar motion. This suggested that earthquakes could be responsible for a sizable fraction of the excitation and revived interest in the subject which has become one of the more controversial topics in the geophysical literature.

Subsequent studies^{12,13} concentrated on the correlation between individual earthquakes and short-term changes in polar motion. Because of the considerable uncertainty in the exact location of the pole at any time, a definite correlation between polar motion and earthquakes could not be firmly established.^{14,15} In addition, Dahlen¹⁶ concluded that earthquakes could not account for the observed amplitude of the wobble.

Nevertheless, there is still highly suggestive evidence of a correlation between global seismicity and changes in the amplitude of the wobble over the period of the last 70 years.¹⁷⁻¹⁹ This suggests that the cumulative effect of earthquakes may account for long-term variations in the amplitudes of the wobble, even though the effect of any individual earthquake is too small to be detected above the noise in the polar motion data. In order to investigate this possibility, we calculate the polar motion expected from major earthquakes over the last 70 years and compare it with actual polar motion data over the same period. This requires specification of the time, location, and source parameters of the earthquakes, as well as the calculation of the change of the earth's inertia tensor caused by an earthquake.

In our previous report,²⁰ we have described a method of calculation of the polar shift from an earthquake of known location, source mechanism, and seismic moment. We also have demonstrated how the knowledge of relative motions of plates can be used to infer the geometry of a fault plane solution of an earthquake occurring at a particular type of the boundary between two plates.

The 234 earthquakes with magnitudes $M_s \geq 7.8$ used to calculate the excitation of the Chandler wobble are taken from the catalog compiled by Duda²¹ and supplemented by information from the Bulletin of the Seismological Society of America for the years 1965-1970. Since it is the seismic moment M_0 that determines the static displacement, we have used an approximate empirical relation to determine the moments from the reported magnitudes. Figure V-9, after Chinnery and North,²² shows the relation between M_0 and M_s for a number of earthquakes for which both have been independently determined. The solid line is the relation between moment and magnitude proposed by Chinnery and North. The dashed line shows the relation we have used to determine the moments; it obviously is a reasonable approximation to the data for magnitudes greater than 7.5. The remaining source parameters were determined from the

TABLE V-1
TIMES AND LOCATIONS OF THE 30 LARGEST EARTHQUAKES
CONTRIBUTING TO THE EXCITATION OF THE CHANDLER WOBBLE†

Na.	Year	Month	Day	Latitude	Longitude	Depth (km)	Magnitude	Shift (0.01 in.)	Direction (°E)	ΔLOD (μsec)
1	1901	Aug.	9	-22.0	170.0	s	8.4	0.60	336.2	-7.02
2	1902	Sept.	23	16.0	-93.0	s	8.4	0.49	296.3	-5.83
3	1905	Apr.	4	33.0	76.0	s	8.6	1.62	89.4	-2.60
4	1906	Jan.	21	34.0	138.0	340	8.4	0.83	101.4	1.84
5	1906	Jan.	31	1.0	-81.5	s	8.9	1.39	218.0	-160.17
6	1906	Aug.	17	-33.0	-72.0	s	8.6	2.56	108.0	-16.09
7	1906	Sept.	14	-7.0	149.0	s	8.4	0.79	239.0	-0.03
8	1910	June	16	-19.0	169.5	100	8.6	1.78	340.7	-26.53
9	1911	June	15	29.0	129.0	160	8.7	4.86	105.7	-17.96
10	1914	Nov.	24	22.0	143.0	110	8.7	3.07	160.6	-43.10
11	1917	May	1	-29.0	-177.0	60	8.6	2.33	9.0	-18.26
12	1917	June	26	-15.5	-173.0	s	8.7	4.33	277.3	-0.69
13	1919	Apr.	30	-19.0	-172.5	s	8.4	0.55	19.6	-8.13
14	1922	Nov.	11	-28.5	-70.0	s	8.4	0.72	110.8	-6.15
15	1923	Feb.	3	54.0	161.0	s	8.4	0.71	146.1	2.07
16	1929	Mar.	7	51.0	-170.0	60	8.6	2.10	171.9	6.95
17	1934	Jan.	15	26.5	86.5	s	8.4	0.53	95.3	-3.40
18	1938	Nov.	10	55.5	-158.0	s	8.7	3.89	189.1	17.54
19	1939	Dec.	21	0.0	123.0	150	8.6	0.84	106.7	-4.36
20	1940	May	24	-10.5	-77.0	60	8.4	0.33	73.9	-8.76
21	1941	June	26	12.5	92.5	60	8.7	4.30	178.4	-13.57
22	1941	Nov.	25	37.5	-18.5	s	8.4	0.53	323.6	-0.27
23	1942	Aug.	24	-15.0	-76.0	60	8.6	1.30	75.6	-22.71
24	1946	Dec.	20	32.5	134.5	s	8.4	0.77	116.8	-3.20
25	1950	Aug.	15	28.5	96.5	s	8.7	2.86	122.3	-11.83
26	1952	Mar.	4	42.5	143.0	s	8.6	2.77	131.2	-5.00
27	1952	Nov.	4	52.8	159.5	s	8.4	0.82	147.2	1.69
28	1958	Nov.	6	44.5	148.5	75	8.7	4.50	130.4	-2.47
29	1960	May	22	-39.5	-74.5	s	8.6	2.56	109.2	-9.80
30	1964	Mar.	28	61.1	-147.6	20	8.5	1.11	202.7	7.92

†The magnitude and direction of the pole shift as well as the change in length of day from each earthquake is shown. Depths designed s were assigned a standard value of 33 km. Earth model PEM-A (Ref. 24) was used to calculate the pole shifts.

plate tectonic model using the data of Solomon *et al.*²³ for the positions of the boundaries and relative motions of plates.

The calculated pole shift (in 0".01) and direction (degrees east of Greenwich) are given in Table V-1 for the 30 largest earthquakes of those considered. Also shown is the change in length of day (ΔLOD , in microseconds) resulting from the change in the polar moment of inertia of the earth.

From the calculated pole shifts, we can compute a synthetic polar wobble curve that would result from this source of excitation alone. For this, we also require the starting position $m(t_0)$ of the pole in January 1901 and the frequency ω_0 and damping Q of the Chandler wobble.

The synthetic wobble $m(t)$ is computed from:

$$m(t) = m(t_0) \exp[i\omega(t - t_0)] + \sum_k s_k H(t - t_k) \cdot \left\{ 1 - \left(1 + \frac{\omega_0}{\Omega} \right) \exp[i\omega(t - t_k)] \right\}$$

where ω is the complex circular frequency of the Chandler wobble: $\omega = \omega_0(1 + i/2Q)$, s_k are the complex pole shifts due to earthquakes at times t_k , Ω is the frequency of the diurnal rotation and H is the unit step function. The complex function $m(t)$ is referred to the coordinate system in which the real axis corresponds to the Greenwich meridian and the imaginary axis points toward 90°E .

Figure V-10 shows the real part (m_x) of three such synthetic wobble curves obtained using $\omega_0 = 5.287$ rad/yr after Wilson²⁵ and three different values of Q . Shown for comparison is a smoothed version of the International Latitude Service (ILS) polar motion data, with the annual term removed, also from Wilson.²⁵ The initial pole location is the same for all curves, and each curve has been bandpass filtered from 0.3 to 0.98 cycles/yr to facilitate comparison. The ticks on the top of the figure mark the times of the earthquakes in Table V-1.

The general trend of the amplitude of the wobble can be seen in the ILS data. The observed amplitude was large in 1910, decreased fairly uniformly from 1910 to 1920, and remained small until 1940 when it began to increase again to reach the maximum value by 1954. Since then, there has been an irregular decline in amplitude. The synthetic wobble time series, particularly for $Q = 100$, reproduce the principal features of these amplitude changes. The decrease in the synthetic wobble is due to the cumulative effect of several large earthquakes from 1914 to 1929. This occurs even for the case with $Q = 10,000$ and it is thus apparent that earthquakes can reduce the amplitude of the wobble and a rapid decay of amplitude need not be attributed to intrinsic dissipation. Similarly, the increase in the synthetic wobble amplitude is due to large earthquakes from 1938 through 1950 which gradually re-excite the wobble. We should note that the decline in amplitude observed since 1954 is not reproduced in the synthetic wobble curves; this may be an effect of other sources of excitation.

The results of this study indicate that the cumulative effects of major earthquakes can account for at least a large part of the excitation of the Chandler wobble and, in particular, for the long-term variations of the amplitude of the wobble. This, together with recent estimates of the atmospheric excitation of the wobble,²⁵ indicates that these two mechanisms may well account for the entire excitation. If this is verified by more detailed analysis, it should permit more accurate determination of the period and damping of the wobble, and of the effective elastic properties of the earth at very long periods.

R. J. O'Connell†
A. M. Dziewonski

† Department of Geological Sciences, Harvard University, Cambridge, MA 02138.

REFERENCES

1. T. J. Ulrych and T. N. Bishop, "Maximum Entropy Spectral Analysis and Autoregressive Decomposition," *Rev. Geophys. Space Phys.* **13**, No. 1, 183-200 (1975).
2. T. J. Ulrych and R. W. Clayton, "Time Series Modeling and Maximum Entropy," unpublished manuscript, Department of Geophysics and Astronomy, University of British Columbia (1975).
3. H. Akaike, "Fitting Autoregressive Models for Prediction," *Ann. Inst. Statist. Math.* **24**, 243-246 (1969).
4. H. Akaike, "A New Look at Statistical Model Identification," *IEEE Trans. Auto. Control* **AC-19**, No. 6, 716-723 (1974).
5. E. Parzen, "Multiple Time Series: Determining the Order of Approximating Autoregressive Schemes," *Statistical Sciences*, Report No. 23, Department of Computer Science, State University of New York at Buffalo (July 1975), 24 pages.
6. D. W. McCowan and A. M. Dziewonski, "Toward a Moment Tensor-Energy Relation," *Seismic Discrimination SATS*, Lincoln Laboratory, M.I.T. (31 December 1975), DDC AD-A025777.
7. H. Kanamori and D. L. Anderson, "Amplitude of the Earth's Free Oscillations and Long-period Characteristics of the Earthquake Source," *J. Geophys. Res.* **80**, 1075-1078 (1975).
8. G. Plafker and J. C. Savage, "Mechanism of the Chilean Earthquakes of May 21 and May 22, 1960," *Geol. Soc. Am. Bull.* **81**, 1001-1030 (1970).
9. R. P. Buland and F. Gilbert, "The Theoretical Basis for the Rapid and Accurate Computation of Normal Mode Eigenfrequencies and Eigenfunctions" (unpublished note, 1975).
10. W. H. Munk and G. J. F. MacDonald, The Rotation of the Earth (Cambridge University Press, 1960).
11. D. E. Smylie and L. Mansinha, "Earthquakes and the Observed Motion of the Rotation Pole," *J. Geophys. Res.* **73**, 7661-7663 (1968).
12. D. E. Smylie, G. K. C. Clarke, and L. Mansinha, "Deconvolution of the Pole Path," in Earthquake Displacement Fields and the Rotation of the Earth, L. Mansinha, D. E. Smylie, and A. E. Beck, Eds. (D. Reidel Publishing Co., Dordrecht, Holland, 1970), pp. 99-112.
13. L. Mansinha and D. E. Smylie, "Seismic Excitation of the Chandler Wobble," in Earthquake Displacement Fields and the Rotation of the Earth, L. Mansinha, D. E. Smylie, and A. E. Beck, Eds. (D. Reidel Publishing Co., Dordrecht, Holland, 1970), pp. 122-135.
14. R. A. Haubrich, "An Examination of the Data Relating Pole Motion to Earthquakes," in Earthquake Displacement Fields and the Rotation of the Earth, L. Mansinha, D. E. Smylie, and A. E. Beck, Eds. (D. Reidel Publishing Co., Dordrecht, Holland, 1970), pp. 149-158.
15. F. J. Wells, "On Separation of the Annual and Chandler Spectral Components in Astronomic Latitude and Polar Motion Data," Ph. D. Thesis, Brown University (1972).
16. F. A. Dahlen, "A Correction to the Excitation of the Chandler Wobble by Earthquakes," *Geophys. J. R. Astr. Soc.* **32**, 203-217 (1973).
17. R. J. Myerson, "Evidence for Association of Earthquakes with the Chandler Wobble, Using Long Term Polar Data of the ILS-IPMS," in Earthquake Displacement Fields and the Rotation of the Earth, L. Mansinha, D. E. Smylie, and A. E. Beck, Eds. (D. Reidel Publishing Co., Dordrecht, Holland, 1970), pp. 159-168.
18. D. L. Anderson, "Earthquakes and the Rotation of the Earth," *Science* **186**, 49-51 (1974).
19. F. Press and P. Briggs, "Chandler Wobble, Earthquakes, Rotation and Geomagnetic Changes," *Nature* **256**, 270-273 (1975).

20. A. M. Dziewonski and R. J. O'Connell, Seismic Discrimination SATS, Lincoln Laboratory, M.I.T. (31 December 1975), DDC AD-A025777.
21. S. J. Duda, "Secular Seismic Energy Release in the Circum-Pacific Belt," *Tectonophysics* 2, 409-452 (1965).
22. M. A. Chinnery and R. G. North, "The Frequency of Very Large Earthquakes," *Science* 190, 1197-1198 (1975).
23. S. C. Solomon, N. H. Sleep, and R. M. Richardson, "On the Forces Driving Plate Tectonics: Inferences from Absolute Plate Velocities and Intraplate Stress," *Geophys. J. R. Astr. Soc.* 42, 769-801 (1975).
24. A. M. Dziewonski, A. L. Hales, and E. R. Lapwood, "Parametrically Simple Earth Models Consistent with Geophysical Data," *Phys. Earth Planet. Inter.* 10, 12-48 (1975).
25. C. R. Wilson, "Meteorological Excitation of the Earth's Wobble," Ph. D. Thesis, University of California, San Diego (1975).

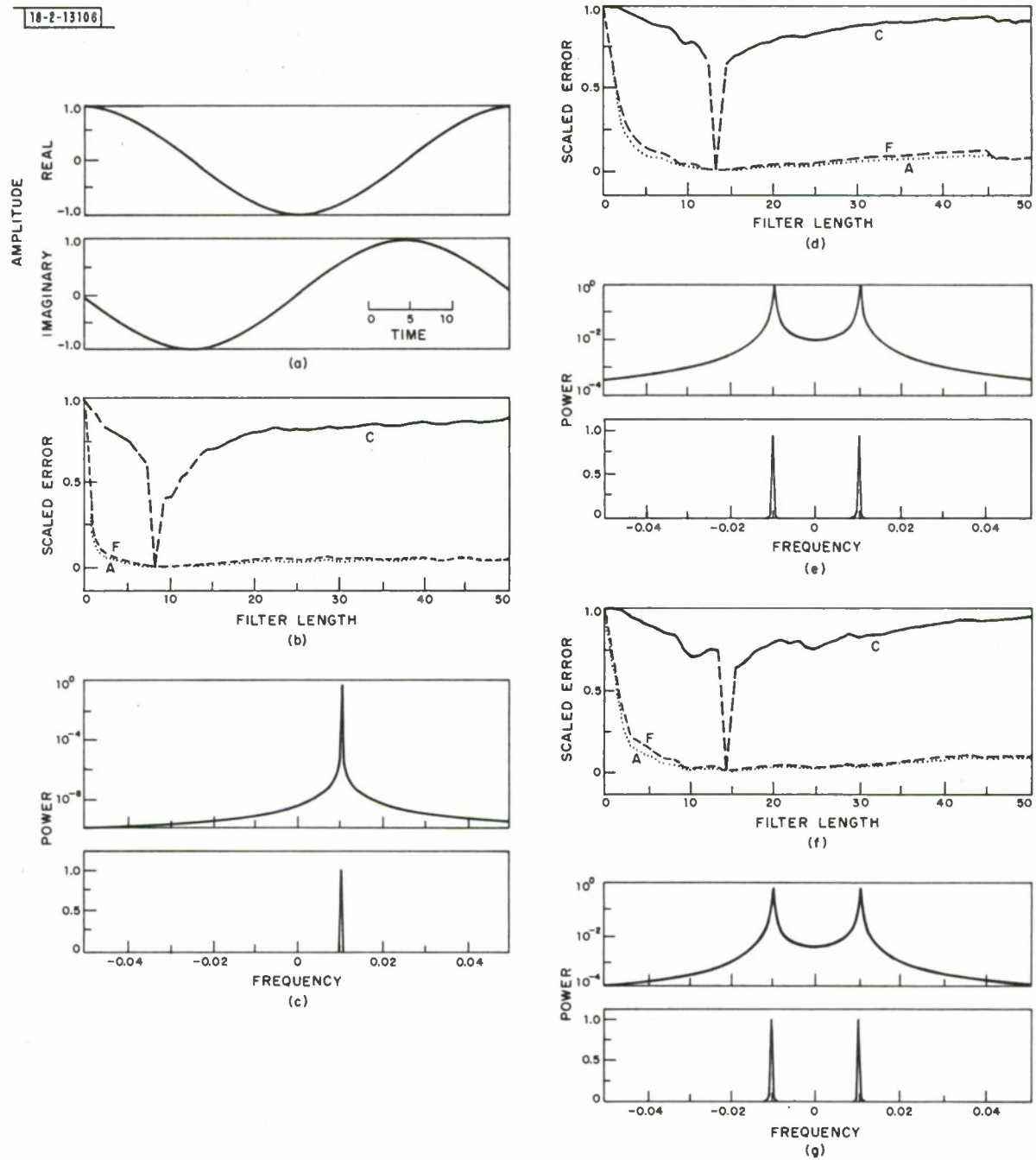


Fig. V-1. Error analysis for one cycle of a complex harmonic: (a) Complex harmonic $\exp[\sqrt{-1}(2\pi/100)t]$; (b) AIC, CAT, and FPE for (a); (c) spectrum at minimum in (b); (d) AIC, CAT, and FPE for real part of (a); (e) spectrum at minimum in (d); (f) AIC, CAT, and FPE for imaginary part of (a); and (g) spectrum at minimum in (f).

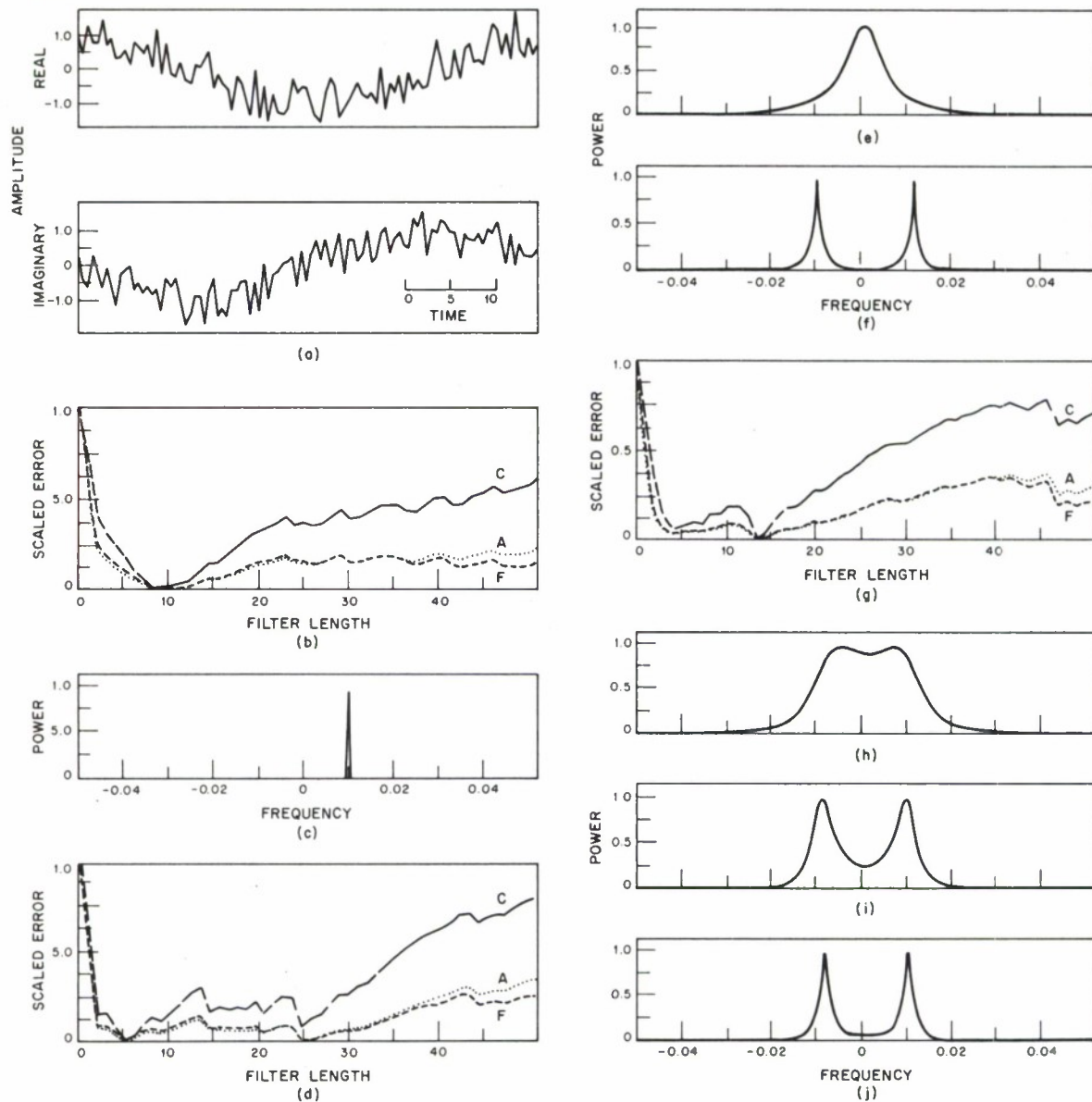


Fig. V-2. Error analysis for one cycle of a complex harmonic with white noise: (a) Complex harmonic $\exp[\sqrt{-1}(2\pi/100)t]$ plus 50 percent noise; (b) AIC, CAT, and FPE for (a); (c) spectrum for minimum in (b); (d) AIC, CAT, and FPE for real part of (a); (e) spectrum for minimum given by AIC and CAT in (d); (f) spectrum for minimum given by FPE in (d); (g) AIC, CAT, and FPE for imaginary part of (a); (h) spectrum for minimum in (g); (i) spectrum for twice minimum in (g); and (j) spectrum for three times minimum in (g).

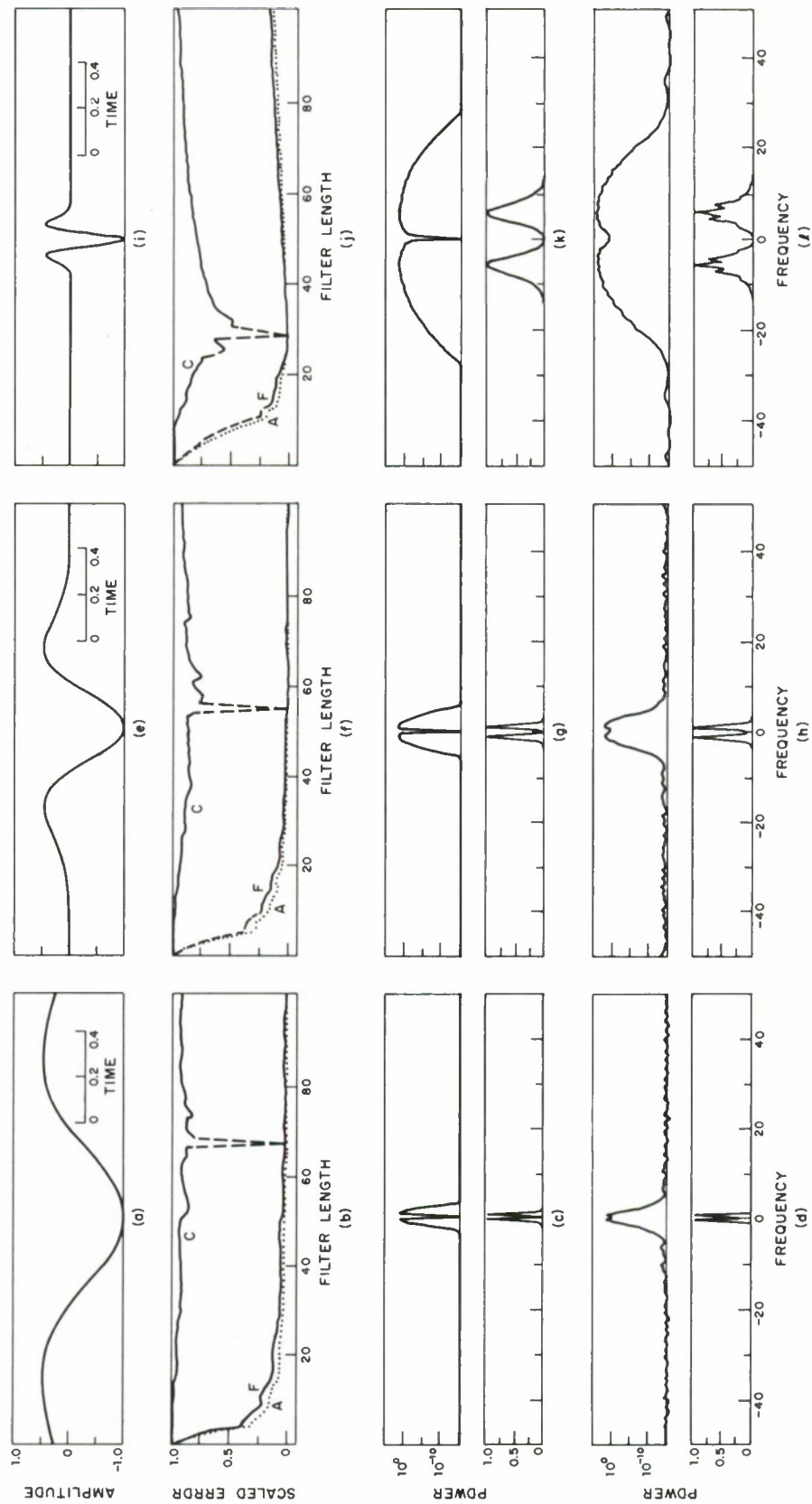


Fig. V-3. Error analysis for the non-autoregressive Ricker wavelet: (a) Ricker wavelet $k = 1$; (b) AIC, FPE, and CAT for (a); (c) exact spectrum of (a); (d) spectrum of (a) based on minimum in (b); (e), (f), (g), and (h) same as (a-d) for $k = 2$; and (i), (j), (k), and (l) same as (a-d) for $k = 10$.

Fig. V-4. Three different source time functions.

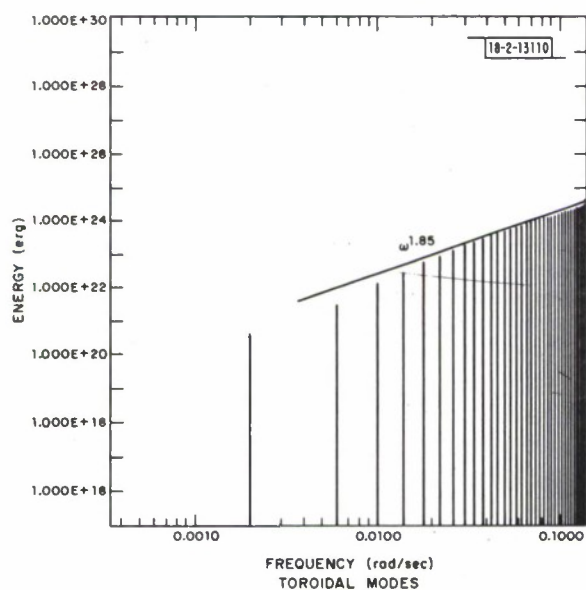
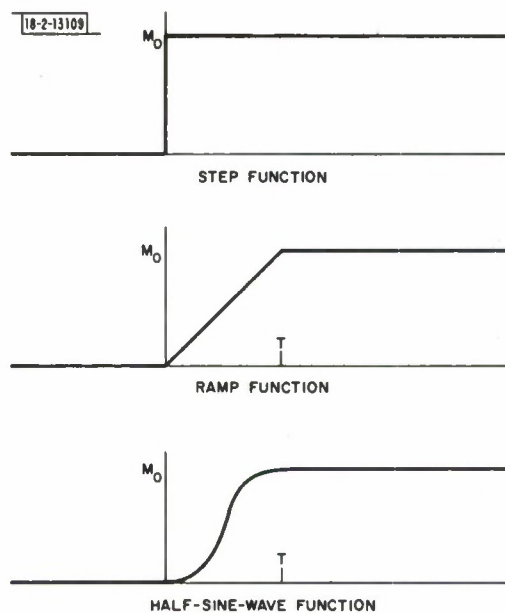


Fig. V-5. Spectral distribution of radiated energy for a step source time function of applied moment. Results for the 1960 Chilean earthquake using Plafker and Savage's (1970) fault-plane solution. 180-sec source at 79.4 km depth.

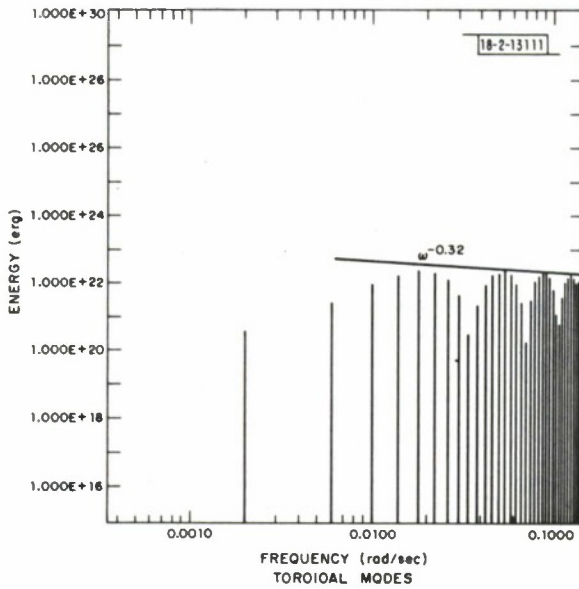


Fig. V-6. Spectral distribution of radiated energy for a ramp source time function of applied moment. Results for the 1960 Chilean earthquake using Plafker and Savage's (1970) fault-plane solution. 180-sec source at 79.4 km depth.

Fig. V-7. Spectral distribution of radiated energy for a half-sine-wave source time function of applied moment. Results for the 1960 Chilean earthquake using Plafker and Savage's (1970) fault-plane solution. 180-sec source at 79.4 km depth.

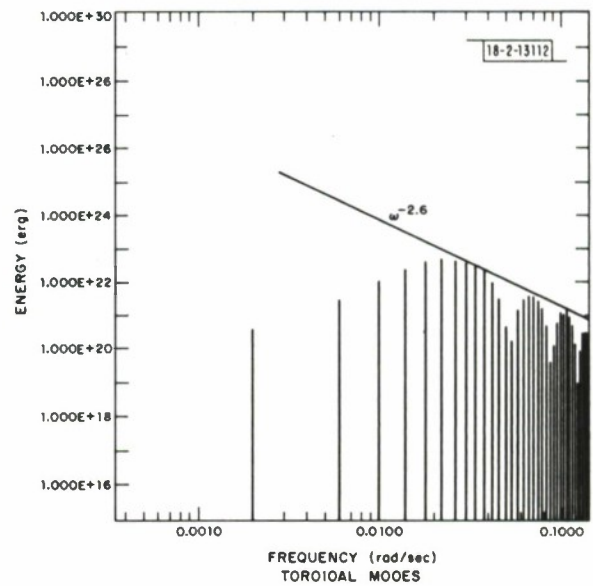


Fig. V-8. Energy as a function of source duration for the half-sine-wave source time function. Results for the 1970 Chilean earthquake using Plafker and Savage's (1970) fault-plane solution. Source at 79.4 km depth. Magnitude from Gutenberg-Richter relation.

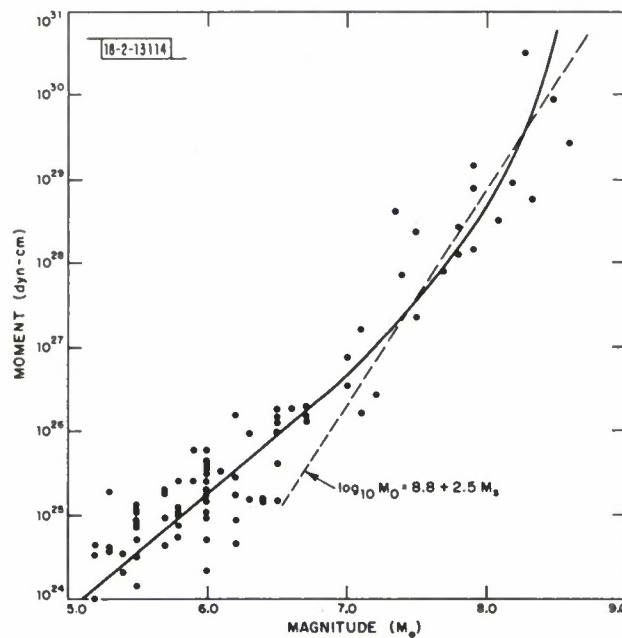
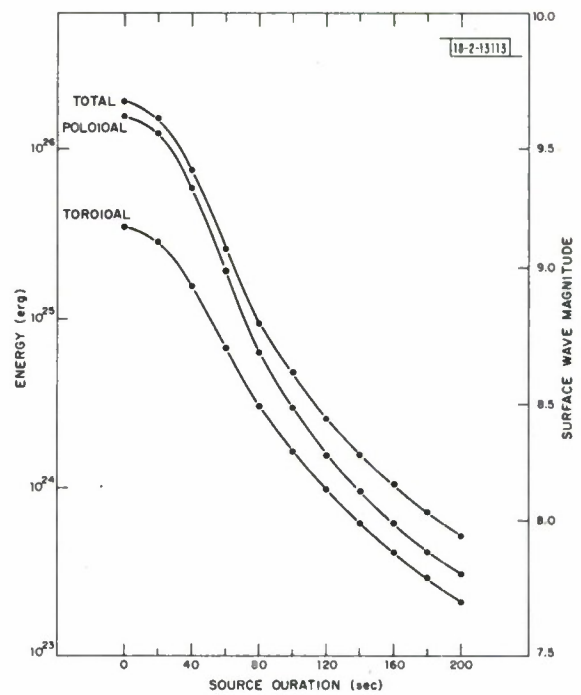


Fig. V-9. Relation between seismic moment M_0 and magnitude M_s after Chinnery and North.²² The dashed line gives the relation used to calculate the pole shifts from earthquakes.

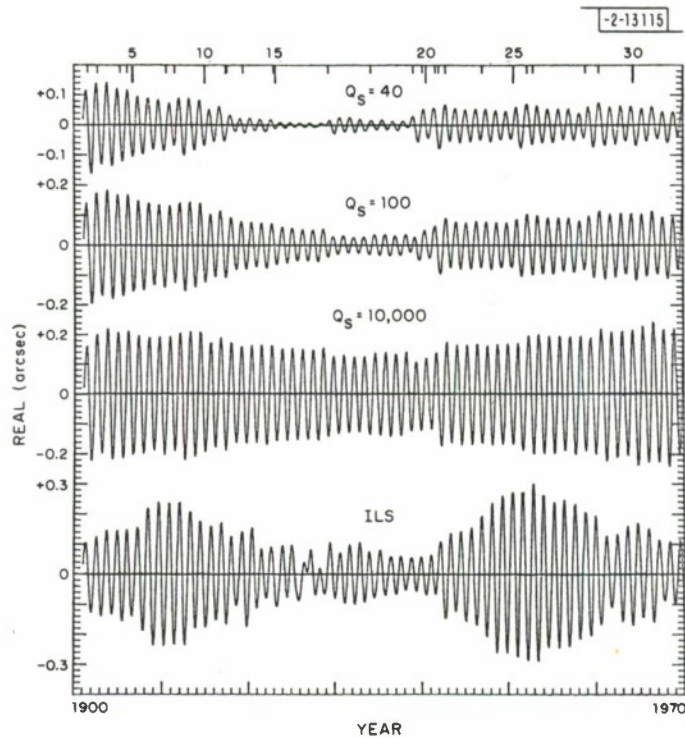


Fig. V-10. Simulated polar motion curves resulting from excitation by large earthquakes; the damping for each is determined by Q_s . ILS is smoothed observed polar motion with anneal term removed.²⁴ Only the component along the Greenwich meridian is shown.

VI. DATA SYSTEMS

A. SEISMIC DATA AND INFORMATION SYSTEM

A seismic information and data system has been under design and development for the last year and a half. The progress in implementing the system has been described in several of the more recent Semiannual Technical Summaries issued during that period. This present report will be a project milestone in that it will mark both the end of the development phase of the system and the beginning of the information distribution phase. A complete report describing the project is in preparation and should be ready for distribution during the third quarter of 1976. What is presented in this short report is a general overview of the system and the various files that make up the directory (IWWSS) at ISIC on the ARPANET.

There are two reasons for developing such a seismic data and information system, and both reasons are equally important for the development of this data base. One reason was the complexity of the seismic research observatory program combined with the previously installed large seismic arrays and the high-gain long-period installations. These seismic systems combined to produce a highly sophisticated system of digital recording seismic stations. This system needed a logically structured description that could be made available to users of the data generated by this seismic network. A second reason was the development of a sophisticated text editing and management system called NLS (on-Line System) developed by the Augmentation Research Center of Stanford Research Institute. This system was made available over the ARPANET to a very diverse community of users. NLS was to provide the basic tool necessary to build the data base.

The Seismic Data and Information System (SDIS) is an information data base that describes in detail the Seismic Research Observatory (SRO) program development and the high-gain long-period program. The older large seismic arrays are also covered; however, not in such detail as are the newer components of the seismic network. Additional information is contained in the SDIS describing the mass storage device, i.e., datacomputer, that is available on the ARPANET. The datacomputer will serve as the actual on-line depository for much of the raw and processed seismic data generated by the SRO and HGLP programs.

As of this writing, not all components of this integrated seismic system are complete. For example, the actual format descriptions for all the data files which will exist in the datacomputer are not yet available. Descriptions of the network event processor, command and control processor, and the seismic information processor are also not yet available. Apart from these items, the SDIS contains a detailed description of all the major components in the SRO and HGLP programs.

A directory has been established on the ARPANET host computer located at ISIC, network address number 150, which contains all the files of the SDIS. The Tenex protection for each file has been set to allow any user who is logged in at ISIC to have read access to these files. This will enable a user to read or copy any file in the directory (IWWSS) but not allow him to change the files in any way. Files within the directory (IWWSS) can be copied from the directory to any other host on the ARPANET by means of the FTP programs located at each site. Network users cannot log into the directory (IWWSS) but are otherwise free to access the information stored there.

The files within the directory do vary in size from a few pages to nearly 100 pages. The files which reflect the current status of the data are short files but will grow as the seismic system matures. The data status and site status files contain information that has been taken from a directory that is maintained by the Albuquerque Seismological Laboratory. As this directory is updated, data will also be incorporated into the (IWWSS) directory.

A brief description of each of the major files is given below. Persons with ARPANET access are encouraged to look into the (IWWSS) directory. Persons without ARPANET access can address a request to the author.

List of Files Within the Directory (IWWSS)

Summary-Overview

List and descriptions of available files. This list is taken from the Summary-Overview file.

Introduction

This file contains an introduction to the documents available in the directory (IWWSS). Also covered is a brief description of the components of the Integrated World Wide Seismic System.

Index

A copy of the index from each file is contained here. It provides a good starting point to determine what document is appropriate for one's needs.

Contacts/People

People and groups associated with the IWWSS program. Indicates who to contact for what kind of information.

Datacomputer-Datafile-Structure

This file gives proper data-language descriptions of all seismic files in the datacomputer and detailed English language descriptions of the contents of these files. When coupled with a proper users manual for data-language, this file contains all information needed by a user to allow him to write programs to retrieve data from the datacomputers. This file is not yet implemented.

Datacomputer-Version-1

This file contains the programming manual for the datacomputer. When used in combination with the seismic data file, specifications will allow users to obtain access to data stored in the datacomputer.

HGLP-Calibrations

The most recent calibrations for the various high-gain long-period sites are contained in this file. Older calibrations also will be available in this file for historical purposes.

HGLP-General-Description

General descriptions of the high-gain long-period instrumentation, seismometer, tape recorders, and filters are available in this file.

HGLP-Site-Descriptions

Specific site descriptions and installation reports are available in this file. The exact site coordinates, site geology, and descriptions of the installation conditions can be found within this file.

SRO and HGLP-Data-Status

For each seismic site, this file lists when it became operational, when major changes in operation or configuration occurred, and what raw data are available from the IWWSS mass store and from the original data tapes.

SRO-Calibrations

The calibrations performed at the time of installation and at any time thereafter are listed in this file.

SRO-Hardware and Software

The descriptions of the general components of the SRO installations are contained within this file. Those elements which are common to all SROs will be described here. Items such as the seismometer, filters, computer, tape drives, etc., are described in detail.

SRO-Site-Descriptions

The actual installation reports are contained in this file. As the report becomes available it will be included. Items covered include site coordinates, site geology, and installation conditions.

Seismic-Arrays

Brief descriptions of the large seismic arrays, LASA, NORSAR, ALPA, and ILPA are contained in this file. The actual seismometer coordinates also can be found here.

SIP

Describes the configuration and functions of the Seismic Information Processor (SIP), its protocols and formats for communication with the CCP and the main datacomputer; actual operational procedures including actions of the datacomputer, the SIP, the ARPANET, the CCP, or the loss of any data streams into the CCP. This file is not yet implemented.

CCP

Describes the configuration and the Control and Communication Processor; its protocol and formats for communication with the SIP, sites attached via the

ARPANET, sites attached by private lines, and the SDAC IBM 360 computers; operational procedures including action taken for all failure conditions. This file is not yet implemented.

NEP

Functionally describes Network Event Processor and its relation to the data-computer and CCP in detail. This includes description algorithms and heuristics, and time scale and sequence for functions performed. Interactions between NEIS, NEP, datacomputer, and CCP are included in detail. This file is not yet implemented.

R. M. Sheppard

B. MULTI-AZIMUTH LARGE ARRAY LONG-PERIOD DATA BASE

Several ongoing studies require a multi-event data base consisting of long-period array recordings. Among these seismological experiments are: (1) a study to determine the degree of structural and mineralogical velocity anisotropy in the crust and upper mantle beneath ALPA, NORSAR, and LASA, (2) a study to determine the angular difference between phase and group wavefronts for Love and Rayleigh waves propagating across inhomogeneous media, (3) a study to quantize the deviation in azimuth of surface waves from great circle routes and to invert such data into path corrections for the purpose of more uniform long-period magnitudes and source characteristics, and (4) a study to compare the S-wave velocity structure differences obtained by the independent inversion of Love and Rayleigh wave dispersion data at each of the large arrays. To these ends an appropriate data base has been edited out of the existing ASG seismic library, restored to its original quality, and saved in a multiframe FFASTRO format.

The data format is as follows: for each event, the long-period recordings of both the vertical and horizontal components of each subarray triax are retained. The time increment spans from several minutes before the long-period P-wave arrival to several tens of minutes after the high-frequency tails of the Love and Rayleigh waves. For each of the long-period arrays at LASA, ALPA, and NORSAR, 18 source events were selected such that each 20° arc of azimuth for each array contains the great circle back azimuth of one of the events. The source events for each array were necessarily unique since the allowable depth, distance, and magnitude of an event were restrained as follows: (1) the event distance from the array must be equal to or less than 90°, (2) the event depth must be less than or equal to 60 km, and (3) the event magnitude must be equal to or greater than 5.0 m_b . These limitations insure good signal-to-noise ratios over the complete long-period band. The geographic distribution for the events for the NORSAR array and the ALPA array are shown in Figs. VI-1 and -2, respectively. Each plot is an equiazimuthal equidistance projection centered on the appropriate array. The LASA data set is near completion.

R. E. Needham
T. E. Landers

C. SRO DATA TAPE PROCESSING FACILITY

A plan for PDP-7 Console expansion and other software required to effectively handle SRO data tapes was described in a previous SATS.¹ This system has been completely implemented and is now in operation. The last SATS² discussed the first parts to be completed; the final programs that were added to the system were these:

(1) SROSP, SROLP, SRO26

These programs run on our PDP-11 and convert 9-track SRO raw data tapes to 7-track tapes in the new Data Unit format described in Ref. 1. This format's advantage over the SRO format is that it includes more descriptive information (such as instrument gain and orientation) as alphanumeric data on the tape itself.

(2) Two new PDP-7 programs to allow these Data Unit tapes to be used as input to the Analysis Console system:

(a) DUINIT (previously called >TAB)

This program allows the user to select the data to be viewed by typing in an event time and location. DUINIT will compute the theoretical arrival time at each selected SRO station and will set up a table of arrival times to pass to >DUI.

(b) >DUI

>DUI actually searches the Data Unit tape for segments of data that match the stations, times, and orientations specified in the table set up by DUINIT. When matching data are found, >DUI reads them in and initializes the Analysis Console appropriately.

As SRO tapes have been received we have been converting them to Data Unit tapes on the PDP-11 and then merging the tapes from various stations using the PDP-7 DUM program. We now have merged tapes available for use starting with 28 December 1975.

One more software improvement is being designed: An Analysis Console plot program which will plot all the data contained in an Analysis Console session, complete with alphanumeric descriptive information. (Currently we can only get hard copy of the part of the data segment that can be displayed on the scope at any one time.)

L. J. Turek
M. F. O'Brien

D. PDP-11 SOFTWARE

An analysis of the computer usage of Group 22 has led to a reorganization of the PDP-11 based computer systems. The analysis showed that the group has a variety of data-processing requirements. These include interactive usage such as editing programs and document preparation, batch processing for CPU-bound programs, both hard and soft copy computer graphics, the maintenance and manipulation of a large seismic data base, and access to the ARPANET. All the above-mentioned processing requirements are now being performed on a number of machines with a variety of foreign host computers on the ARPANET accessed through a USER TELNET running on our PDP-11 systems. Data are transferred to and from our site using a primitive FTP program on the PDP-11 system and through the use of the shuttle service between Group 22 and the Lincoln IBM 370/168.

The dispersal of these functions on the various machines and the quality of data transfer connections between the systems create a number of problems for the user. Interactive response time is significantly slower over the ARPANET than with a direct machine connection; there is a lack of adequate network file transfer capability; the probability of a system failure is increased because the user must go through a number of computers to do his processing;

the user is faced with learning the intricacies of a number of computer systems; and, finally, the local PDP-11 computers are greatly underutilized. Because of these problems, it was felt that the centralization of most of the processing tasks in the Group 22 computers would be desirable. Only extremely large CPU-bound programs and the large seismic data bases would remain on foreign host computers.

The development of system software to handle all these processing tasks would be quite expensive and time consuming. It was therefore decided to purchase an existing PDP-11 operating system and modify it for our needs. The system chosen was UNIX developed by Bell Telephone Laboratories.³ It was chosen because it is an extremely well designed and proven operating system and contains a large amount of the required software.

With UNIX as a base it will be possible to build the other parts of the desired system. It will provide a software development environment far superior to that which we have previously had. All the standard features of a time-sharing system, including document preparation facilities, already exist under UNIX. The ARPANET software for UNIX is available from the University of Illinois. An extremely sophisticated interactive graphics package already exists under UNIX at the University of Toronto. While this system is more sophisticated than anything we require, it can be used as a basis for building a more modest graphics package.

A major problem which must be solved is the efficient use of computer resources to handle the variety of processing tasks. It is difficult to build a time-sharing system which runs both interactive and CPU-bound programs efficiently. Most systems which have to run both kinds of programs give scheduling priority to the interactive programs at the expense of the CPU-bound jobs. A better solution for Group 22 will be a dual CPU system. One CPU will be used for all the interactive programs, while the other will be run in batch mode for CPU-bound programs. The machines will be linked together through a data channel and through a common disk system (Fig. VI-3). The interactive processor will control the system and the user-machine interface. The batch CPU will run those CPU-bound programs passed to it by the interactive processor. All data files would be passed to the batch program through the common disk and all output will be passed back to the user through the same disk.

It is felt that the system described above will significantly improve our computer user interface over that which now exists. Users will have a direct link to the computer, thereby decreasing response time and increasing system reliability. In addition, the Group 22 resources will be more efficiently utilized. Most major hardware items are now installed. A 40-megabyte disk system is on order for installation this summer. The UNIX software has been ordered and will be installed as soon as the license to use it is obtained. In the meantime, a UNIX system running on another PDP-11 installation within Lincoln Laboratory is being used for software development.

J. Sax

REFERENCES

1. Seismic Discrimination SATS, Lincoln Laboratory, M.I.T. (30 June 1975), DDC AD-A014793/4.
2. Seismic Discrimination SATS, Lincoln Laboratory, M.I.T. (31 December 1975), DDC AD-A025777.
3. D.M. Ritchie and K. Thompson, "The Unix Time-Sharing System," Commun. ACM 17, No.7, 365 (July 1974).

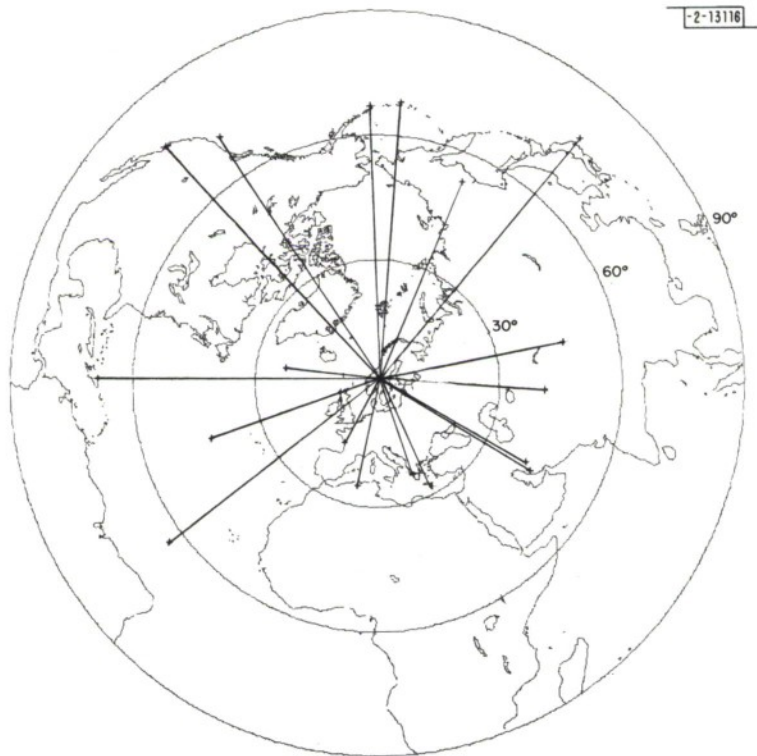


Fig. VI-1. Equidistance projection for NOR SAR events.

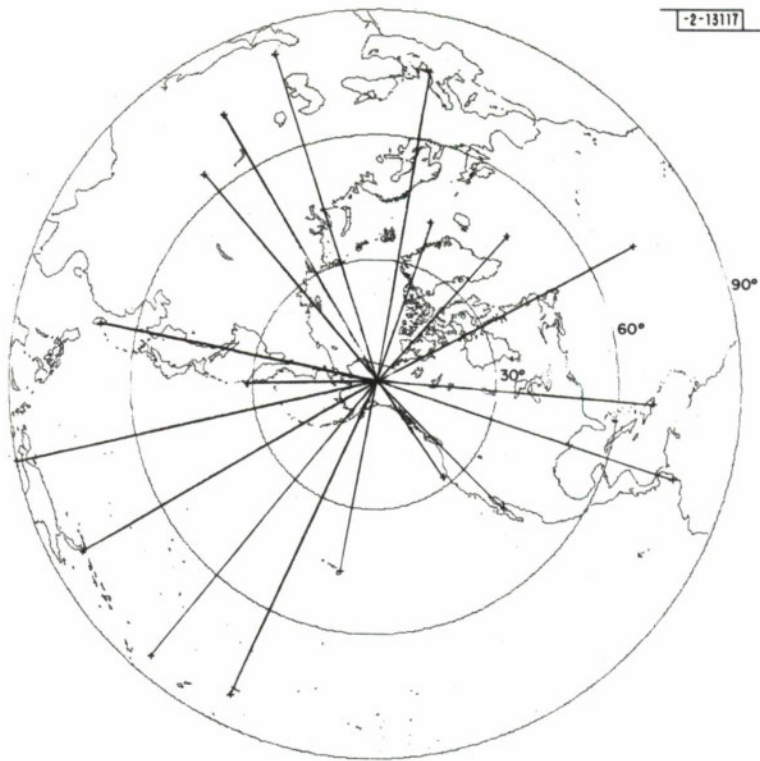


Fig. VI-2. Equidistance projection for ALPA events.

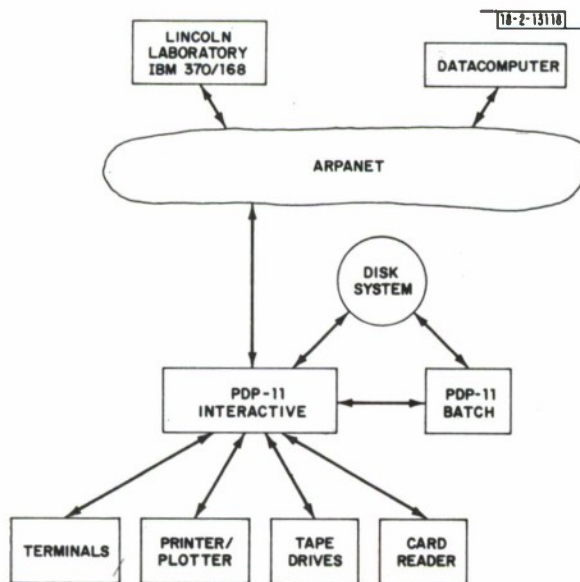


Fig. VI-3. Applied seismology group's PDP-11 system and its relationship to the ARPANET.

GLOSSARY

AIC	Information Theoretic Criterion
ALPA	Alaskan Long Period Array
ARPA	Defense Advanced Research Projects Agency
ARPANET	DARPA Computer Network
ASG	Applied Seismology Group
CAT	Autoregressive Transfer Function Criterion
CCP	Control and Communication Processor
CPU	Control and Processing Unit
EDR	Earthquake Data Reports
FPE	Final Prediction Error Criterion
FTP	File Transfer Protocol
HGLP	High Gain Long Period (Station)
ILPA	Iranian Long Period Array
ILS	International Latitude Service
ISC	International Seismological Center
IWWSS	Integrated World-Wide Seismic System
LASA	Large Aperture Seismic Array
LOD	Length of Day
LRSM	Long-Range Seismic Measurements
NEIS	National Earthquake Information Service
NEP	Network Event Processor
NLS	On-Line System
NOAA	National Oceanic and Atmospheric Administration
NORSAR	Norwegian Seismic Array
NTS	Nevada Test Site
PDE	Preliminary Determination of Epicenters
PEM	Parametric Earth Model
RMS	Root Mean Square
SATS	Semiannual Technical Summary
SDAC	Seismic Data Analysis Center
SDIS	Seismic Data and Information System
SIP	Seismic Information Processor
SPZ	Short-Period Vertical (Seismometer)
SRO	Seismic Research Observatory
USCGS	U. S. Coast and Geodetic Survey
USGS	U. S. Geological Survey
WWSSN	World-Wide Standardized Seismograph Network

UNCLASSIFIED

SECURITY CLASSIFICATION OF THIS PAGE (When Data Entered)

REPORT DOCUMENTATION PAGE		READ INSTRUCTIONS BEFORE COMPLETING FORM
1. REPORT NUMBER ESD-TR-76-185	2. GOVT ACCESSION NO.	3. RECIPIENT'S CATALOG NUMBER
4. TITLE (and Subtitle) Seismic Discrimination		5. TYPE OF REPORT & PERIOD COVERED Semiannual Technical Summary 1 January - 30 June 1976
		6. PERFORMING ORG. REPORT NUMBER
7. AUTHOR(s) Michael A. Chinnery		8. CONTRACT OR GRANT NUMBER(s) F19628-76-C-0002
9. PERFORMING ORGANIZATION NAME AND ADDRESS Lincoln Laboratory, M.I.T. P.O. Box 73 Lexington, MA 02173		10. PROGRAM ELEMENT, PROJECT, TASK AREA & WORK UNIT NUMBERS ARPA Order 512 Program Element No. 62701E Project No. 6F10
11. CONTROLLING OFFICE NAME AND ADDRESS Defense Advanced Research Projects Agency 1400 Wilson Boulevard Arlington, VA 22209		12. REPORT DATE 30 June 1976
		13. NUMBER OF PAGES 112
14. MONITORING AGENCY NAME & ADDRESS (if different from Controlling Office) Electronic Systems Division Hanscom AFB Bedford, MA 01731		15. SECURITY CLASS. (of this report) Unclassified
		15a. DECLASSIFICATION DOWNGRADING SCHEDULE
16. DISTRIBUTION STATEMENT (of this Report) Approved for public release; distribution unlimited.		
17. DISTRIBUTION STATEMENT (of the abstract entered in Block 20, if different from Report)		
18. SUPPLEMENTARY NOTES None		
19. KEY WORDS (Continue on reverse side if necessary and identify by block number)		
<div style="display: flex; justify-content: space-between;"> <div> seismic discrimination seismic array seismology </div> <div> surface waves body waves LASA </div> <div> NORSAR ARPANET </div> </div>		
20. ABSTRACT (Continue on reverse side if necessary and identify by block number)		
<p>This report describes 25 investigations in the field of seismic discrimination. These are grouped as follows: estimation of body wave magnitude m_b by single stations and networks (9 contributions), surface wave studies (2 contributions), examination of methods for the separation of the signals from a sequence of closely spaced explosions (2 contributions), studies concerned with lateral heterogeneity within the earth (5 contributions), miscellaneous studies (3 contributions), and recent developments in our data and computer systems (4 contributions).</p>		

UNCLASSIFIED

SECURITY CLASSIFICATION OF THIS PAGE (When Data Entered)